UNIVERSITY OF ZULULAND

Nickel and Cobalt Sulfide Nanomaterials for Magnetic and Energy Applications

By

Charles Gervas

201445491

B.Sc. ed. (Hons), M. Sc. (University of Dar es Salaam, Tanzania)

THESIS

Submitted in fulfilment of the Requirements for the degree

DOCTOR OF PHILOSOPHY

In the field of

CHEMISTRY

Faculty of Science and Agriculture

Supervisor: Prof. Neerish Revaprasadu

Department of Chemistry, University of Zululand
Private Bag X1001, KwaDlangezwa 3886,
South Africa.

August 2018

DECLARATION

I hereby declare that the work described in this thesis entitled "**Nickel and Cobalt Sulfide Nanomaterials for Magnetic and Energy Applications**" is my own work and has not been submitted in any form for another degree or qualification of the University of Zululand or any other University/Institution for tertiary education. Information derived from the published or unpublished work of others has been acknowledged in the text and a list of references is given.

Name: Charles Gervas

Signature: ……. Date: …….

CERTIFICATION BY SUPERVISOR

This is to certify that this work was carried out by Mr. Charles Gervas in the Department of Chemistry, University of Zululand and is approved for submission in fulfilment of the requirements for the degree of Doctor of Philosophy in Chemistry.

…….

Supervisor

N. Revaprasadu (PhD)

Professor of Inorganic Chemistry

Department of Chemistry, University of Zululand

KwaDlangezwa, South Africa

DEDICATION

This work is dedicated to the Rufyiriza clan and their leader Bizo; a man of God!

ACKNOWLEDGEMENT

My sincere and heartfelt gratitude to Prof. Neerish Revaprasadu, my supervisor. His constant guidance, mentorship and profound support have been unwavering throughout these years of my PhD studies. Thank you for your understanding and dedication!

My family members, both at home in Tanzania and in other corners of the world, have been a wonderful support during these years which I have been away from home. Being aware that we missed one another, they never ceased to keep in contact through telephonic calls, emails, chat on whatsApp and even visitations. May the Almighty God reward you abundantly!

I also would like to thank those in leadership, in the catholic dioceses of Kigoma (Tanzania) and Eshowe (South Africa), Tanzanian Episcopal Conference, as well as the St. Augustine University of Tanzania (SAUT) for their support and encouragement when I started my studies here in South Africa. Their constant prayers, planning and constant reminder of our huge responsibility to the society encouraged me to dig deeper into the field of nanotechnology.

I have received an immense support from congregants in the parishes of KwaDlangezwa (Sacred Heart Parish), Mtunzini (Immaculate Conception Parish), Empangeni (St. Patrick's Parish) in (SA), Kibangu (Dar es Salaam) and my home parish Kiganza (Kigoma). To you all I promise to continue praying for you and will never forget moments of faith and encouragement shared with you.

Without team work with our collaborators, it would have been challenging to achieve the specialized analyses required for this work. I sincerely thank all our collaborators from various learning institutions: University of Zululand (UZ), University of Kwazulu Natal (Westiville campus and Pietermaritzburg Campus), Manchester University (in the UK), Nkwame Nkhuruma University of Technology (Ghana), Younde University (Cameroon), Mumbai University (India) Ben Suef University (Egypt), CSIR (Pretoria), University of Dar es Salaam, Pittsburg State University, Kansas, USA and University of Johannesburg, SA.

I am humbled to have worked with such a dedicated team in our group (UZ NANOGROUP). My special thanks to the entire staff of the Department of Chemistry, University of Zululand.

Postdoctoral fellows in the department (Special mention to Dr. Sixberth Mlowe, Dr. Linda Nyamen, Dr. Joseph Adekoya, Dr. Mavundla, Dr. Rekha Dunpall, Dr. Joseph Kyobe, Dr. Masood, Dr. Paul MacNaughter and Dr. Malik Dilshad) whom we have closely worked together throughout my PhD studies. Thank you all for your time and support!

My colleagues in the lab, Siphamandla Masikane, Sandile Khoza, Zikhona Tshemese, Ginena Bilbard, Zimele Mzimela, Lethukuthula Nene, Philangezwi W. Zibane, Dr. Shesan Owonubi, Kevin Ketchemen, Walter Ndamukong Kun and Gervais Tigwere, to you all receive my special thanks! Thank you for our networking and collaboration!

Judine Govender deserves a special mention for being so effective in communicating to us what was necessary for our group. Ordering chemicals, and organizing trips, conferences and at times pizzas and drinks in our tea room. Thank you Judine!

Lastly, I would like to mention with special appreciation, my special colleague, Siphamandla Masikane (a.k.a Cardinal), you are such a beautiful soul Sipha. Please keep on being who you are and success is already yours!

TABLE OF CONTENTS

ABSTRACT

This thesis reports the symthesis of five metal complexes, namely bis(piperidinylldithiocarbamato)nickel(II) (**1**), bis(tetrahydroquinolinyldithiocarbamato)nickel(II) (**2**), bis(*N'*-ethyl-*N*-piperazinyldithiocarbamato)nickel(II) (**3**), tris(morpholinodithiocarbamato)cobalt(III) (**4**) and tris(*N'*-ethyl-*N*-piperazinyldithiocarbamato)cobalt(III) (**5**). These heterocyclic dithiocarbamate complexes have been characterised using common techniques such as Fourier Transform Infrared spectroscopy, elemental analysis and nuclear magnetic resonance spectroscopy. Nuclear magnetic resonance spectroscopy measurements were not conducted for complexes, due to their paramagnetic behaviour which adversely interferes with the technique. Single-crystal X-ray diffraction was used instead, which aided in the accurate elucidation of novel chemical structures of the complexes. Three complexes were characterised using the technique; the chemical structures of the rest are already known in literature. Generally, dithiocarbamate complexes have been identified as compounds of technological importance, particularly as single-source molecular precursors for the fabrication of nanomaterials for widespread applications. However, interest has mainly been on alkyl derivatives. Thus, this thesis focuses on the use of heterocyclic dithiocarbamates complexes as single-source molecular precursors for the fabrication of the corresponding metal sulfide thin films and nanoparticles through thermal decomposition routes.

Thermal decomposition of the complexes (**1**)-(**5**) produced Ni-S, Co-S and Ni-Co-S nanoparticles and thin films which exhibited interesting morphological and optoelectronic properties. The above-mentioned systems were particularly chosen for their increased interest in magnetism, as well as energy generation and storage applications. In this thesis, the nature of the complexes and other reaction parameters were demonstrated to have an influence on the particle size, morphology, and phase purity of the nanoparticles and thin films produced. These properties have a profound impact on the efficiency of the nanoparticles and thin films, towards specific applications.

The work presented in chapter two aimed at establishing reactions protocols suitable to to produce good quality nanoparticles using the solvent thermolysis approach. The complexes (**1**), (**2**) and (**3**) afforded Ni_xS_y nanoparticles displaying various morphologies (spheres, rods, irregular tetrahedral, nanospheres and irregular shapes) which were identified mainly by the

transmission electron microscopy imaging technique. Furthermore, it was discovered that docecylamine and hexadecylamine capping agents produced phase pure Ni_3S_4 and Ni_3S_2, respectively; phase identification was conducted using the powder X-ray diffraction technique. On the contrary, oleylamine capping agent produced mixed phase Ni_xS_y nanoparticles from complexes (**1**) and (**2**) while complex (**3**) afforded phase-pure Ni_3S_2. Magnetic measurements identified Ni_3S_4 and Ni_3S_2 nanoparticles to possess ferromagnetic and paramagnetic behaviours, respectively. Chapter 3 reports the deposition of thin films using the same three complexes by the aerosol-assisted chemical vapour deposition method; NiS phase thin films were predominantly formed. The scanning electron microscopy imaging technique showed the films to display various morphologies.

Chapter 4 focuses on the catalytic evaluation of Co_3S_4 nanoparticles (with minor CoS_2 impurities) in the oxygen evolution reaction (OER), hydrogen evolution reaction reaction (HER) and supercapacitance applications. The nanoparticles were prepared from complex (**4**) by a facile olelylamine-mediated hot injection method. The OER catalytic performance of nanoparticles prepared at 230 ºC and 260 ºC showed the overpotential of 307 mV and 276 mV, respectively. The specific capacitance and specific stability for the nanoparticles prepared at 230 ºC are 298 F/g and 73%, respectively. Nanoparticles prepared at 260 ºC achieved 440 F/g and 97%. The efficiency was measured after 5000 cycles. These results indicated that the prepared materials are good candidates for efficient energy generation and energy storage devices.

Chapter 5 reports the use of complexes (**3**) and (**5**) as dual precursors for the Ni-Co-S ternary material. Though thiospinels structure show interesting catalytic and energy storage applications, the cationic disorder can have major influence on the energy generation and/or energy storage applications. In this work, the effect of stoichiometric variation of metals in a thiospinel i.e. $Ni_xCo_{3-x}S_4$ was examined on energy generation and storage properties. Nickel or cobalt-rich $Ni_xCo_{3-x}S_4$ nanosheets were prepared by the oleylamine-mediated hot injection method. It was observed that nickel-rich and cobalt-rich nanosheet have different performances when tested for OER and HER, as well as supercapacitance performance. It was observed that the nickel-rich $Ni_xCo_{3-x}S_4$ nanosheets have superior energy generation and storage properties.

List of Figures

List of Schemes

List of Tables

List of abbreviations

TMS	Transition Metal Sulfide
SSP	Single Source Precursor
LPCVD	Low Pressure Chemistry Vapour Deposition
HCP	Hexagonal Closed-packed
FCC	Face-centred Cubic
HER	Hydrogen Evolution Reaction
OER	Oxygen Evolution Reaction
OLA	Oleylamine
HDA	Hexadecylamine
DDA	Dodecylamine
TOP	Tri-*n*-octylphosphine
VSM	Vibrating Sample Mangetometer
CSD	Cambridge Structure Database
PIPDTC	Piperidine Dithiocarbamate
THQDTC	Tetrahydroisoquinoline Dithiocarbamate
DSSC	Dye-sensitized Solar Cells
TOPO	Tri-*n*-octylphosphine oxide

CHAPTER ONE

INTRODUCTION AND LITERATURE REVIEW

1.1. General introduction

Nanotechnology in recent years has brought a revolution in the mindset of the materials sciences community, with different materials exhibiting interesting properties at the nano-scale size regime. Generally, the field focuses on the understanding and control of matter at nano-scale dimensions between 1 nm to 100 nm. The resulting nanomaterials (consisting of nanoparticles, nanorods, nanowires, nanoflowers), depending on the morphology of the materials, would portray unique optoelectronic, magnetic, and physicochemical properties when compared to their bulk counterparts [1, 2]. Thus, these properties lead to exploitation in diverse novel applications. As a result, control and manipulation of particle size and shape at the nanometer scale have been identified as the key driving force in the field of nanotechnology [3].

The synthesis protocols of nanomaterials have been dominated by two approaches, namely the bottom-up approach and top-down approach. The former is a typical self-assembly process through a nucleation mechanism at the atomic level, whereas the latter is concerned with the breaking down (mostly a physical process) of bulk materials to afford nanostructures. Regardless of the type of approach, the breakthrough in nanotechnology over recent years has been advocated predominantly by the synthesis of colloidal quantum dots [4]. As a result, it is mostly common that synthesizing monodispersed nanostructures with well-defined morphology and properties, scaling up for green industrial production, and more understanding on the tuning of physical-chemical related properties, are likely to be the main current trends in nanotechnology research projects [5].

Transition metal sulfide (TMS) nanomaterials, a class of metal chalcogenides, have been recognized for their rich structural diversities in applications. They receive considerable attention due to their interesting electronic and magnetic properties. Furthermore, they are relatively cheap and abundant; most occur naturally in different mineral forms [6]. Such nanomaterials, including thin films, have been widely researched in fields focusing on photovoltaic technologies, semiconductors, telecommunication, bioimaging and solar cells, amongst others [7, 8].

The synthesis of TMS nanomaterials can either follow multiple-source or single-source precursor routes, depending on compatibility with the synthetic protocols. The single-source precursor (SSP) route is mostly preferred due to pre-existing metal-sulfur bonds in the

compounds, thus, requiring only careful decomposition of the compounds to afford nanomaterials of desired stoichiometry. Furthermore, the route eliminates multiple reaction steps which would adversely result to challenges in controlling the properties and/or features of nanomaterials, as well as preventing contamination issues. Dithiocarbamate metal complexes have, for some time, demonstrated their outstanding performance as SSPs desirable for the fabrication of TMS nanomaterials. Dithiocarbamate ligands are widely observed for their ability to bind effortlessly to transition metals centers of different oxidation states [9, 11, and 12]. Dithiocarbamate ligands can readily produce chelating compounds, with an ability to coordinate to a wide range of transition metals via its two donor atoms of sulfur. They can also stabilize low and high oxidation state metal ions, thus, rendering them as important compounds in the synthesis protocol of single source precursors. The complexes inherently become desirable for their diversity, easy preparation and long shelf life in ambient conditions. These complexes have also been reported in literature to have widespread applications such as in the material science, biomedical and agricultural fields [10].

Though dithiocarbamate complexes as single source precursors have been studied widely in the area of nanotechnology, the heterocyclic dithiocarbamate class have recently been investigated in detail [13]. From literature reports, distinguished research groups such as Revaprasadu and co-workers have demonstrated the attractive qualities of heterocyclic dithiocarbamates in the fabrication of TMS nanomaterials, e.g. piperidine and tetrahydroisoquinoline dithiocarbamato cadmium(II) complexes to afford CdS nanomaterials [14]. The same group has also reported other TMS nanomaterials such as PbS and ZnS fabricated from the corresponding metal heterocyclic dithiocarbamates [14, 15].

Dithiocarbamate ligands, like other related dithiolates, are formed through the nucleophilic attack on the carbon disulphide molecule, as shown in Scheme 1.1. Dithiocarbamates bonding mode with metals is shown in Figure 1.1 where the coordination capabilities of the ligands are shown to proceed through the monodentate (**I & II**) or bidentate manner (**III**). Such mode of coordination has been reported to contribute to the overall electronic structure of the resulting complexes.

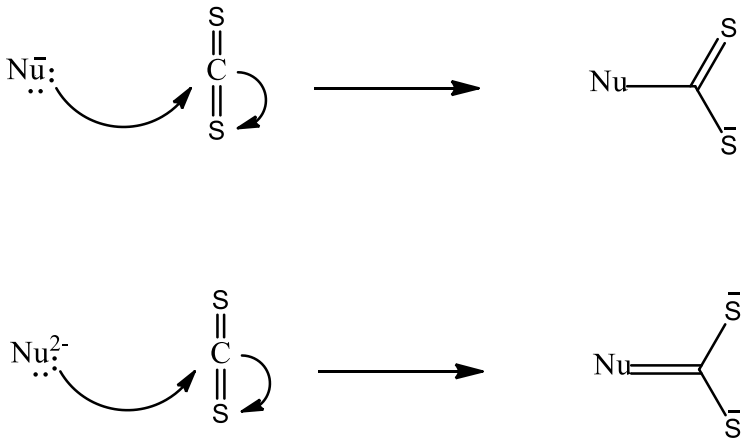

Scheme 1.1: Nucleophilic attack of carbon disulfide.

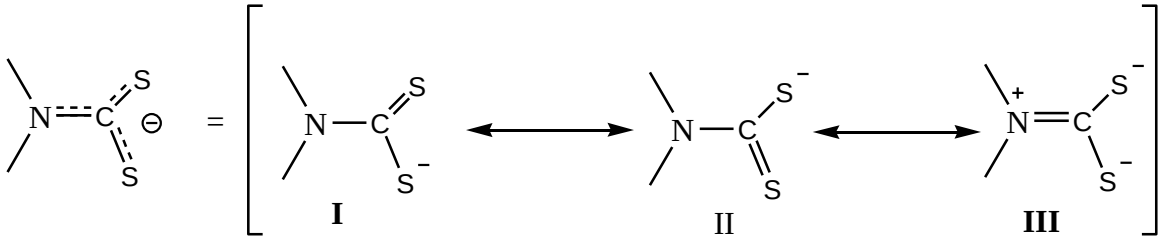

Figure 1.1: Resonance forms of dithiocarbamic-NCS_2^- moiety.

Dithiocarbamates as common compounds that bind strongly and selectively to a range of metal ions, have in recent times attracted and controlled self-assembly of many beneficial supramolecular methods for preparation of nanomaterials [16]. While dithiocarbamates, in general, share the characteristic disulfur motif that binds to the metal as a bidentate ligand (Fig. 1.1), the nitrogen may be functionalized in various ways to modify the physico-chemical properties of the ensuing metal complex, in particular its solubility and lipophilicity. This gives them a very useful characteristic when it comes to their biological applications [17].

Since different dithiocarbamates derivatives may end up having different physico-chemical properties for the ensuing metal complex, it is important to select a group of dithiocarbametes that can beneficially suit the synthesis protocol for a particular application. For instance, iron dithiocarbamate complexes may easily bind free NO radicals to form stable mononitrosyl iron complex. For that matter, iron dithiocarbamate complexes can be applied industrially to scavenge free NO [18]. In a biological study by Pieper et al. [18] iron(II)

diethyldithiocarbamate and iron(II) *N*-methyl-d-glucaminedithiocarbamate complexes were observed to displayed hydrophobic and hydrophilic behavious. Hence, were we found to be suitable for different biological applications. Another example is the organotin(IV) dithiocabamate complexes which are found to have the ability to stabilize specific stereochemistry in their complexes and subsequently find diverse applications in agriculture, biology and catalysis research fields [19]. Their usefulness as single source precursors for tin sulfide nanoparticles has made them relevant in modern times [20], as a result, devising easier access to SnS nanoparticles which are desirable for their stereo-electronic properties most relevant in the field of medicinal chemistry [21-23]. Organotin(IV) dithiocarbamates, therefore, owe their functionalities and usefulness to the individual attributes of the organotin and the dithiocarbamate moieties present within the molecule.

Similarly, different functionalities of metal dithiocarbamate complexes have different decomposition pattern, thus, leading to different nanomaterials. Hollingsworth *et al.* [24] examined complexes of nickel dithiocarbamates and concluded that the properties of the inorganic products dependend on the amide-exchange intermediates formed in the course of their decomposition. The phase of nanoparticles produced is dictated by the extent of the amide-exchange mechanism. In their study, Hollingsworth *et al.* [24] established that nickel dithiocarbamate complexes which decompose via a single amide-exchange mechanism form NiS, while those that decompose through a double amide-exchange machanism favoured the formation of Ni_3S_4 nanoparticles. Gervas *et al.* [25] have indicated that a choice of a capping agent also plays key role in directing the decomposition pattern and hence influencing the type of amide exchange mechanism which inadvertently controls the phase of the Ni-S system for exploitation in a specific application. It is therefore important to search for reaction parameters (particularly the choice of dithiocarbamate ligand and capping agents) which will fine-tune the properties of the nanoparticles to achieve high efficiencies in various applications.

1.2. Literature Review

As it has already been established, TMS nanomaterials play a major role in the current state of technological advances due to their continuously improved and/or novel properties. Access to these properties is easily achieved through tweaking reaction parameters during synthesis and/or processing of the as-synthesized nanomaterials. However, careful consideration

of the type of TMS plays a major role since they possess different chemical behaviours. The current theme in the nanoscience field is the search of alternative non-toxic materials which exhibit similar or improved properties to the existing toxic counterparts. Thus, TMS materials such as Ni_xS_y and Co_xS_y have received a lot of attention due to this respect. Ni_xS_y and Co_xS_y nanomaterials, like other transition metal sulfides, have a wide range of potential applications. Ni_xS_y sulfide nanomaterials have potential use in rechargeable lithium batteries [26], catalytic degradation of organic dyes and magnetic devices [8]. Co_xS_y nanomaterials can directly be used in solar selective coatings, photo detectors, magnetic devices, lithium ion batteries and biological labelling [27, 28].

Given the tremendous technological importance of Ni_xS_y and Co_xS_y nanomaterials, different synthetic routes have been reported. As a rule of thumb in nanotechnology, the control over particle size can tune the band-gap for nanomaterials to suit specific applications. In order to attain this goal, a number of synthetic routes have been applied. One of the efficient routes involves the wet chemical approach where nanoparticles form through growth processes in solutions of a molecular precursor. Murray and co-workers pioneered this technique by injecting volatile metal alkyl compound and an organic chalcogen source in hot tri-*n*-octylphosphine oxide preheated at temperatures of between 120 °C and 300 °C [4]. Although the method affords high quality nanomaterials, it suffered from severe challenges and limitations. One of the limitations was the use of the metal alkyl such as $[(CH_3)_2Cd]$, which is extremely toxic, expensive, pyrophoric, and explosive at higher temperatures. Since then, the method has undergone drastic improvements, such as the employment of alternative, safer and non-toxic precursors.

The SSPs route is one of the exemplary efforts which overcame issues such as that encountered in Murray and co-workers route. It substitutes the undesirable multiple precursors; reactions parameters remain similar, e.g. the use of the boiling coordinating solvent at elevated temperatures. The choice of these solvents depends on their ability to promote the decomposition of the SSP while efficiently passivating the surface of the nanomaterials formed [29]. Trindade and O'Brien demonstrated the use of cadmium (II) dithiocarbamate complexes as SSPs to synthesize CdS nanomaterials. The works of Revaprasadu and co-workers have reported the continued use of various metal dithiocarbamate precursors to synthesize corresponding metal sulfide nanomaterials [13, 14, 30]. The works further demonstrated particle size, shape and

morphology control by varying reaction parameters such as precursor concentration, type of capping agent, reaction temperature and time. Good precursors for the deposition of thin films should have high purity to exclude substances which at times can act as dopants on thin films (external impurity) and it should be volatile to facilitate its transport from the reactor to the substrate in the furnace. Clean substrate surface is also crucial, to avoid intrinsic impurities [7]. Deposition of various 3d TMS thin films from the corresponding dithiocarbamates complexes by the aerosol-assisted chemical vapour deposition AACVD route, have been reported [31, 32].

The AACVD protocols follow 8 basic steps, namely: 1) precursor generation of reacting gaseous species, 2) transport media to deliver the precursor in the reaction chamber/furnace, 3) adsorption of the precursor into the hot substrate surface, 4) precursor atomic decomposition so as to give the required film, 5) movement of the atoms to a strong binding site, 6) nucleation which can lead to the growth of thin films, 7) desorption of the unwanted by-products, and 8) the removal of unwanted products. A schematic representation of the AACVD assembly is shown in Figure 1.2.

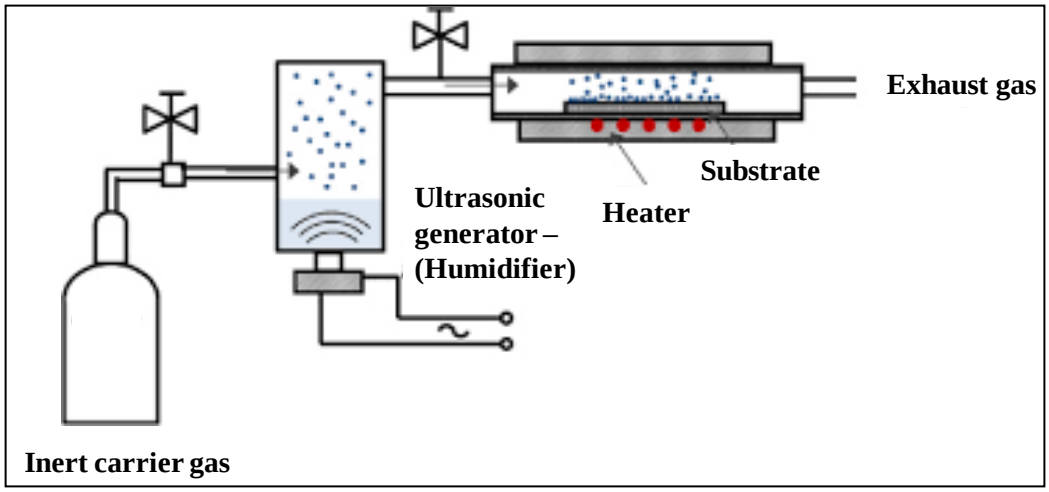

Figure 1.2: A schematic diagram of AACVD apparatus assembly.

1.2.1. Nickel Sulfide (Ni_xS_y) Nanoparticles and Thin Films

Ni_xS_y nanoparticles and thin films are in the class of important TMSs exhibiting potential properties for a number of applications including cathode materials for rechargeable lithium

battery, catalysts, magnetic devices, solar coating, photoelectrochemical storage devices and a range of other important applications [33, 34]. It exists in species exhibiting different stoichiometries, such as Ni_6S_5, Ni_7S_6, Ni_3S_4, Ni_3S_2, and NiS. Ni_xS_y nanoparticles and thin films have been synthesized by following reaction routes such as the soft solution method, solvothermal process, UV irradiation, laser ablation, sol-gel method, chemical precipitation method, and dual or single-source-incorporated CVD [8, 34]. O'Brien and co-workers have reported the deposition of Ni_xS_y thin films by both low pressure (LP) CVD and AACVD methods utilising nickel dithiocarbamate SSPs [35,36]. Phases of $NiS_{1.03}$ or a mixture of $NiS_{1.03}$ and NiS were deposited on glass substrate with variation of temperature. Alam and co-workers observed that the thin films deposited from the nickel(II) xanthates SSPs by AACVD [24] at temperatures not exceeding 300 °C were either amorphous or sparsely deposited on the substrates. However, an increase in temperature afforded orthorhombic Ni_7S_6 and hexagonal $NiS_{1.03}$ thin films [36].

The Ni-S phase diagram is known for its complexity [37, 38]. The wide range of different phases has prompted some of the phases to be widely researched, while other phases though equally important, are not widely studied. The different phases of Ni_xS_y results in different applications; for instance, NiS_2, a p-type semiconductor with a band gap of about 0.5 eV, is among the phases widely researched due to its suitability for use in photoelectrochemical solar cells, IR detectors, catalysis and sensors [39]. On the other hand, Ni_3S_2 manifests metallic properties [40]; it changes into $Ni_{3+x}S_2$ phase at temperatures above 256 °C [41, 42]. Similarly, other Ni_xS_y phases are able to be transformed into other phases by varying temperature.

Some nickel-based SSPs have been effectively used to produce phase-pure Ni_xS_y nanoparticles and thin films; phase and size control can be achieved if the role of ligands and capping agents are well understood in the preparation method [34]. There are exemplary literature reports such as the synthesis of Ni_3S_4 affording different morphologies (wires, rods, spheres, and triangles) via a solvent thermolysis of nickel(II) thiobiuret SSPs [43]. The variation of temperature and capping agent concentration gave different morphologies for Ni_3S_4, while NiS only exhibited the nanowire morphology when the SSPs were dispersed in oleylamine then injected in a hot solvent, 1-octadecene.

1.2.2. Cobalt Sulfide (Co_xS_y) nanoparticles and thin films

Co_xS_y is commonly known to be a ferromagnetic material, thus, mostly used as an alloying compound in permanent magnets. It exists in basically two crystallographic systems, namely: hexagonal close-packed (HCP) and face-centered cubic (FCC). Normally HCP is stable at room temperature while FCC is stable at higher temperatures above 450 °C [44].

Co_xS_y, like Ni_xS_y, exhibits a number of phases such as Co_4S_3, Co_9S_8, CoS, Co_3S_4, Co_2S_3 and CoS_2 [6]. Thus, there is a challenge of optimizing synthetic routes to obtain a specific, desired phase. However, hexagonal $Co_{1-x}S$ nanoparticles have been easily prepared by a solvent thermolysis of $[Co\{N(SCNMe_2)_2\}_3]$. The particle size was found to be influenced by reaction time and nature of the capping agent used. When the $[Co\{N(SOCN^iPr_2)_2\}_2]$ complex is decomposed under the same reaction conditions, a mixture of hexagonal and cubic cobalt sulfide exhibiting irregular shapes was obtained [45-47]. Thus, this demonstrates a need for continued search on fabrication routes and reaction conditions to achieve high quality nanoparticles of specific phase, particle size, shape and morphology.

The challenges in the fabrication of Co_xS_y nanomaterials and thin films can be attributed to the chemistry of Co. For example, challenges in obtaining monodispersed cobalt nanoparticles are caused by agglomeration as a result of nanoparticles having difficulties in trying to reduce their high surface energy, typical for metal nanoparticles. These are caused by attractive forces exerted on the Brownian motion and van der Waals forces in nanoparticles. For Co nanoparticles, such forces are even greater, due to the additional influence of their magnetic properties [48]. To overcome such challenges, strategies have to be designed so as to give high yield of the nanoparticles in the desired shape, size and morphology.

General strategies for obtaining monodispersed nanoparticles include separation of the nucleation and growth stages during synthesis, controlling the mode of growth and prevention of random growth of nanoparticles. Factors affecting the shapes of inorganic nanocrystals have been reported to involve competition between thermodynamic and kinetic factors [49]. According to this model, reactions at higher temperatures are controlled by thermodynamic parameters while at lower temperatures they are mostly under kinetic control. The work of O'Brien and co-workers have reported the shape control of cobalt sulfide nanoparticles, under

different temperature conditions; a mixture of spherical and irregular shapes was obtained at thermolysis temperature of 230 °C, while only the spherical shape is obtained when the temperature is increased to 250 °C [35]. This phenomenon is due to the influence of thermodynamic parameters, although at higher temperatures, some other factors play a role, e.g. Ostwald ripening process [50]. Furthermore, the study equally indicated that the concentration of the reactants has an effect on the nanoparticles. This observation is explained by the delicate balance between kinetic and thermodynamic control, which is why anisotropic growth is observed at high flux of the monomer [51]. Deposition of Co_xS_y thin films have also been reported in literature. Solution (chemical bath deposition) technique and AACVD are the two mostly used approaches to prepare Co_xS_y thin films [52, 53].

1.2.3. Ternary Nanomaterials with Thiospinel Structure

Thiospinel structures of transition metal sulfides in the form of AB_2S_4 have emerged to be important materials for various applications in areas such as catalysis, energy; (generation, storage and conversion) and also in electronics [54]. The advantage of such structure lies in its unit cell having metal atoms A and B occupying the tetrahedral and octahedral sites, thus, enabling their position to shift within the cell, and hence giving rise to a normal and inverse spinel structure [55]. A normal spinel structure has A^{+2} in tetrahedral position and B^{+3} in an octagonal structure, where the general formula is AB_2X_4 (e.g. $MgAl_2O_4$). An inverse spinel structure has a general formula of $B(AB)X_4$ with B^{+3} tetragonal position (B^{+2} B^{+3}) in octahedral position. An example of an inverse spinel is $CoFe_2O_4$. A typical inverse spinel crystal structure is indicated in Figure 1.3, showing both octahedral and tetrahedral positions.

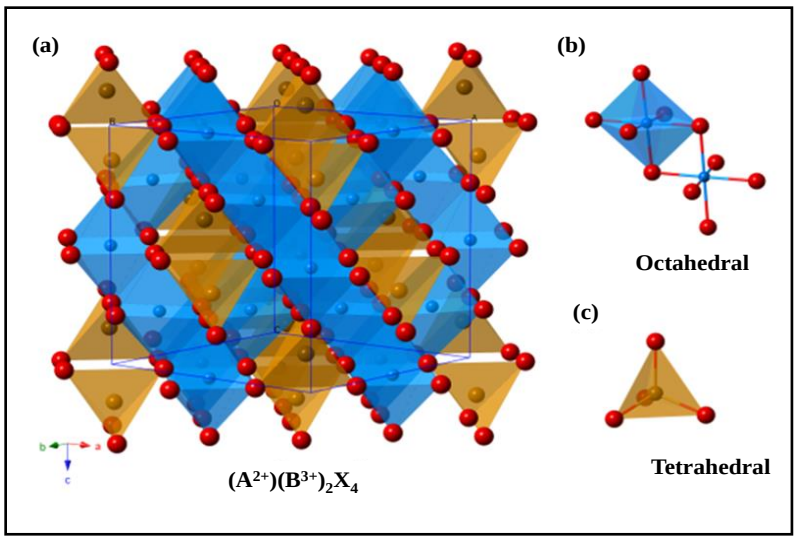

Figure 1.3: The (a) crystal structure of inverse spinel AB_2O_4 and (b) corresponding octahedral and (c) tetrahedral sites [56].

On the other hand, the normal thiospinel model of crystal structure is represented in Figure 1.4 below:

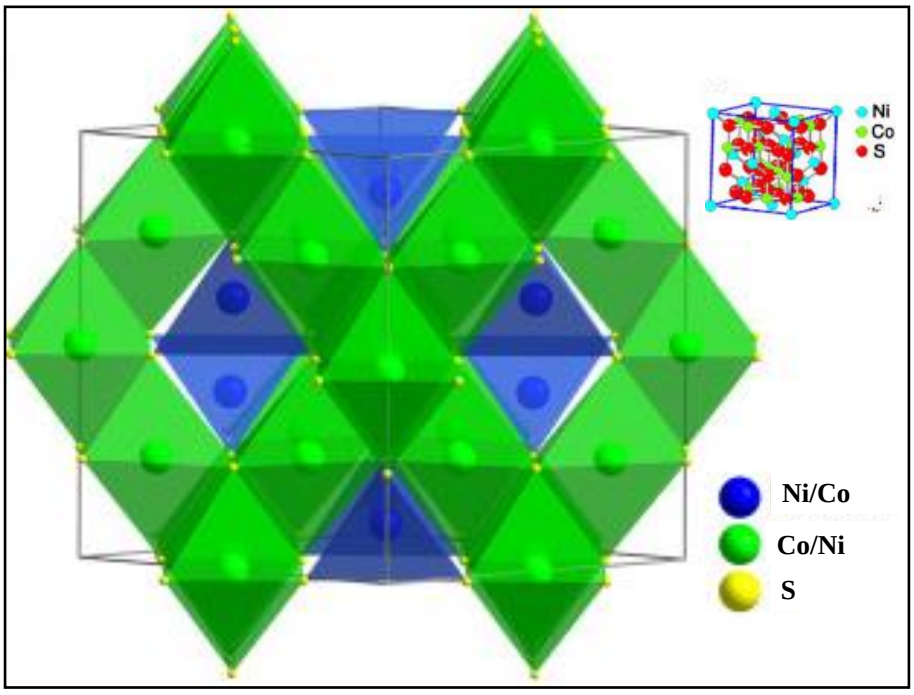

Figure 1.4: Model of normal spinel structure with the crystal model inset for $NiCo_2S_4$.

Figure 1.4 shows a normal spinel, crystal structure $(Ni)_A[Co_2]_BS_4$ where A still represent a divalent metal and B a trivalent metal. In such material both nickel and cobalt occupy tetrahedral sites (A) and octahedral site (B). If you consider a unit cell of such material, it would be only one eighth of A sites which will be occupied by Ni^{+2} and half of the B sites are occupied by Co^{+3} [57].

Such kind of structures in Figures 1.3 and 1.4, which have multivalence metals A and B, give thiospinel materials special properties in redox reaction, good electrical conductivities and an abundance of many sulphur vacancies at the surface of the material [58]; the bimetallic sulfide of cobalt and nickel form materials with the same structure. These properties can be harnessed to make devices which can generate or store energy [59]. Supercapacitors are considered best candidate as energy storage devices.

1.2.4. Magnetic properties

Structural, electronic and magnetic properties of a material are highly dependent on particle size as it approaches the nanoscale level [60]. Magnetic properties are further affected by other parameters such as particle shape, chemical composition, electronic bond-to-bond interactions and crystal structure of the material [61]. The evolution of nanomaterials has opened a window of opportunities to study magnetic properties with respect to those of the bulk counterparts [62].

Magnetism or magnetic properties of a material is a result of electronic interaction in an orbital when subjected to external magnetic field. This interaction gives rise to magnetic moments whose origin is mainly from electron spinning and the motion of the orbital itself. Hence, net magnetic moment is the sum of these interactions. Since all materials have electronic orbit and electronic interactions, all materials are thus considered to be magnetic in nature. The only difference is the magnitude of magnetism in particular material [63]. In some materials, there is no collective interaction from the atomic magnetic moments, whereas other materials have very strong interaction between atomic moments [64]. Magnetic properties of the material can be classified as being diamagnetic, paramagnetic, antiferromagnetic and ferromagnetic. Diamagnetic means having permanent magnetic moments because all electrons in their orbitals are fully paired, thus making materials (e.g. water, protein, fats, etc) tend to repel flux lines of

applied electric field weakly. Paramagnetic materials have net magnetic moment due to unpaired electrons in the electronic structure to such material applying magnetic field would tend to orient the dipole moments. Antiferromagnetic property means the individual dipoles have magnetic moments due to antiparallel magnetic moment such that the net result for magnetism is zero); in such materials (mostly metal oxides), exchange of interactions favours antiparallel orientation of atomic magnetic dipole. Ferromagnetic materials have individual magnetic dipoles but since the dipoles have different magnitude then the net results is not zero. Thus, in ferromagnetic materials, quantum mechanical exchange interactions would favour parallel alignment of moments [65, 66].

Ferromagnetic materials have a tendency of forming what is known as domains, i.e. magnetization is in a uniform direction. Domain is a basic concept in magnetism. Although all domains are spontaneous, the direction of magnetization will vary from one domain to the other. The sum total magnetization becomes near to zero. Domain structure minimizes energy due to stray fields. When an electric field is applied on the domains, their structure changes; domains whose magnetization is in the direction of the field tend to grow while domains in other directions shrink. This characteristic is very important because if strong field is applied then magnetization can be saturated, thus, creating a single domain and the removal of the field does not necessarily change the domain structure to its original size, hence resulting into ‘magnetic hysteresis’ [67].

A general practice to identify the magnetism of a material is by studying and extracting information from its hysteric loop. Figure 1.5 shows an example of a hysteric loop and information which can be drawn from the loop. Figure 1.5 refers to a material (a) magnetized to saturation by the alignment of domains, (b) the magnetic material retains a considerable level of magnetization (useful for memory devices), (c) coercivity stage where magnetic field must be reversed and increased to a large value to drive the magnetization, (d) saturation points but towards the opposite direction, (e) material has been magnetized and the magnetic field can be dropped to zero because magnetic material will retain its history, and (f) the applied magnetic field intensity.

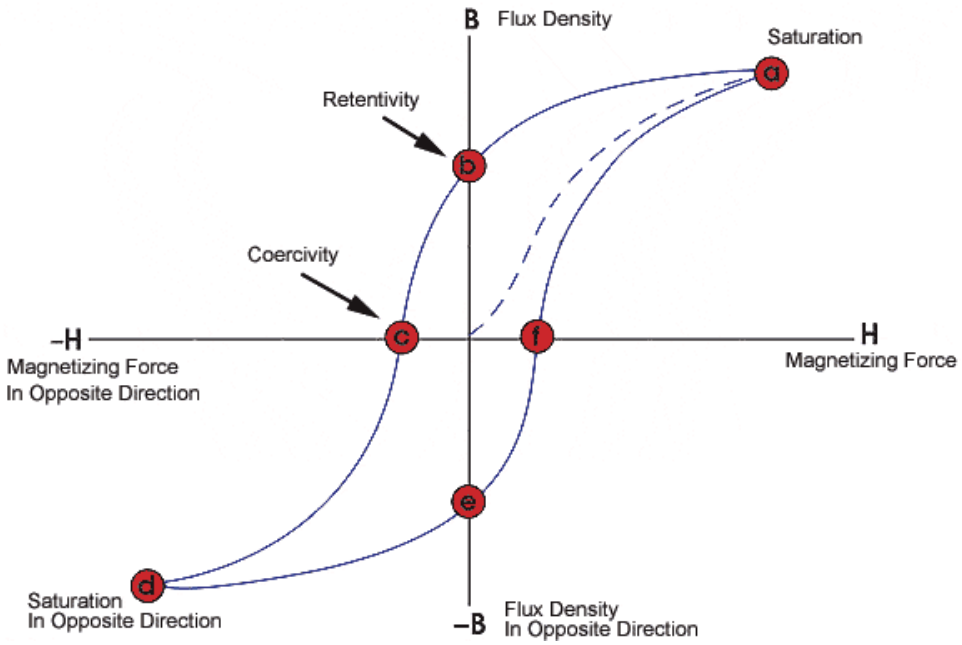

Figure 1.5: Hysteresis loop indicating information to be learned on magnetic properties of materials.

Magnetic nanoparticles (MNPs) are currently providing substantial knowledge on magnetic interaction and magnetic phenomenon at the nanoscale level. Most of critical magnetic lengths (whether single or multi-domain structure, ferrimagnetic or superparamagnetic) are found at the nanometer-size regime (1-100 nm). This makes size tuning in nanomaterials an important factor to equally tune the desired magnetic properties of material.

Single-domain nanoparticles are very important in the establishment of well-understood prototypes which are useful in probing more complex magnetic phenomena [68]. MNPs have important applications in pharmaceuticals and biomedical [69], magnetic fluid [70], data storage [71], magnetic resonance imaging [72], and environmental remediation [73], among others. All these applications require precise control of MNPs in the synthesis protocol such that the magnetic properties to suit specific applications are attained.

Non-precious metal chalcogenides with magnetic properties become desirable over other materials. They are of low cost, high abundance, less toxic and mostly possess unique magnetic, electric and optical properties [74- 77].

1.2.5. Energy Applications

Consumption of electricity is estimated to be growing annually at a rate of about 2.5%. Fossil fuel combustion account to almost 70% of the total power produced globally, while 11.7% comes from nuclear power plants. Hydroelectric power generates about 16% and wind turbines contribute to global power consumption by 2.5%. Photovoltaic produces 0.6% and other sources like geothermal, solar power give 1.4% to the total of the global power production. To reduce global warming, fossil fuel consumption should be replaced by renewable clean energy. The switch to clean energy is inevitable since energy is among the topmost problems facing human society today [78].

The International Renewable Energy Agency (IRENA), International Energy Agency (IEA) and the Renewable Energy Policy Network for the 21st century (REN21) have reported that almost 29% of total energy produced globally is consumed by the transportation sector [79]. The transport vehicles traditionally use internal combustion engines whose efficiency is approximately 25%. If the internal combustion engines would switch to grid electricity for wheels, its efficiency would increase up to 80 %. If then hydrogen gas can be used as fuel with the provision of grid electricity to wheels, it can play an important role in the transportation sector. This is because a car running on fuel cell-generated hydrogen coupled in connection to grid electricity to wheels has overall efficiency of ~28%. Thus, energy storage is an important element in this regard. Electricity storage is more important in renewable energy systems due to the nature of its source and the variability of electricity load required by the user.

1.2.5.1. Energy storage applications (supercapacitors)

Energy storage and energy generating materials have recently become a key area of interest among material scientists and engineers, in pursuit of meeting the technological demands of modern world industrialization and population increase [80]. Important energy storage devices include fuel cells, batteries and supercapacitors, amongst others. Some important applications of supercapacitors is their incorporation in electric vehicles, industrial equipment and memory backup equipment. Figure 1.6 represents basic components and operation of a typical supercapacitor. There are three classifications of supercapacitors, namely: double layer

capacitors, pseudo-capacitors and hybrid capacitors, which have different applications as depicted in Figure 1.7.

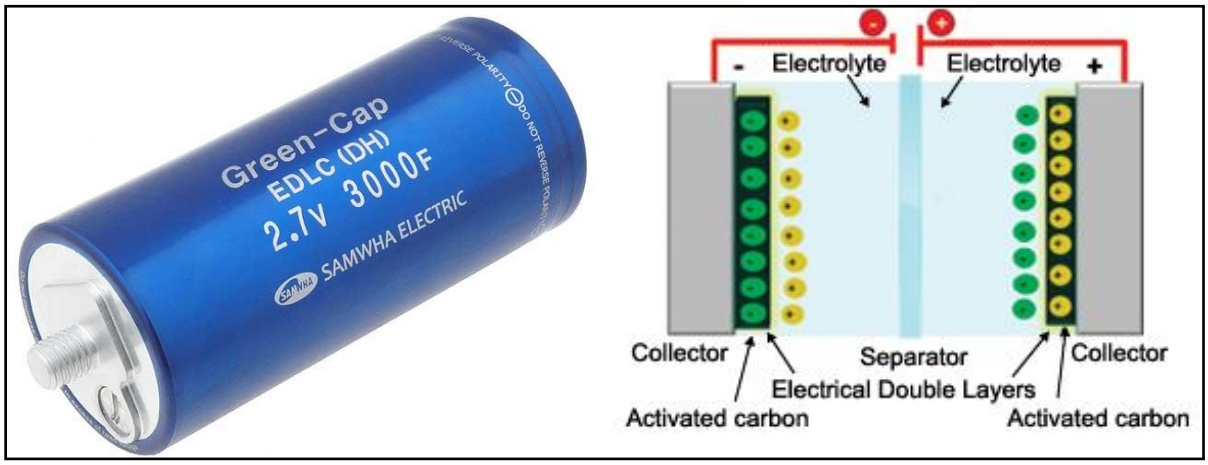

Figure 1.6: Schematic representation of supercapacitors.

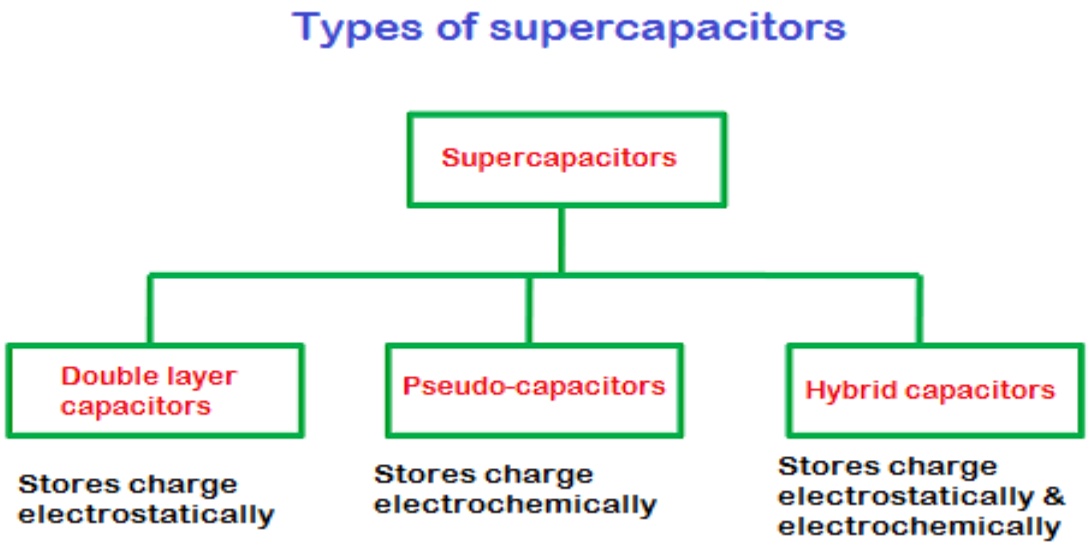

Figure 1.7: Schematic tabulation of different types of supercapacitors.

But what are supercapacitors (ultracapacitors) or electrochemical capacitors? These are energy storage systems which have recently gained popularity due to their potential application in energy storage devices. They can be thought of as a hybrid device which possesses qualities of both an ordinary capacitor and a battery, but technologically different from them.

Ultracapacitor cells have a positive and negative electrode separated by an electrolyte, similarly to a battery. However, they store energy electrostatically (like a capacitor) rather than chemically (typical of a battery).

Supercapacitors have recently gained popularity because of safety issues related to Li-ion batteries which have been reported to catch fire or explode when used in devices like mobile smartphones, laptops and related technologies [81]. Supercapacitors have also proved to perform better than Li-ion batteries when it comes to charging time. Researchers have now focused their attention on supercapacitors so that the challenges faced by battery technology can be addressed and hence developing more reliable and safer source of energy [82].

Practical applications of supercapacitors are limited by the lack of high-performance electrode materials, which could be easily prepared at reasonably low cost [83]. Exemplary materials include graphene and carbon nanotubes [84], transition metal derivatives like (metal oxides, metal hydroxides, metal sulphates and metal sulfides), and conducting polymers [18]. Unfortunately, these materials are limited by poor conductivity, low capacitance, mechanical degradation and high cost. Relatively cheaper and high performance materials thus become the main objectives and goals in the field of sustainable energy. Ni, Co and Mn have been recognized as alternative candidates, due to their natural abundance [85]. Furthermore, researchers have highlighted the Ni-Co-S ternary system to exhibit better electrochemical performance than other alternative such as the Ni-Co-O system [18]. Hence, the former ternary system has been recently crowned a hot topic in the field of nanomaterials and related applications [86-91].

$NiCo_2S_4$ has been exploited for various applications such as anodes for lithium-ion batteries [92, 93], electroactive materials for micro-supercapacitors [94, 95] and bifunctional electrocatalyst for water splitting reaction [96-99]. In these examples, the nanomaterial showed superior performances compared to the $NiCo_2O_4$ counterparts. Replacing oxygen with sulfur creates a more reactive structure attributed to the elongated chemical bonds; thus, making it easier for electrons to be transported in a carefully-fabricated nanostructure which ultimately contribute to the enhancement of the electrochemical performances of supercapacitors and related electrocatalytic reactions [100]. Specifically, $NiCo_2S_4$ nanomaterials not only provide much higher electrochemical activity and specific capacitances than the corresponding Ni-S and

Co-S binary derivatives, but also have an electrical conductivity 100 times greater than that of $NiCo_2O_4$; conducting ability of $NiCo_2O_4$ is only two orders of magnitude higher than those of Ni-O and Co-O binary derivatives [101, 102].

Researchers have prepared Ni-Co-S nanomaterials exhibiting various supercapacitance efficiencies, by using various synthetic protocols. Liu *et al*. [103] used the hydrothermal method to prepared flowerlike $NiCo_2S_4$ nanomaterials whose specific capacitance was 1516 Fg^{-1} at 2 Ag^{-1}. Similarly, Li *et al*. [104] prepared $NiCo_2S_4$ materials with hollow sphere morphology using the hydrothermal method. The material exhibited a specific capacitance of 1753.2 F g^{-1} at 1A g^{-1} compared to 1036 F g^{-1} at 1 A g^{-1} reported by Shen *et al*. [105]. Furthermore, the nanomaterials achieved a rate capability of up to 77.8% from 1 to 10 A g^{-1}. Microwave approach to prepare $NiCo_2S_4$ nanomaterial has been reported by Yan *et al*. [106], where they obtained a tremella-like morphology and a specific capacitance of 1410.7 F g^{-1} at 1 A g^{-1}. The nanomaterial also showed a very high rate capability of 92.7% at 20 Ag^{-1}. A specific capacitance of 10.82 F cm^2 was obtained at 10 mA cm^{-2} [107] from $NiCo_2S_4$ nanomaterial electrodeposited on nickel foam.

Figure 1.8 depicts the performance chart for commonly available technology for energy storage devices. Supercapacitors are, by far, the attractive devices in the field. For supercapacitors to be highly efficient, they need materials that will have high power density, fast charge-discharge kinetics and long-life cycle as compared to other battery counterparts [108].

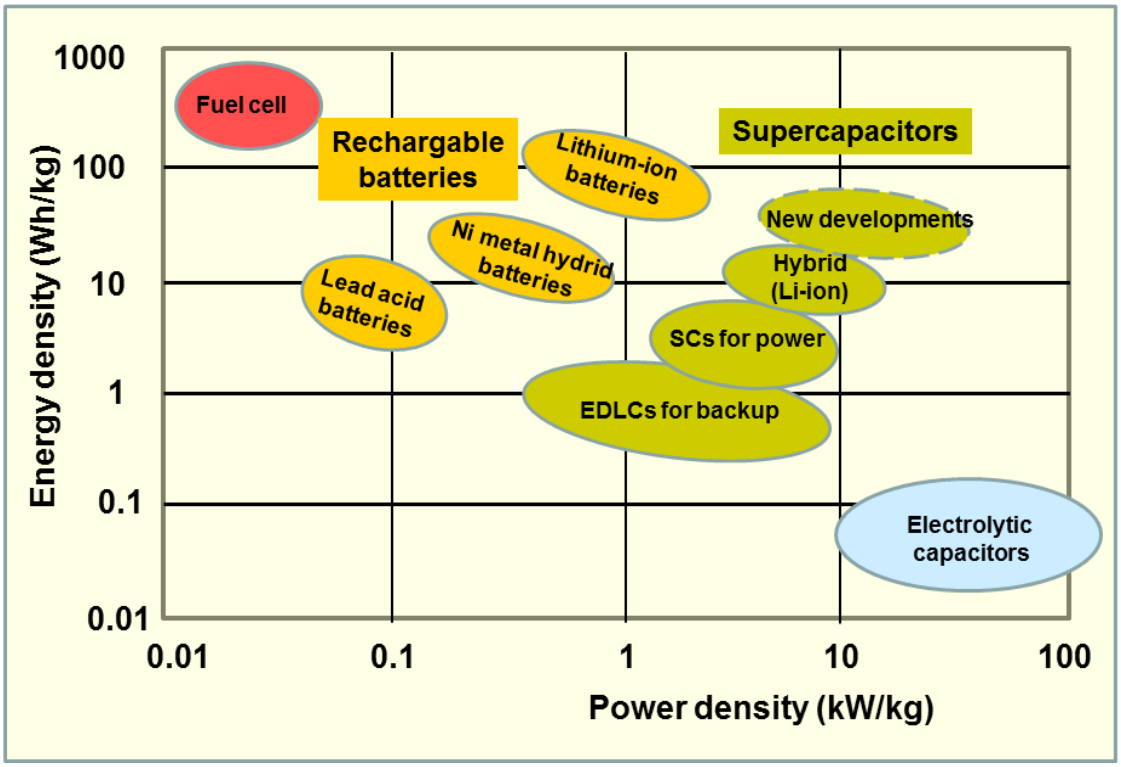

Figure 1.8: A comparison chart for performance of some energy storage devices.

Traditionally, performance and durability of both batteries and supercapacitors largely depend on electrodes which are conductive and can manage to survive the hurdles of charging cycles. Very often, electrodes have polymeric binders which stabilize the electrode materials and subsequently the conductive charges during operation or charging cycles. However, binders fail to perform well because they are not mechanically strong enough to withstand the stress experienced when the device is operating, this can lead to cracking of electrode which automatically will affect conductivity within the electrode. Search for reliable material with good electrical conductivity and remarkable mechanical properties are envisaged to enhance performance of energy storage devices. Another solution to manage the physical deterioration of storage devices is to increase surface area of electrodes thereby improving the chemical reaction taking place within the device. Nanomaterials improve drastically with regards to surface area, hence ideal for electrode materials [109].

The charge storage mechanism for any supercapacitor is analyzed based on its energy and power densities defined by equation (1) below:

$$E = \frac{C\,x\,V^2}{2} \quad \text{and} \quad P = \frac{V^2}{4R} \qquad \ldots\ldots\ldots\ldots\ldots\ldots\ldots\ldots (1)$$

Where C is the capacitance in Farad, V is the operating potential in volt; R is the resistance in Ohm. Power density is improved with an increase in the potential range across the supercapacitor and reducing the resistance, but capacitance depends on the type of electrode material used and the storage mechanism [110].

Evaluation of supercapacitors employs similar criteria for energy storage systems, i.e. cyclic voltammetry (CV), galvanostatic charge/discharge (GCD) and electrochemical impedance spectroscopy (EIS). These are employed to evaluate parameters like specific capacitance, energy density, power density, series resistance, cycling life and rate capability. [111-113]. It is these electrochemical properties which are used to characterize supercapacitors (electrode materials) [114-116]. Collectively, these techniques complement each other, giving a broad understanding of the energy storage mechanism and the surface phenomena between the electrode and the electrolyte.

1.2.5.2. Hydrogen evolution reaction (energy generation)

Hydrogen is a good candidate to substitute the use of fossil fuels due to its high energy density and it is pollution-free [117]. Hydrogen, as abundant, clean and renewable energy source, is a suitable candidate to replace the depleting fossil fuels in the near future [118, 119].

There are two important technologies for industrial production of hydrogen, namely: electrochemical and photoelectrochemical electrolysis of water. While these approaches are environmental-friendly, the efficiency of sunlight-driven water splitting reaches only 12.3% for generating H_2. This calls for the use of electrolysis of water as the most viable route towards scaling up in the production of H_2.

The modern large-scale production of H_2 depends on the method of steaming methane gas, as shown in the following equations:

$$CH_{4(g)} + H_2O_{(g)} \longrightarrow CO_{(g)} + 3H_{2(g)} \ldots\ldots\ldots\ldots\ldots\ldots (2)$$

$$CO_{(g)} + H_2O_{(g)} \longrightarrow CO_{2(g)} + H_{2(g)} \quad \ldots\ldots\ldots\ldots\ldots\ldots (3)$$

Equation (2) involves high energy input which goes up to ΔH_{298} = -206 kJ mol^{-1} while equation (3) needs an energy input of ΔH_{298} = -41 kJ mol^{-1}. These reactions need high energy input (heat) and produce huge amount of carbon dioxide into the atmosphere, hence, contributing to global warming. This cannot be considered to be a favourable green route for the production of H_2 [120]. The greener route would be the electrolysis of water which produces H_2 with no greenhouse gas emissions.

1.2.5.3. Water Splitting Reaction

Hydrogen has been regarded as the cleanest chemical fuel and hence it is among the major sources of sustainable energy [121]. It is thus considered a sustainable energy carrier that can replace depleting fossil fuels and also tackle environmental problems that comes with fossil fuels [122, 123].

Hydrogen is the most abundant element in the universe, accounting for 75% by mass though it is not commonly found in its pure form due to its high reactivity. Hydrogen is also abundantly present in water, thus, any endeavor to split water into H_2 and O_2 would be a promising means to renewable and sustainable energy. Progress in water splitting reactions has been achieved by use of Pt as cathodic material. However, poor abundance and high cost for Pt has limited its use for cost-effective hydrogen evolution reaction (HER) and oxygen evolution reaction (OER) [124, 125].

Search for a replacement of Pt as cathodic material for HER would need an understanding of the mechanism that is undertaken to break water into H_2 and O_2. The cathodic reaction is represented in equation (4) below:

$$2H^+ + 2e^- \longrightarrow H_2 \quad \ldots\ldots\ldots\ldots\ldots\ldots (4)$$

The burning of hydrogen would result into equation (5). The energy produced by burning one molecule of hydrogen is given by ΔH = -286 kJ/mol which can be equated to about 142 MJ/Kg energy density at 700 bar pressure. This is far greater than the energy density for methane which is just 55.5 MJ/Kg when in a compressed state. Such huge amount of energy can be used in so many other technologies such as cars running on H_2 engines.

$$2H_{2(g)} + 1/_2\, O_{2(g)} \longrightarrow H_2O_{(l)} \quad \text{..... (5)}$$

The OER is another half electrochemical cell for water splitting process. Equation (6) represents this process which is driven by four electrons and hence becoming much more complicated if compared to HER reaction.

$$2H_2O \longrightarrow O_2 + 4H^+ + 4e^- \text{..... (6)}$$

The best catalysts for this reaction are iridium and ruthenium oxides, particularly in acidic media. However, their natural abundance is very limited. They are also costly and they cause electrochemical instability during reaction, hence, rendering them ineffective material for OER [126].

Extensive work has been carried out to look for a catalyst that can replace Pt for the HER/OER reaction. Layered transition metal dichalcogenides like WS_2, MoS_2, $MoSe_2$ and WSe_2 have been shown to have higher catalytic activity to HER [127-129]. Other potential candidates are metal phosphides and metal alloys such as Ni_3S_2, CoS_2 and $NiCo_2S_4$ which seem to have surpassing character for the catalytic performance in water splitting reactions [130, 131].

1.3. Statement of the research problem

Dithiocarbamates are versatile ligands, i.e. they provide endless opportunities regarding their derivatization. In organic synthesis, they are important synthetic intermediates; they also can bind to a range of transition metals of different oxidation states to form corresponding metal complexes [132]. As a result, using dithiocarbamates as SSPs for nanomaterials synthesis and thin films broadens the scope that needs to be explored [14,36,45]. Nanomaterials synthesized by using selected dithiocarbamate metal complexes give specific pure phases which can be tuned to a particular technological application. Energy crisis around the globe has prompted researchers to search into targeted dithiocarbamate ligands, which will ultimately produce nanomaterial applicable in magnetism and energy application.

According to various energy specialists, the fossil-fuel reserve is rapidly depleting and it can support a limited number of years for petroleum, 60 years for natural gas and ~156 years for coal [133, 134]. The predicted scarcity of fossil-fuel reserve coupled with the increasing energy consumption threatens energy and economic security worldwide. Thus, to search into the use of

nanostructured materials which has proved to be promising candidate for synthesis of supercapacitors with higher efficiency and making electrode nanomaterial that can catalyse electrolysis of water for HER and OER reaction is highly needed as a means to solve the energy crises worldwide and hence alleviate the severe environmental threats associated with the use of fossil fuels.

The main motivation of this work is to attain a great energy security by searching into nanomaterials that can reduce the dependence on depleting nonrenewable sources of energy. This can be achieved by synthesizing nanomaterials which would effortlessly generate and/or store energy, hence, be able to sustain our energy economy and environment. A secondary objective is to prepare nanoparticles and subsequently study their magnetic properties. To achieve this goal, some methods need to be devised so as to obtain different, pure phases of nickel and cobalt sulfide nanoparticles and thin films produced through variation of reaction parameters. This would thus allow their evaluation in different applications with aims of expanding contributions to the body of knowledge in the field of nanosciences. Selected dithiocarbamate ligands and their Ni(II) and Co(III) complexes are synthesized, characterized fully and evaluated as single source precursors to fabricate binary and ternary nanoparticles and thin films. This provides an opportunity to evaluate the as-prepared nanoparticles and thin films in magnetic, H_2/O_2 evolution reactions and supercapacitance applications.

1.4. Scope of the work

The technological application of TMS materials in their thin film and monodispersed nanoparticulate forms have motivated continued research on novel and/or improved SSPs. In this research project, binary and ternary nanomaterials (including thin films) of cobalt and nickel sulfides were fabricated from the corresponding heterocyclic dithiocarbamate SSPs. The SSPs were derived from four different dithiocarbamate ligands namely: piperidine, tetrahydroisoquinoline, 4-morpholine and 1-ethylpiperazine. Reaction parameters which include temperature, time, nature of capping agent, among others, were investigated to gain particle size, shape and morphology control of the nanomaterials and thin films. Well-suited capping agents capable of stabilizing and passivating the nanoparticles during solvent thermolysis reactions are key research areas in nanotechnology; oleylamine (OLA), hexadecylamine (HDA), and

dodecylamine (DDA) were used to passivate the fabricated nanoparticles. Thin films were deposited from the solutions of complexes in chloroform by the AACVD technique. The resulting nanomaterials were thoroughly investigated, where applicable, for their efficacy in applications which include magnetism, H_2/O_2 evolution and capacitance.

1.5. Aim and objectives of the work

The aim of this project was to explore the use of different heterocyclic dithiocarbamate complexes as SSPs for the fabrication of Ni and Co sulfide nanoparticle and thin films for magnetic and energz applications.

The objectives included:

1. Synthesis and characterization of Co and Ni piperidine, tetrahydroisoquinoline, 4-morphiline and 1-ethylpiperazine dithiocarbamates complexes.
2. Synthesis and characterization of DDA, HDA and OLA-capped Ni_xS_y and Co_xS_y nanoparticles by the solvent thermolysis of the complexes.
3. Synthesis of multiple-phase NiS thin films by AACVD at different decomposition temperatures
4. Synthesis of Ni and Co-rich ternary $Ni_xCo_{3-x}S_4$ nanoparticles through the solvent thermolysis method using a dual molecular precursor route.
5. Establishment and effectiveness of $Ni_xCo_{3-x}S_4$ ternary material in the electrocatalytic and electrochemical reactions, i.e. energy generation and energy storage application.

1.6. Thesis layout

Chapter	Description
1	The chapter is the introduction and literature review outlining an overview summary on the scientific research and theories related to areas of research followed in this thesis.
2	The chapter outlines the synthesis, characterization, results and discussion on piperidine, tetrahydroisoquinoline and ethylpiperazine dithiocarbamate nickel complexes and the corresponding Ni_xS_y nanoparticles. X-ray single crystal structures of two complexes are elucidated and magnetic properties for some Ni_xS_y phases are elaborated in detail.
3	The chapter is based on the synthesis and results obtained when three chloroform solutions of Ni(II) piperidine, tetrahydro-isosquinoline, ethyl-piperazine dithiocarbamates are employed in the AACVD method to deposit NiS thin films.
4	The chapter reports a synthesis of a novel Co(III) complex of 4-morpholine dithiocarbamate; crystal structure and related information is provided. The synthesis and characterization of the nanoparticles obtained from the solvent thermolysis which uses OLA as a capping agent is elaborated. The as-prepared nanoparticles are tested for electrocatalytic and electrochemical reactions.
5	The chapter reports the synthesis of the ternary $Ni_xCo_{3-x}S_4$ nanoparticles through the dual molecular precursor route using the solvent thermolysis method. The resulting nanomaterials are tested for their electrocatalytic and electrochemical applications.
6	The chapter gives a summary of the results obtained from this work, the challenges and the recommendation for future work

1.7. References

[1] T.C. Prathna, L. Mathew, N. Chandrasekaran, A.M. Raichur, A. Mukherjee, Biomimetic Synthesis of Nanoparticles : Science , Technology & Applicability, 2010.

[2] R. Tilley, Chem. New Zeal. (2008) 146–150.

[3] M. Niederberger, H. Cölfen, Phys. Chem. Chem. Phys. 8 (2006) 3271–87.

[4] C.B. Murray, D.J. Norris, M.G. Bawendi, J. Am. Chem. Soc. 115 (1993) 8706–8715.

[5] L. Cademartiri, G. a Ozin, Philos. Trans. A. Math. Phys. Eng. Sci. 368 (2010) 4229–48.

[6] N. Kumar, N. Raman, A. Sundaresan, Zeitschrift Für Anorg. Und Allg. Chemie (2014).

[7] M. Afzaal, M.A. Malik, P. O'Brien, J. Mater. Chem. 20 (2010) 4031.

[8] M. Banerjee, L. Chongad, A. Sharma, V. Bhawan, K. Road, G. Arts, I. Road, 2 (2013) 326–329.

[9] G. Hogarth, K.T. Holman, A. Pateman, A. Sella, J.W. Steed, I. Richards, Dalton Trans. (2005) 2688–95.

[10] A.M. Cotero-Villegas, P.G. y García, H. Höplf-Bachner, M. del C. Pérez-Redondo, P. Martínez-Salas, M. López-Cardoso, R.C. Olivares, J. Organomet. Chem. 695 (2010) 1246–1252.

[11] S.E. Al-mukhtar, 24 (2013) 50–59.

[12] A. Gölcü, Transit. Met. Chem. 31 (2006) 405–412.

[13] T. Mthethwa, V.S.R.R. Pullabhotla, P.S. Mdluli, J. Wesley-Smith, N. Revaprasadu, Polyhedron 28 (2009) 2977–2982.

[14] L.D. Nyamen, V.S. Rajasekhar Pullabhotla, A.A. Nejo, P. Ndifon, N. Revaprasadu, New J. Chem. 35 (2011) 1133.

[15] L.D. Nyamen, A. a. Nejo, V.S.R. Pullabhotla, P.T. Ndifon, M.A. Malik, J. Akhtar, P. O'Brien, N. Revaprasadu, Polyhedron 67 (2014) 129–135.

[16] H. Nabipour, Sh. Ghammamy, Sh. Ashuri and Z.Sh. Aghbolagh, *Org.Chem. J.*, (2010) 2, 75.

[17] D.T. Sakhare, T.K. Chondhekar, S.G. Shankarwar and A.G. Shankarwar, *Adv. Appl. Sci. Res.*, (2015) **6**, 10.

[18] G.M. Pieper, V. Nilakantan, G. Hilton, N.L.N. Halligan, C.C. Felix, B Kampalath, A.K. Khanna, A.M. Roza, C.P. Johnson, M.B. Adams, Am. J. Physiol. Heart Circ. Physiol. (2003); 284: H1542–H1551

[19] E.R.T. Tiekink, Appl. Organomet. Chem. (2008), 22, 533–550

[20] D.C. Menezes, G.M. de Lima, A.O. Porto, C.L. Donnici, J.D. Ardisson, A.C. Doriguetto, J. Ellena, Polyhedron (2004), 23, 2103–2109.

[21] R. Kadu, H. Roy, V.K. Singh, Appl. Organomet. Chem. (2015), 29, 746–755.

[22] N. Awang, N.H. Zakri, N.M. J. Chem. Pharm. Res. (2016), 8, 862–866

[23] E.N. Iornumbe, S.G. Yiase, R. Sha'Ato, Int. J. Sci. Res. (2016), 5, 1610–1617

[24] N. Hollingsworth, A. Roffey, H.-U. Islam, M. Mercy, A. Roldan, W. Bras, M. Wolthers, C. R. A. Catlow, G. Sankar, G. Hogarth and N. H. de Leeuw, Chem. Mater., (2014), 26, 6281–6292.

[25] C. Gervas, S. Mlowe, M. P. Akerman, I. Ezekiel, T. Moyo and N. Revaprasadu, *Polyhedron* 2017, 122, 16.

[26] J. Wang, S. Chou, S. Chew, J. Sun, M. Forsyth, D. Macfarlane, H. Liu, Solid State Ionics 179 (2008) 2379–2382.

[27] L.P. Deshmukh, S.T. Mane, 6 (2011) 931–936.

[28] J. Xiao, L. Wan, S. Yang, F. Xiao, S. Wang, Nano Lett. 14 (2014) 831–838.

[29] Malik M A and O'Brien P, Organometallic and Metallo-Organic Precursors for Nanoparticles, Springer Berlin Heidelberg, Berlin, Heidelberg, 2005.

[30] S.F. Wuister, A. Meijerink, J. Lumin. 102–103 (2003) 338–343.

[31] G. Kraeuter, P. Favreau, W.S.J. Rees, Chem. Mater. 6 (1994) 543–549.

[32] S.D. Burnside, V. Shklover, C. Barbé, P. Comte, F. Arendse, K. Brooks, M. Grätzel, Chem. Mater. 10 (1998) 2419–2425.

[33] Y. Li, H. Wang, H. Zhang, P. Liu, Y. Wang, W. Fang, H. Yang, Y. Li, H. Zhao, Chem. Commun. (Camb). 50 (2014) 5569–71.

[34] N. Alam, M.S. Hill, G. Kociok-Köhn, M. Zeller, M. Mazhar, K.C. Molloy, Chem. Mater.

20 (2008) 6157–6162.

[35] P. O'Brien, J. Waters, Chem. Vap. Depos. 12 (2006) 620–626.

[36] P. O'Brien, J.H. Park, J. Waters, Thin Solid Films 431–432 (2003) 502–505.

[37] G. KULLERUD, R.A. YUND, J. Petrol. 3 (1962) 126–175.

[38] J.C. Barry, S. Ford, J. Mater. Sci. 36 (2001) 3721–3730.

[39] S.D. Sartale, C.D. Lokhande, 72 (2001) 101–104.

[40] K. Ramasamy, M.A. Malik, P. O'Brien, J. Raftery, Dalton Trans. 39 (2010) 1460–3.

[41] K. Ramasamy, M. a. Malik, P. O'Brien, J. Raftery, M. Helliwell, Chem. Mater. 22 (2010) 6328–6340.

[42] G. Wang, L. Zhang, J. Zhang, Chem. Soc. Rev. 41 (2012) 797–828.

[43] A.L. Abdelhady, M.A. Malik, P. O'Brien, F. Tuna, J. Phys. Chem. C 116 (2012) 2253–2259.

[44] D.P. Dinega, M.G. Bawendi, Angew. Chemie Int. Ed. 38 (1999) 1788–1791.

[45] K. Ramasamy, W. Maneerprakorn, M.A. Malik, O. Brien, (2010).

[46] V.F. Puntes, K.M. Krishnan, A.P. Alivisatos, Science (80-.). 291 (2001) 2115–2117.

[47] S. Ariponnammal, T. Srinivasan, 2 (2013) 102–105.

[48] N. Rumale, S. Arbuj, G. Umarji, M. Shinde, U. Mulik, A. Pokle, D. Amalnerkar, 2013 (2013) 28–31.

[49] P. Christian, P. O'Brien, J. Mater. Chem. 18 (2008) 1689.

[50] J. An, B. Tang, X. Ning, J. Zhou, W. Xu, B. Zhao, C. Corredor, J.R. Lombardi, J. Phys. Chem. C 111 (2007) 18055–18059.

[51] S.-M. Lee, S.-N. Cho, J. Cheon, Adv. Mater. 15 (2003) 441–444.

[52] F. Srouji, M. Afzaal, J. Waters, P. O'Brien, Chem. Vap. Depos. 11 (2005) 91–94.

[53] M. Chunggaze, M. Azad Malik, P. O'Bricn, J. Mater. Chem. 9 (1999) 2433–2437.

[54] Q. Zhao, Z. Yan, C. Chen, J. Chen, Chem. Rev. 117 (2017) 10121–10211.

[55] D.P. Shoemaker, J. Li, R. Seshadri, J. Am. Chem. Soc. 131 (2009) 11450–11457.

[56] C. Hsu, H.M. Chen, Res. Contract Beamline (2017).

[57] C. Xia, P. Li, A.N. Gandi, U. Schwingenschlögl, H.N. Alshareef, Chem. Mater. 27 (2015) 6482–6485.

[58] L. Yu, L. Zhang, H. Bin Wu, X.W.D. Lou, Angew. Chemie - Int. Ed. 53 (2014) 3711–3714.

[59] M. Chauhan, K.P. Reddy, C.S. Gopinath, S. Deka, ACS Catal. 7 (2017) 5871–5879.

[60] T. Hinotsu, B. Jeyadevan, C.N. Chinnasamy, K. Shinoda, K. Tohji, J. Appl. Phys. 95 (2004) 7477–7479.

[61] L. He, W. Zheng, W. Zhou, H. Du, C. Chen, L. Guo, J. Phys. Condens. Matter 19 (2007).

[62] S.K. Shrama, N. Saurakhiya, S. Barthwal, R. Kumar, A. Sharma, Nanoscale Res. Lett. 9 (2014) 1–17.

[63] S. Ammar, B. Cruz-Franco, R. Valenzuela, A.M. Bolarin-Miro, F. Sanchez de Jesus, S. Nowak, T. Gaudisson, F. Mazaleyrat, R. Ortega-Zempoalteca, G. Vazquez-Victorio, IEEE Trans. Magn. 50 (2014) 1–6.

[64] V. Hnizdo, American Journal of Physics, (1997), 65(1), 55-65.

[65] A.H. Lu, E.L. Salabas, F. Schüth, Angew. Chemie - Int. Ed. 46 (2007) 1222–1244.

[66] M. Angelakeris, M. Farle, V. Ntomprougkidis, K. Simeonidis, M. Spasova, U. Wiedwald, N. Maniotis, A. Makridis, T. Samaras, R. Salikhov, A. Terzopoulou, E. Myrovali, O. Kalogirou, D. Sakellari, Sci. Rep. 6 (2016) 1–11.

[67] J.Q. He, V. V. Volkov, M. Beleggia, T. Asaka, J. Tao, M.A. Schofield, Y. Zhu, Phys. Rev. B - Condens. Matter Mater. Phys. 81 (2010).

[68] E. C. Stoner and E .P. Wohlfarth , Trans. Roy. Soc. London (1948) A 240, 599.

[69] A. K. Gupta, M. Gupta, Biomaterials (2005), 26, 3995.

[70] S. Chikazumi, S. Taketomi, M. Ukita, M. Mizukami, H. Miyajima, M. Setogawa, Y. Kurihara, J. Magn. Magn. Mater. (1987), 65, 245.

[71] T. Hyeon, Chem. Commun. (2003), 927.

[72] S. Mornet, S. Vasseur, F. Grasset, P. Verveka, G. Goglio, A. Demourgues, J. Portier, E. Pollert, E. Duguet, Prog. Solid State Chem. (2006), 34, 237.

[73] D. W. Elliott, W.-X. Zhang, Environ. Sci. Technol. (2001), 35, 4922.

[74] X. Chen, Z. Wang, X. Wang, J. Wan, J. Liu and Y. Qian, Inorg.Chem., (2005), 44, 951–954.

[75] H. Wang and I. Salveson, Phase Transform., (2005), 78, 547.

[76] S. Mlowe, D. J. Lewis, M. A. Malik, J. Ra□ery, E. B. Mubofu, P. O'Brien and N. Revaprasadu, Dalton Trans., 2016, 45, 2647–2655.

[77] J. Puthussery, S. Seefeld, N. Berry, M. Gibbs and M. Law, J. Am. Chem. Soc., 2011, 133, 716–719.

[78] J. Wu, Z. Lan, J. Lin, M. Huang, Y. Huang, L. Fan and G. Luo, Chem. Rev., 2015, 115, 2136

[79] IRENA, IEA and REN21, Renewable Energy Policies in a Time of Transition, 2018

[80] M.C. Dos Santos, O. Kesler, A.L.M. Reddy, J. Nanomater. 2012 (2012) 2–4.

[81] K. Liu, Y. Liu, D. Lin, A. Pei and Y. Cui, Sci. Adv., (2018), 4, 9820

[82 W. Zuo, R. Li, C. Zhou, Y. Li, J. Xia and J. Liu, Adv. Sci., 2017, 4, 1600539

[83] P. Simon, Y. Gogotsi, Nat. Mater. 7 (2008) 845–854.

[84] H. Wang, H.S. Casalongue, Y. Liang, H. Dai, J. Am. Chem. Soc. 132 (2010) 7472–7477.

[85] Z. Chen, Z. Wan, T. Yang, M. Zhao, X. Lv, H. Wang, X. Ren, X. Mei, Sci. Rep. 6 (2016) 1–8.

[86] L. Yu, L. Zhang, H. B. Wu, X. W. D. Lou, Angew. Chem. Int. Ed. 2014, 53, 3711– 3714; Angew. Chem. 2014, 126, 3785 –3788.

[87] R. Zou, Z. Zhang, M. F. Yuen, J. Hu, C. S. Lee, W. Zhang, Sci. Rep. 2015, 5, 7862 –7868.

[88] X. J. Chen, D. Chen, X. Y. Guo, R. M. Wang, H. Z. Zhang, ACS Appl. Mater. Interfaces, 2017, 9, 18774 – 18781.

[89] F. L. Luo, J. Li, H. Y. Yuan, D. Xiao, Electrochim. Acta 2014, 123, 183 – 189.

[90] J. G. Wang, D. D. Jin, R. Zhou, C. Shen, K. Y. Xie, B. Q. Wei, J. Power Sources

2016, 306, 100 –106.

[91] R. J. Zou, Z. Y. Zhang, M. F. Yuen, M. L. Sun, J. Q. Hu, C. S. Lee, W. J. Zhang, NPG Asia Mater. 2015, 7, e195.

[92] F. Zhu, H. Xia, T. Feng, Mater. Technol. 2015, 30, A53– A57.

[93] R. C. Jin, G. Liu, C. P. Liu, L. Sun, Mater. Res. Bull. 2016, 80, 309 –315.

[94] N. Kurra, C. Xia, M. N. Hedhili, H. N. Alshareef, Chem. Commun. 2015, 51, 10494 –10497.

[95] Q. Jiang, N. Kurra, C. Xia, H. N. Alshareef, Adv. Energy Mater. 2016, 1601257

[96] J. H. Wu, S. Dou, A. Shen, X. Wang, Z. L. Ma, C. Ouyang, S. Y. Wang, J. Mater. Chem. A 2014, 2, 20990 –20995.

[97] Z. Y. Zhang, X. G. Wang, G. L. Cui, A. H. Zhang, X. H. Zhou, H. X. Xu, L. Gu, Nanoscale 2014, 6, 3540 – 3544.

[98] D. N. Liu, Q. Lu, Y. L. Luo, X. P. Sun, A. M. Asiri, Nanoscale 2015, 7, 15122– 15126.

[99] Q. Liu, J. T. Jin, J. Y. Zhang, ACS Appl. Mater. Interfaces 2013, 5, 5002 – 5008.

[100] S. H. Park, Y. K. Sun, K. S. Park, K. S. Nahm, Y. S. Lee, M. Yoshio, Electrochim. Acta 2002, 47, 1721 – 1726.

[101] C. Xia, P. Li, J. Li, Q. Jiang, X. X. Zhang, H. N. Alshareef, Chem. Mater. 2017, 29, 690 –698.

[102] C. Xia, P. Li, A. N. Gandi, U. Schwingenschlçgl, H. N. Alshareef, Chem. Mater. 2015, 27, 6482 –6485.

[103] X. B. Liu, Z. P. Wu, Mater. Lett. 2017, 187, 24 –27.

[104] Z. C. Li, Y. Qu, M. G. Wang, Y. M. Hu, J. Han, L. Fan, R. Guo, Colloid Polym. Sci. 2016, 294, 1325 –1332

[105] L. Shen, Y. Le, H. B. Wul, X. Y. Yul, X. Zhang, X. W. Lou, Nat. Commun.2015, 6, 6694– 6701

[106] T. Yan, R. Y. Li, Z. J. Li, Mater. Lett. 2016, 167, 234– 237.

[107] T. Peng, Z. Y. Qian, J. Wang, D. L. Song, J. Y. Liu, Q. Liu, P. Wang, J. Mater. Chem. A 2014, 2, 19376 –19382.

[108] R. Jin, D. Liu, C. Liu, G. Liu, RSC Adv. 5 (2015) 84711–84717.

[109] C. Zhang, S.-H. Park, A. Seral-Ascaso, S. Barwich, N. McEvoy, C.S. Boland, J.N. Coleman, Y. Gogotsi, V. Nicolosi, Nat. Commun. 10 (2019) 849.

[110] S. Bhoyate, K. Mensah-Darkwa, P. K. Kahol and R. K. Gupta, Curr. Graphene Sci., (2017), 1, 26.

[111] A. Divyashree, G. Hegde, RSC Adv. (2015), 5, 88339–88352

[112] K. Liu, Y. Liu, D. Lin, A. Pei and Y. Cui, Sci. Adv., 2018, 4, 9820

[113] M.F. El-Kady, V. Strong, S. Dubin, R.B. Kaner, Science (2012), 335, 1326–1330

[114] C. Peng, S. Zhang, X. Zhou, G.Z. Chen, Energy Environ. Sci. (2010), 3, 1499–1502

[115] C.X. Guo, C.M. Li, Energy Environ. Sci. (2011), 4, 4504–4507

[116] Q. Cheng, J. Tang, J. Ma, H. Zhang, N. Shinya, L.-C.Qin, Phys. Chem. Chem. Phys. (2011), 13, 17615–17624.

[117] G. Nicoletti, N. Arcuri, G. Nicoletti, R. Bruno, Energy Convers. Manag. 89 (2015) 205–213.

[118] C.C. Hou, Q. Li, C.J. Wang, C.Y. Peng, Q.Q. Chen, H.F. Ye, W.F. Fu, C.M. Che, N. López, Y. Chen, Energy Environ. Sci. 10 (2017) 1770–1776

[119] C. Tang, N.Y. Cheng, Z.H. Pu, W. Xing, X.P. Sun, Angew. Chem. Int. Ed. 54 (2015) 9351–9355.

[120] R.M. Navarro, M.A. Peña, J.L.G. Fierro, Chem. Rev. 107 (2007) 3952–3991.

[121] Y. Ge, J. Wu, X. Xu, M. Ye, J. Shen, Int. J. Hydrogen Energy 41 (2016) 19847–19854.

[122] G. D. Berry, A. D. Pasternak, G. D. Rambach, J. R. Smith, and R. N. Schock, "Hydrogen as a future transportation fuel," *Energy*, vol. 21, no. 4, pp. 289–303, 1996

[123] B. Johnston, M. C. Mayo, and A. Khare, "Hydrogen: the energy source for the 21st century," *Technovation*, vol. 25, pp. 569–585, 2005

[124] H.A. Gasteiger, S.S. Kocha, B. Sompalli, F.T. Wagner, Appl. Catal. B Environ. 56 (2005) 9–35.

[125] J.X. Wang, Y. Zhang, C.B. Capuano, K.E. Ayers, Sci. Rep. 5 (2015) 1–8.

[126] D.H. Youn, Y. Bin Park, J.Y. Kim, G. Magesh, Y.J. Jang, J.S. Lee, J. Power Sources 294 (2015) 437–443.

[127] J. Deng, H. Li, J. Xiao, Y. Tu, D. Deng, H. Yang, H. Tian, J. Li, P. Ren, X. Bao, Energy Environ. Sci. 8 (2015) 1594–1601.

[128] A. Irshad, N. Munichandraiah, ACS Appl. Mater. Interfaces 9 (2017) 19746–19755.

[129] H. Li, C. Tsai, A.L. Koh, L. Cai, A.W. Contryman, A.H. Fragapane, J. Zhao, H.S. Han, H.C. Manoharan, F. Abild-Pedersen, J.K. Nørskov, X. Zheng, Nat. Mater. 15 (2016) 48–53.

[130] L.L. Feng, G. Yu, Y. Wu, G.D. Li, H. Li, Y. Sun, T. Asefa, W. Chen, X. Zou, J. Am. Chem. Soc. 137 (2015) 14023–14026.

[131] D. Liu, Q. Lu, Y. Luo, X. Sun, A.M. Asiri, Nanoscale 7 (2015) 15122–15126.

[132] K.V. Gopal, P.S. Jyothi, P.A.G. Raju, K. Rameshbabu, J. Sreeramulu, 5 (2013) 50–59.

[133] A. Midilli, M. Ay, I. Dincer, and M. A. Rosen, *Renewable and Sustainable Energy Reviews*, (2005) 9, 3, 255–271.

[134] British Petroleum, "Putting energy in the spotlight-BP statistical review of World Energy," 2005, http://www.nioclibrary.ir/free-e-resources/BP%20Statistical%20Review%20of%20World%20Energy/statistical review of world energy full report 2005.pdf

CHAPTER TWO

SYNTHESIS OF RARE PURE PHASE Ni_3S_4 AND Ni_3S_2 NANOPARTICLES IN DIFFERENT PRIMARY AMINE COORDINATING SOLVENTS

2.1 Introduction

The binary nickel sulfide system has raised interest because of its multiplicity of phases and stoichiometries which include NiS (α-NiS and ß-NiS), NiS_2, Ni_3S_2, Ni_3S_4, Ni_7S_6, Ni_6S_5 and Ni_9S_8 [1-4] The stability fields of naturally occurring mineral nickel-sulfur systems have been extensively studied and categorized as heazlewoodite (Ni_3S_2), polydymite (Ni_3S_4), millerite ($Ni_{1-x}S$) and vaesite (NiS_2) [1]. The phase diagram of the Ni-S system reveals that temperature, amount of nickel and/or sulfur present in the reaction system are key for the formation of a unique pure phase of nickel sulfide. Whilst a few of these phases have been identified as naturally occurring, others can be fabricated via laboratory protocols. The preparation of a specific Ni-S system is a challenge due not only to the existence of many phases within a single phase such as NiS (α-NiS and ß-NiS) but also to the co-existence of different phases making it difficult to extract a single pure phase [5].

The various phases of nickel sulfide nanomaterials are useful in many technological applications. NiS_2 has photocatalytic properties for hydrogen production and supercapacitors [6-8]. NiS has shown potential in dye-sensitized solar cells as counter electrodes, IR detectors and Li-ion storage applications [9-11]. Ni_3S_2 has been reported as a potent catalyst for water splitting reactions [12-14], whereas Ni_3S_4 has been reported to have applications in high performance supercapacitors [15, 16]. The low temperature heazlewoodite Ni_3S_2, NiS and Ni_7S_6 phases have been reported to have common physical features of creamy bright yellow colour and are not easily distinguished from each other [1]. Ni_3S_2 has two modifications namely α-Ni_3S_2 (healzlewoodite) at low temperature ($T \leq 838$ °C) and ß- Ni_3S_2 at higher temperature (wide range of temperature) [17]. Reports have shown that at temperatures above 556 ºC, Ni_3S_2 changes into $Ni_{3+x}S$ with an fcc crystal structure [18]. Both Ni_3S_2 and Ni_7S_6 are non-magnetic whereas NiS is semi-metallic in nature, a p-type semiconductor whose paramagnetism is temperature independent [3]. Ni_3S_4 polydymite has a cubic spinel crystal structure [19], which decomposes at higher temperatures (400 ºC) to form NiS and NiS_2.

Both nanocystalline NiS and Ni_3S_2 can be prepared by various methods. Keigo *et al.* [20] reported the synthesis of NiS, Ni_3S_2 and Ni_9S_8 in high boiling point coordinating or non-coordinating solvents. The formation of pure phases was influenced by time, temperature and boiling solvents. Salavati-Niasari *et al.* [21] were able to isolate NiS nanocrystals by using

microwave irradiation from organometallic complexes. The same group reported the use of nickel dithiosemicarbazide as a new precursor to obtain nickel sulfide nanoparticles [21, 22]. Karthikeyan *et al.* [23] used hydrothermal method to prepare nickel sulfide with EDTA as a capping group. The obtained nanocrystals were mixed phases of Ni_3S_4, NiS_2, NiS and $Ni_{17}S_{18}$. Ni_3S_4 has been observed to co-exist with other forms of the Ni-S system i.e. NiS and NiS_2. It is also a challenge to prepare this particular phase of nickel sulfide in the laboratory by a solid-state reaction method, since at higher temperatures (360 ºC) it is unstable [19]. The phase diagram of Ni-S system shows pure phase Ni_3S_4 to be stable up to 356 ºC [1, 14] and efforts to prepare it in laboratory have resulted in mixed phases [18]. Various researchers have reported the synthesis of Ni_3S_4 by the colloidal route [5, 16, and [24]. The solvent-less synthetic route produced mixed phases of NiS (millerite) and Ni_3S_4 [18, 25].

Single source precursors (SSPs) have been widely used in the synthesis of different metal sulfides and various phases of nickel sulfide [25-28]. Dithiocarbamate complexes, in particular have been extensively used for the preparation of nickel sulfide nanoparticles with different phases [29-33]. The decomposition patterns of dithiocarbamates promote the formation of a particular pure phase of nickel sulfide [29, 33]. For example, Hogarth and co-workers [33] showed that temperature and solvents are key determinants of Ni-S phase obtained. Roffey *et al.* [29] reported the use of dithiocarbamate complexes for the preparation of a wide range of phase-pure nickel sulfide particles by the manipulation of different reaction conditions.

In this chapter the use of *bis*(piperidinyldithiocarbamato)nickel(II) (**1**), *bis*(tetrahydroquinolinyldithiocarbamato)nickel(II) (**2**) and *bis*(*N'*-ethyl-*N*-piperazinylcarbodithioato-S,S')-Nickel(II) (**3**) complexes for the synthesis of pure phase of Ni_3S_4, Ni_3S_2 and mixed phase of nickel sulfide nanoparticles is reported. Magnetic measurements were showed to be phase dependent. Single crystal x-ray structures of complexes (**1**) and (**3**) are also elucidated [34].

2.2 Experimental details

2.2.1. Materials

Hexadecyalamine (HDA) 98%, oleylamine (OLA) 99%, dodecylamine (DDA), tri-n-octylphosphine (TOP) 90%, piperidine 99%, tetrahydroisoquinoline 99%, ethylpiperazine 99%, carbon disulfide 99% and nickel acetate tetrahydrate were purchased from Sigma Aldrich. Sodium hydroxide 98%, methanol 99.5%, chloroform, acetone and hexane were purchased from Merck. All chemicals were used as purchased without any further purification.

2.2.2. Synthesis of ligands

Carbon disulfide (6.00 mL, 100 mmol,) was added in small portions to an equimolar solution of sodium hydroxide (4.00 g, 100 mmol) in the corresponding 100 mmol of amine (piperidine, tetrahydroquinoline or ethylpiperazine, while being cooled in an ice bath at 0-5 °C. After 15 min of addition, a precipitate was formed. This was filtered off, dried in open air and then recrystallised in a mixture of acetone/petroleum ether. The crystalline, white-coloured material was filtered off, washed with chloroform and vacuum dried at room temperature.

$NaS_2C(NC_5H_{10})$ (Na-pip-dtc), yield: 90 %. ^{1}H NMR (400 MHz, D_2O): δ 1.41 (m, 2H, 3-CH_2), 1.53 (t, 2H, 4-CH_2), 4.28 (t, 2H, 2-CH_2). IR (ν_{max} in cm^{-1}, ATR): 967, ν(C=S); 1468, ν(C=N). Anal. Calc. for $C_6H_{10}NS_2Na$ (%): C, 35.80; H, 6.01; N, 6.96. Found (%): C, 35.90; H, 5.96; N, 6.92.

$NaS_2C(NC_9H_{10})$ (Na-thq-dtc), Yield: 72 %. ^{1}H NMR (400 MHz, CD_3OD): δ 2.07 (m, 2H, 3-CH2), 2.73 (t, 2H, 4-CH2), 4.58 (t, 2H, 2-CH2), 7.08–7.85 (m, 4H, Ar–H). IR (ν_{max} in cm^{-1}, ATR): $\nu_{(O-H)}$: 3250, $\nu_{(C=S)}$: 968, $\nu_{(C=N)}$: 1481. Anal. Calc. for $C_{10}H_{10}NS_2Na.2H_2O$: C, 44.93; H, 5.28; N, 5.24. Found: C, 45.07; H, 5.17; N, 5.32.

$NaS_2C(N_2C_6H_{13})$ (Na-Etpz-dtc), yield: 82 %. ^{1}H NMR (400 MHz, D_2O): δ 1.02 (t, 1H, -CH_3), 2.37 (m, 2H, 2-CH_2), 4.06 (t, 2H, 2-CH_2). IR (ν_{max} in cm^{-1}, ATR): 972, ν(C=S); 1457, ν(C=N). Anal. Calc. for $C_7H_{13}N_2S_2Na$ (%): C, 35.80; H, 6.01; N, 6.96. Found (%): C, 35.90; H, 5.96; N, 6.92.

2.2.3. Synthesis of complexes

A typical synthetic protocol is detailed as follows; $Ni(CH_3CO_2)_2 \cdot 4H_2O$ (4.10 g, 16.4 mmol) was dissolved in deionized water (25.0 mL), and then added drop-wise to the corresponding 100 mL aqueous solution of the 32.8 mmol dithiocarbamate ligand (Na-pip-dtc, Na-thq-dtc or Na-Etpz-dtc). The reaction mixture was stirred for 45 min, and the precipitate formed was vacuum filtered, washed with deionized water and dried in an oven at 80 ºC overnight. The corresponding complexes were analyzed as follows:

2.2.3.1. Bis(piperidinedithiocarbamato)nickel(II) complex (1)

$[Ni(pip\text{-}dtc)_2]$ (**1**), (where pip = piperidinyl and dtc = dithiocarbamato) yield: 79%. ^1H NMR (400 MHz, $CDCl_3$): δ 1.29 (m, 8H, 3-CH_2), 1.68 (t, 4H, 4-CH_2), 3.75 (t, 8H, 2-CH_2). Microanalysis: Calculated for $C_{12}H_{20}N_2NiS_4$: C, 38.00; H, 5.32; N, 7.39. Found: C, 38.12; H, 5.78; N, 7.24. IR (cm^{-1}, ATR): 998, *v* (C═S); 1438, *v* (C═N); 1507, *v* (C-N); 385-365, *v* (Ni–S).

2.2.3.2. Bis(tetrahydroquinolinedithiocarbamato)nickel(II) complex (2)

$[Ni(thq\text{-}dtc)_2]$ (**2**), (where thq = tetrahydroquinyl and dtc = dithiocarbamato) yield: 68%. ^1H NMR (400 MHz, $CDCl_3$): δ 2.99 (m, 4H, 3-CH_2), 3.99 (t, 4H, 4-CH_2), 4.99 (t, 4H, 2-CH_2), 7.20–7.50 (m, 8H, Ar–H). Microanalysis; Calculated for $C_{20}H_{20}N_2NiS_4$: C, 50.54; H, 4.24; N, 5.89. Found: C, 50.34; H, 4.52; N, 5.56. IR (cm^{-1}, ATR): 985, *v* (C═S); 1441, *v* (C═N); 1521, *v*(C-N); 385-365, *v* (Ni–S).

2.2.3.3. Bis(ethylpiperazinyldithiocarbamato)nickel(II) complex (3)

$[Ni(Etpz\text{-}dtc)_2]$ (**3**), (where Etpz = Ethylpiperazinyl and dtc = dithiocarbamato) yield: 81%. ^1H NMR (400 MHz, $CDCl_3$): δ 1.02 (m, 6H, 2-CH3), 2.37 (t, 8H, 4-CH_2), 2.38 (t, 8H, 4-CH_2). Microanalysis: Calculated for $C_{14}H_{26}N_4NiS_4$: C, 38.45; H, 5.99; N, 12.81. Found: C, 38.36; H, 6.01; N, 12.93. IR (cm^{-1}, ATR): 1006.93, *v* (C═S); 1431, *v* (C═N); 1499.69, *v* (C-N); 452-360, *v* (Ni–S).

2.2.4. Synthesis of NiS nanoparticles

In a typical procedure, 300 mg of complex (**1**) or (**2**) or (**3**) was dissolved in 3.0 mL of tri-*n*-octylphosphine (TOP) and injected in hot DDA in a three-necked flask at 190 ºC. A drop in reaction temperature of ~20 ºC was observed and the solution instantly turned to a blackish colour. The reaction temperature was raised back to 190 ºC and maintained for 2 hours, after which the heating was stopped. Ethanol was then added to flocculate the nickel sulfide nanoparticles. The DDA-capped nickel sulfide nanoparticles were separated by centrifugation followed by washing with ethanol and acetone. The above reaction procedure was repeated at reaction temperatures of 230 ºC and 270 ºC, using HDA and OLA as the capping agents.

2.2.5. Characterization techniques

2.2.5.1. Elemental CHNS/O analysis

Elemental (C, H, N) microanalysis provides sample's atomic composition. The analyses were performed on a Perkin-Elmer 2400 series II CHNS/O analyser.

2.2.5.2. Infra-red analysis (IR)

Infra-red spectra were recorded on a Bruker FT-IR Tensor 27 spectrophotometer, equipped with a standard ATR crystal cell detector. Analyses were performed in the wavenumber range of 200 – 4000 cm^{-1}.

2.2.5.3. Thermogravimetric analyses (TGA)

Thermogravimetric analysis was carried out at 10 °C min^{-1} heating rate using a Perkin Elmer Pyris 6 TGA up to 600 °C in a closed perforated aluminium pan under N_2 gas flow.

2.2.5.4. ^{1}H Nuclear Magnetic Resonance (NMR)

The ^{1}H NMR spectra of both the ligands and Ni(II) complexes were obtained using a Bruker advance III 400 MHz spectrophotometer equipped with trimethylsilane as an internal standard reference. The instrument is housed at the University of KwaZulu-Natal, South Africa.

2.2.5.5. Single crystal X-ray crystallography

Single crystal X-ray diffraction data for complexes were collected on a Bruker APEX diffractometer, using graphite monochromated Cu-K_α radiation (λ = 1.54178 Å). Hydrogen atoms were included in calculated positions, assigned isotropic thermal parameters and allowed to ride on their parent carbon atoms. All calculations were carried out using the SHELXTL software suite. Single crystal X-ray structure analyses: A green needle-like single crystal measuring about 0.21 × 0.04 × 0.02 mm for (**1**) and (**3**), was mounted on the goniometer of a Bruker Apex II Duo CCD diffractometer using a 500 µm-long needle cryoloop (MiTeGen®) mount. After initial suspension and selection in Paratone® oil. Intensity data were collected using Mo Kα radiation from an Incoatec® microsource (IuS, Quazar mirror optics) at a temperature of 100(2) K. The structures were solved using direct methods with SHELXS running in WinGX. The structures were refined using least-squares methods (SHELXL). All non-H-atoms were refined anisotropically; hydrogen atoms were included in calculated positions, assigned isotropic thermal parameters (U_{iso} for H atoms = 1.2U_{iso} for the attached C atom) and allowed to ride on their parent carbon atoms using the standard HFIX parameters in SHELXL.

2.2.5.6. Powder X-ray diffraction (p-XRD)

The p-XRD patterns were recorded in the high angle 2θ range of 20 - 80° using a Bruker AXS D8 Advance X-ray diffractometer, equipped with nickel filtered Cu Kα radiation (λ = 1.5406 Å) operated at 40 kV and 40 mA. Nanoparticles were placed on a sample holder and p-XRD patterns of the nanoparticles were recorded at room temperature in the high angle 2θ range (20 – 80°).

2.2.5.7. Transmission electron microscopy (TEM) and high resolution TEM (HRTEM)

TEM and HRTEM analyses were performed using a JEOL 1400 TEM and a JEOL 2100 HRTEM, respectively. Samples were prepared by placing a drop of dilute solution of NiS nanoparticles on Formvar-coated Cu grids (150 mesh) for TEM and holey carbon grids for HRTEM. The samples were allowed to dry completely at room temperature and viewed at an accelerating voltage of 120 kV (TEM) and 200 kV (HRTEM), and images captured digitally

using a Megaview III camera; stored and measured using Soft Imaging Systems iTEM software (TEM) and Gatan camera and Gatan software (HRTEM) were used.

2.2.5.8. Magnetic Measurement of Ni_3S_4 Samples.

The variation of room temperature hysteresis loops was investigated by using a Lakeshore model 735 vibrating sample magnetometer (VSM). In this case, the hysteresis loops were obtained in external applied magnetic fields of only up to 14 kOe.

2.2.5.9. Optical measurements

Optical absorption measurements were carried out using a Perkin-Elmer Lambda 1050 UV-Vis-NIR spectrophotometer. The samples were placed in silica cuvettes (1 cm path length), using hexane as a reference solvent.

2.3. Results and discussion

2.3.1. Characterization of the ligands and complexes

The nickel dithiocarbamato complexes used in this work were synthesized from cost-effective starting materials using relatively simple reaction protocols. They were found to be stable at ambient conditions similarly to other dithiolate complexes [32]. The complexes were obtained as green-coloured microcrystalline powders in good yields and their purity was confirmed by microelemtental analysis. IR spectroscopy revealed a very broad band around 3324-3367 cm^{-1} in the spectra of the ligands attributed to the ν (O-H) band for water, common for most dithiocarbamate ligands. This band was absent in the spectra of the complexes. Both the ligands and complexes showed bands in the 1466–1485 cm^{-1} region, corresponding to ν (C=N) and ν (C-N). The ν (C=S) band was observed at 999-975 cm^{-1} region in the spectra of the ligands. The increasing wavenumber shift of this ν (C=S) band in the complexes compared to the free ligand, in addition to the shuft of the strong bands attributed to ν (C-S), was indicative of a bidentate or slightly anisobidentate complexation. The TGA plots of the complexes displayed a single step decomposition pattern. The TGA plots showed a weight loss of 75 % (theoretical calc. 76%) at 353.5 °C, 71 % (theoretical calc. 80%) at 315.4 °C and 82 % (theoretical calc. 79%) at 323.95 °C for complexes (**1**), (**2**) and (**3**), respectively (Figure 2.1). This corresponds

mainly to the loss of the organic moiety of the complexes and some sulfur atoms. Generally, dithiocarbamate metal complexes decompose in solid state either by volatilization/sublimation (leaving behind almost no residue) or decomposition via a number of steps to yield respective metal sulfide residues [35]. Our metal complexes are in the latter category as the final residues displayed weights of 25%, 21% and 18% which were close to the calculated weights of 24%, 19% and 21% for NiS from complexes (**1**), (**2**) and (**3**), respectively.

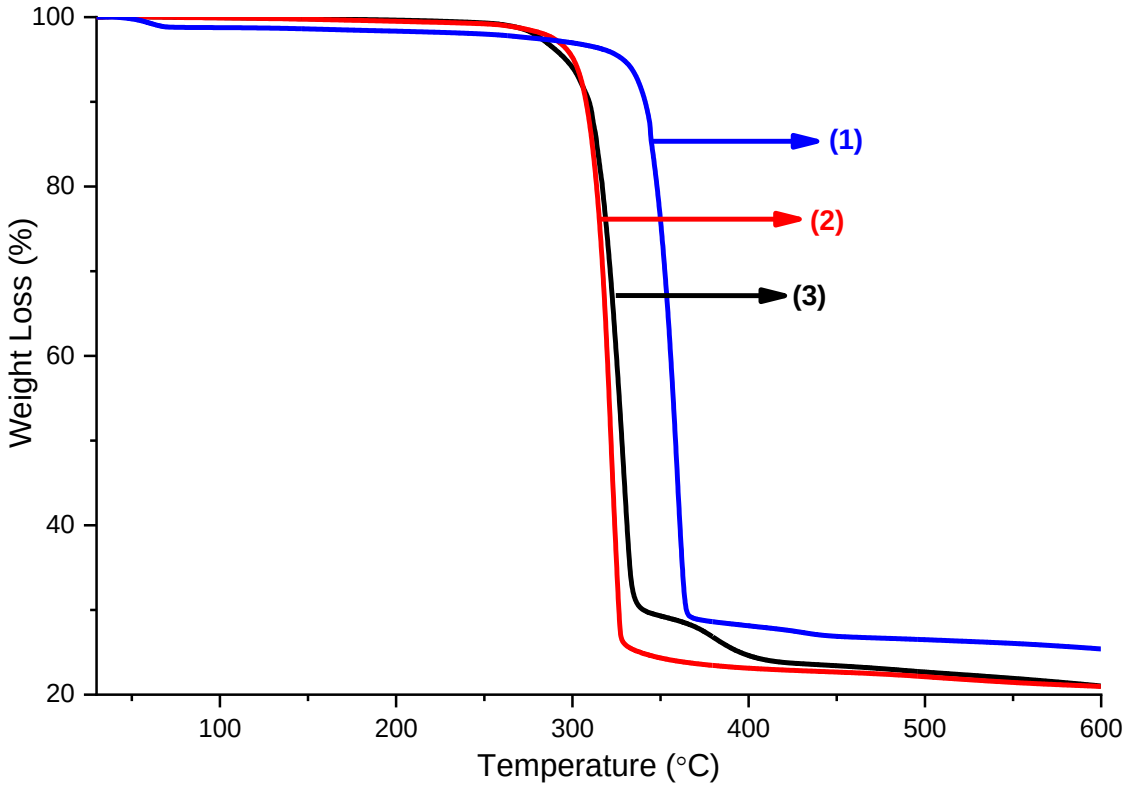

Figure 2.1: Thermogravimetric analysis (TGA) plots of complexes (**1**), (**2**) and (**3**)

2.3.2. Single-crystal X-ray structures for complexes (1) and (3)

The X-ray data for complex (**2**) were recorded recently by Hogarth *et al*. [36] at ambient temperature. The data collected need no further improvement as the instrumentations used to record them is recent and the crystal recorded was of high quality.

The X-ray data for complex (**1**) was previously recorded at ambient temperature by Radha *et al*. [34]. The data presented herein offer a significant improvement over that previously reported. Offering better data/parameter ratios as well as significant improvements in the R_1,

wR_2 and accuracy in the C–C bond lengths. Complex (**1**) crystallised in the monoclinic space group $P2_1/c$ with a half molecule in the asymmetric unit and Z = 2. The molecule has crystallographically imposed inversion symmetry with a centre of inversion located at the Ni(II) ion (Figure 2.2). Crystal data and structure refinement parameters for complex (**1**) are presented in Tables 2.1 and 2.2.

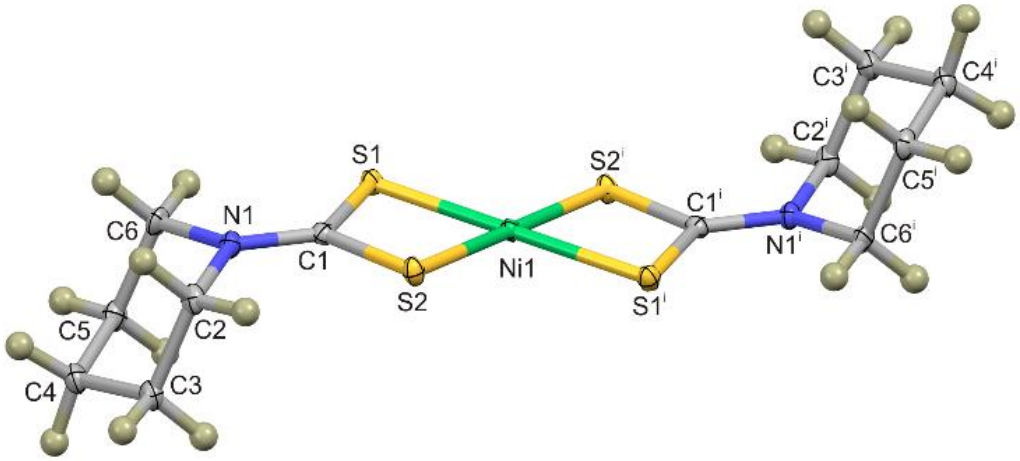

Figure 2.2: Displacement ellipsoid plot of complex (**1**) showing 50% probability surfaces. Hydrogen atoms have been rendered as spheres of arbitrary radius. The molecule has inversion symmetry with the centre of inversion located at the Ni(II) ion. Symmetry code: (i) -x, -y, -z (CCDC 1502999).

The d^8 Ni(II) ion has adopted a nominally square planar coordination geometry. The bond parameters are summarized in Table 2.1. The most notable deviation from an ideal square planar geometry lies in the intraligand S1–Ni1–S2 bond angle which measures 79.49(1)°, significantly more acute than the ideal bond angle of 90°. This acute bond angle is attributed to the small bite of the dithiocarbamate ligand and the associated 4-membered chelate ring. Consequently, the interligand S1–Ni1–S2 bond angle is obtuse, measuring 100.51(1)°. The S1-C1 and S2-C1 bond lengths measure 1.727(1) Å and 1.722(1) Å, respectively. These bond lengths are intermediate to those of a formal single or double C–S bond, highlighting the delocalisation of the dithiocarbamate ligand. Further, the C1-N1 bond length measures 1.321(2) Å. This is shorter than a typical sp^2 C–N single bond (1.377 Å) [37] suggesting a portion of double bond character and illustrating further delocalisation.

Table 2.1: Selected bond parameters of crystal structure for complex (**1**).

Bond	Length (Å)	Bond	Angle (°)
Ni1–S1	2.2010(3)	S2–Ni1–S1 (intraligand)	79.49(1)
Ni1–S2	2.2117(4)	S2–Ni1–S1 (interligand)	100.51(1)
S1–C1	1.727(1)	S1–C1–N1	125.4(1)
S2–C1	1.722(1)	S2–C1–N1	124.8(1)
C1–N1	1.321(2)		

The four coordinating atoms and the metal ion are planar by definition; however, this planarity does not extend to the C–N bond which shows a significant out-of-plane distortion. The atoms C1 and N1 are displaced from the 5-atom mean plane defined by the coordination sphere by 0.132(1) Å and 0.346(1) Å, respectively. The piperidine rings are approximately perpendicular to the coordination sphere and are in a *trans*-configuration. This geometry leads to a herringbone pattern in the crystal lattice as shown in the packing diagram in Figure 2.3.

The structure does not show any signs of axial coordination by the sulfur atoms of adjacent dithiocarbamate ligands as is noted in previously reported copper (II) dithiocarbamate structures[38], seemingly the steric bulk of the piperidine rings preclude the formation of these interactions. The lattice is stabilized by weak C–H···S interactions between the C6 methylene CH and S1 of an adjacent molecule. The C–H···S distance measures 2.935(2) Å, only fractionally shorter than the sum of the van der Waals radii suggesting a weak interaction.

Table 2.2: Crystal data and structure refinement details for complex (**1**).

Crystal Data	**[Ni(pip-dtc)$_2$ (1)**
Chemical formula	$C_{12}H_{20}N_2NiS_4$
Molar Mass (g mol^{-1})	379.23
Crystal system, space group	Monoclinic, $P2_1/c$
Temperature (K)	100(2)
a, b, c (Å)	6.0389(4), 8.4174(5), 15.1379(9)
β(°)	96.322(3)
V (Å^3)	764.81(8)
Z	2
Radiation type	Mo$K\alpha$
μ (mm^{-1})	1.80
Crystal size (mm)	0.21 × 0.04 × 0.02
Data collection	
Diffractometer	Bruker Apex Duo CCD diffractometer
Absorption correction	Multi-scan, *SADABS*, Bruker 2012
T_{min}, T_{max}	0.655, 0.746
No. of Measured, independent and observed [$I > 2\sigma(I)$] reflections	8601, 2220, 1952
R_{int}	0.024
Refinement	
$R[F^2 > 2\sigma(F^2)]$, $wR(F^2)$, S	0.023, 0.055, 1.09
No. of reflections	2220
No. of parameters	88
No. of restraints	0
H-atom treatment	H-atom parameters constrained.
$\Delta\rho_{max}$, $\Delta\rho_{min}$ (e Å^{-3})	0.54, –0.28

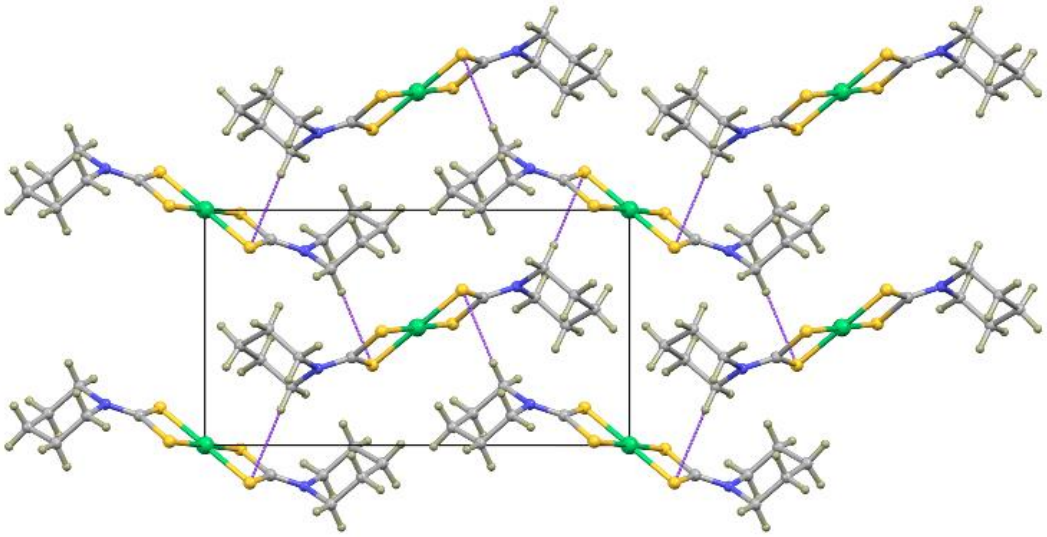

Figure 2.3: Packing diagram of complex (**1**) viewed down the *a*-axis. The packing diagram illustrates the trans-configuration of the piperidine rings and the resultant herringbone pattern. The lattice is stabilized by C-H···S interactions, shown as dashed purple tubes.

The X-ray data for the molecule [Ni(Etpz-dtc)$_2$] (**3**), crystallised in the triclinic crystal system with a half molecule in the asymmetric unit (i.e. $Z = 1$). The asymmetric unit comprises a single nickel(II) ion and bidentate S_2-donor dithiocarbamate ligand. The asymmetric unit and symmetry-complete molecule are shown in Figure 2.4. The metal ion has adopted an approximate square planar coordination geometry; relatively common for the d^8 electronic configuration. The four-membered chelate ring yields a strained intraligand S–Ni–S bond angle of 79.28(1)°, significantly more acute than the ideal angle of 90°. Consequently, the interligand S–Ni–S bond angle is more obtuse than is typically ideal, measuring 100.72(1)°. Parameters describing key bond lengths and angles are summarized in Table 2.3. A Mogul structural search [39] shows the bond lengths described in Table 2.3 to be comparable to those of related structures in the Cambridge Structural Database (CSD)[40]. A detailed Crystal data and structure refinement for the crystal is presented in Table 2.4. A search of the CSD shows that the ligand has been previously coordinated to nickel(II), however, the present structure has been determined to a significantly higher precision [39]. When coordinated to copper(II), which is the only other example of a *bis*-[Ni(Etpz-dtc)$_2$], a similar coordination geometry is noted [40].

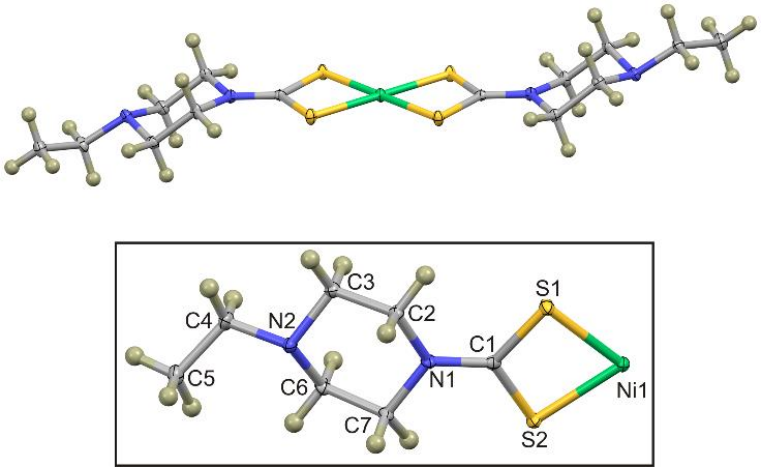

Figure 2.4: Thermal ellipsoid plot of the symmetry-completed structure of [Ni(Etpz-dtc)$_2$] (**3**), showing the nominally square planar coordination geometry. [Inset] Labelled structure of the asymmetric unit which comprises a half molecule, i.e. a single nickel(II) ion and ligand. Hydrogen atoms have been rendered as spheres of arbitrary radius, all other atoms are shown at the 50% probability level.

Table 2.3: Selected bond parameters describing the coordination sphere of [Ni(Etpz-dtc)$_2$].

Bond	Length (Å)	Bond	Angle (°)
Ni1–S1	2.2111(6)	S1–Ni1–S2 (intraligand)	79.28(1)
Ni1–S2	2.2103(6)	S1–Ni1–S2 (interligand)	100.72(1)
S1–C1	1.724(1)	S1–C1–S2	109.97(6)
S2–C1	1.720(1)	S1–C1–N1	125.14(9)
C1–N1	1.320(1)	S2–C1–N1	124.89(9)

Table 2.4: Crystal data and structure refinement details for complex (**3**) [Ni(Etpz-dtc)$_2$].

Crystal Data	**[Ni(Etpz-dtc)$_2$] (3)**
Chemical formula	$C_{14}H_{26}N_4NiS_4$
Molar mass (g mol^{-1})	437.32
Crystal system, space group	Triclinic, *P*-1
Temperature (K)	100(2)
a, *b*, *c* (Å)	6.5759(4), 8.4895(5), 8.8346(5)
α, β, γ (^{0})	84.185(2), 78.947(3), 80.038(3)
V (Å^3)	475.57(5)
Z	1
Radiation type	Mo Kα
μ (mm^{-1})	1.46
Crystal size (mm)	0.12 × 0.09 × 0.02
Data Collection	
Diffractometer	Bruker APEXII CCD diffractometer
Absorption correction	Multi-scan, SADABS
T_{min}, T_{max}	0.692, 0.746
No. of measured, independent and observed [$I > 2\sigma(I)$] reflections	8678, 2259, 2174
R_{int}	0.017
Refinement	
$R[F^2 > 2\sigma(F^2)]$, $wR(F^2)$, S	0.018, 0.047, 1.04
No. of reflections	2259
No. of parameters	107
H-atom treatment	H-atom parameters constrained
$\Delta\rho_{max}$, $\Delta\rho_{min}$ (e Å^{-3})	0.43, –0.18

The geometry of each of the two nitrogen atoms is significantly different with N1 adopting a trigonal planar geometry and N2 a trigonal pyramidal geometry. This difference highlights the partial double bond character of the C1–N1 bond, which measures 1.320(1) Å. This is shorter than a typical single bond, but fractionally longer than a standard double bond which measure *ca.* 1.47 and 1.28 Å, respectively. In contrast, the N2–C4 bond measures 1.474(1); typical of a carbon-nitrogen single bond. The four C–N bonds comprising the six-membered heterocycle have a mean bond length of 1.467(3) Å, again typical of a C–N single bond. The bond angles subtended by the nitrogen atoms similarly indicate their different geometries with the mean N–C bond angles of N1 measuring 119.7(2) and those of N2 was

measuring 110.0(2). Despite these differences in the geometry of the nitrogen atoms, the piperazine ring adopts a typical chair conformation.

The molecule packs with small voids in the lattice. The void sizes were calculated using a probe radius of 1.2 Å and grid spacing of 0.2 Å, this shows voids with a volume of 15.86 $Å^3$ (3.3% of the unit cell volume). The voids are isolated, i.e. not interconnected to form solvent-accessible channels, and their small volume renders them unlikely to be suitable for trapping solvent molecules. The lattice voids are shown in Figure 2.5. The molecule shows short, complementary C–H···Ni contacts with a C···Ni separation of 3.587(1) Å. This interaction is 0.139 Å shorter than the sum of the van der Waals radii of the interacting atoms, suggesting that it is a genuine stabilizing interaction. These interactions link the molecules into one-dimensional chains as shown in Figure 2.6. It shows the One-dimensional chain of [Ni(Etpz-dtc)$_2$], in the solid state (viewed down the *a*-axis) stabilised by C–H···Ni interactions between the methylene hydrogen atoms of the ethyl moiety and the Ni(II) ion of an adjacent molecule. The atoms have been rendered as spheres of arbitrary radius. The interactions are depicted as dashed purple lines.

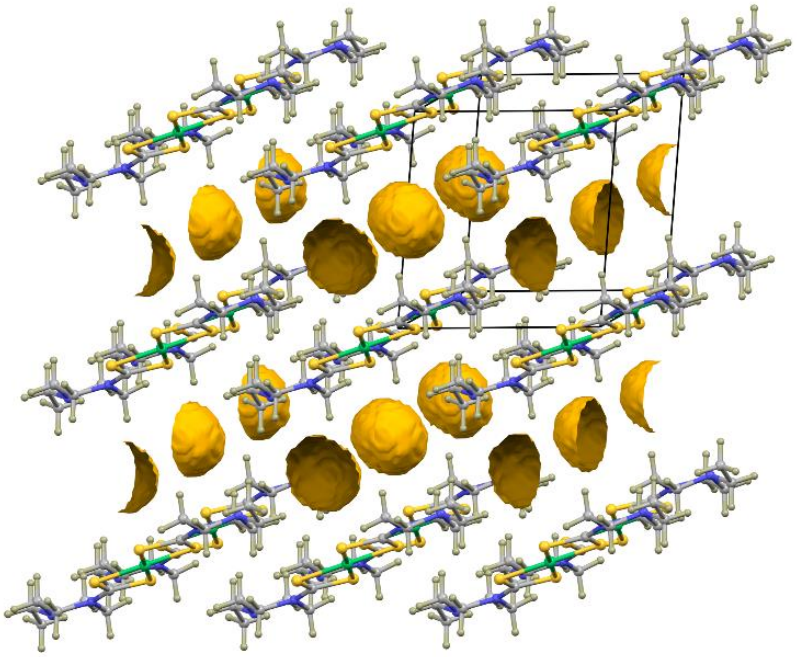

Figure 2.5: Voids in the lattice of [Ni(Etpz-dtc)$_2$], (shown as yellow surfaces). The voids were calculated using a probe radius of 1.2 Å. All atoms have been rendered as spheres of arbitrary radius.

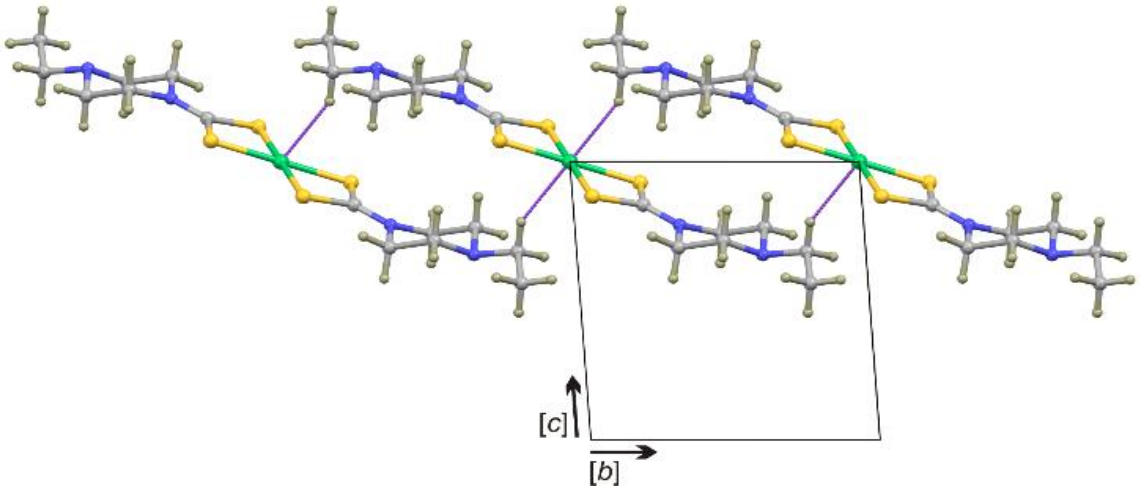

Figure 2.6: One-dimensional chain of [Ni(Etpz-dtc)$_2$] complex (**3**)

2.3.3. Nickel sulfide nanoparticles

The thermolysis of precursors in high boiling point primary amine solvents is a well reported route to high quality nanoparticles [33, 41]. The size of the nanoparticles depends on the reaction time, temperature, precursors and capping agent. Amines, particularly with long alkyl chains, are found to be suitable coordinating solvents for II–VI semiconductor nanomaterials. In this work, hexadecylamine (DDA), dodecylamine (HDA) and oleylamine (OLA) were selected as appropriate capping groups for synthesizing nickel sulfide nanoparticles. Complexes (**1**), (**2**) and (**3**) were thermolysed at temperatures of 190 °C and 230 °C for DDA (due to the boiling point limit), while 190 °C, 230 °C and 270 °C were chosen for HDA and OLA, for a duration of 2 hrs.

2.3.3.1 Powder X-ray diffraction

The powder X-ray diffraction (p-XRD) patterns of nanoparticles obtained from the single source precursors show the influence of varying reaction parameters (capping groups and temperatures) on the phases obtained. DDA, a shorter alkyl chain (12 carbon) capping group, gave phase-pure Ni_3S_4 (Card No. 00-043-1469) nanoparticles synthesized from complex (**1**), (**2**) and (**3**) at 190 and 230 °C (Figure 2.7-2.9). All diffraction peaks with *hkl* values (022), (113), (004), (115), (044) and (335) can be indexed to the sulfur-rich pure phase of cubic Ni_3S_4 (Card No. 00-043-1469). This is in good agreement with literature [4], where it is reported that temperatures lower than 250 °C predominantly affords the cubic phase Ni_3S_4. The results are

also in agreement with the decomposition pattern of other dithiocarbamate complexes reported elsewhere [33].

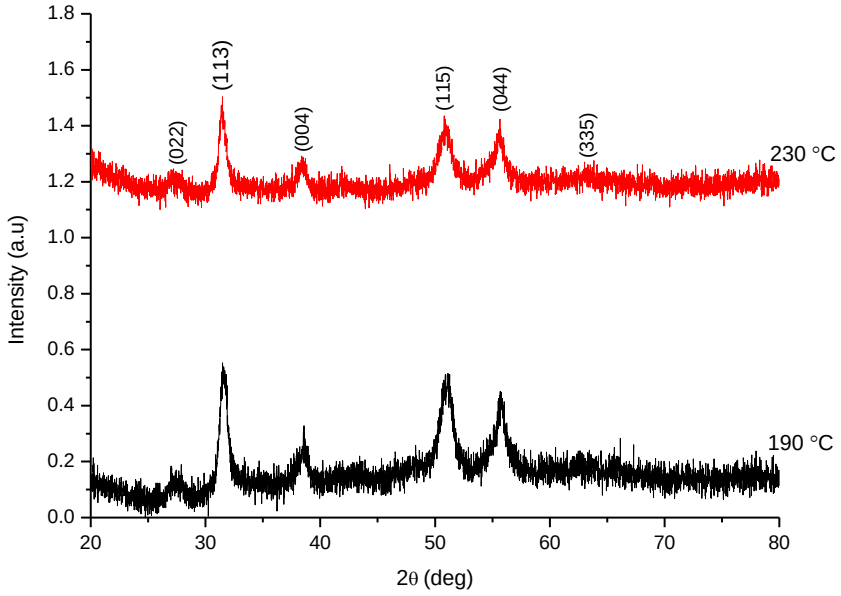

Figure 2.7: Powder X-ray diffraction (p-XRD) patterns for DDA-capped nickel sulfide nanoparticles from complex (**1**).

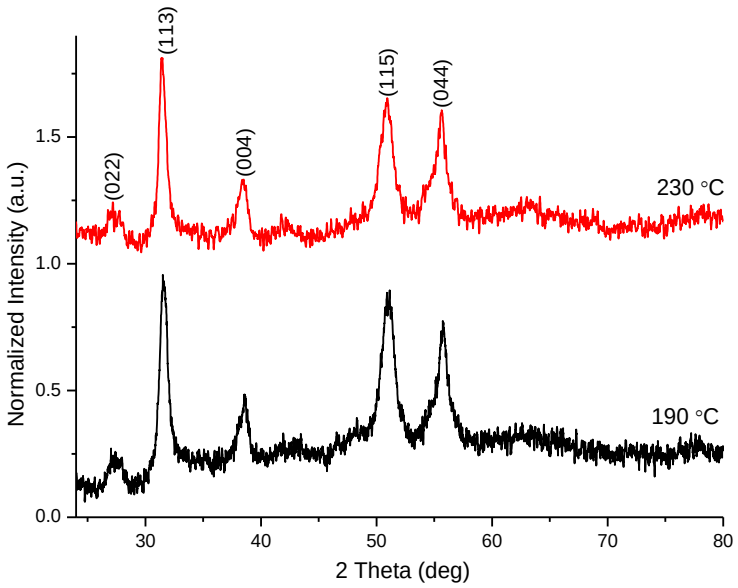

Figure 2.8: p-XRD patterns for DDA-capped nickel sulfide nanoparticles from complex (**2**).

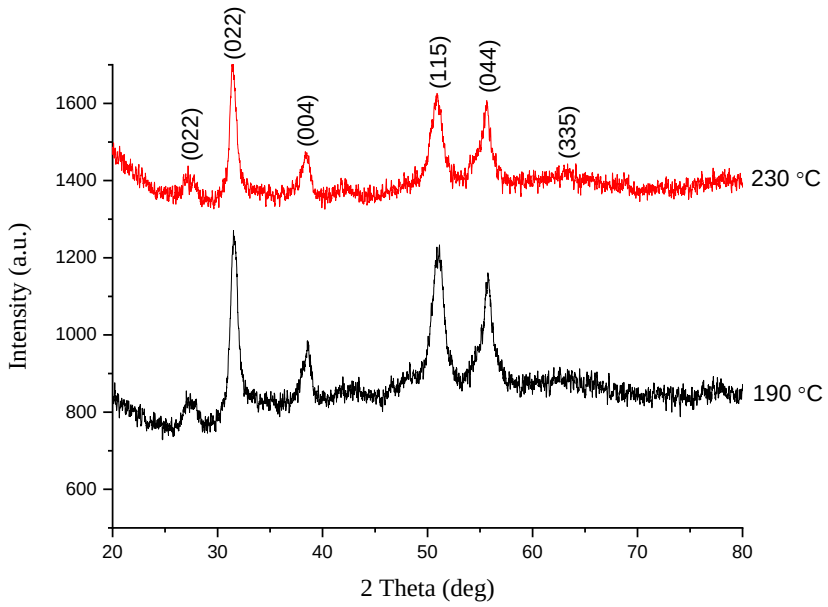

Figure 2.9: p-XRD patterns for DDA-capped nickel sulfide nanoparticles from complex (**3**).

A different phase, Ni_3S_2, was afforded when the thermolytic reaction was conducted in the primary amine with 16 carbon alkyl chain (HDA), at all reaction temperatures (Figures 2.10-2.12). The p-XRD peaks were indexed to the (101), (012), (003), (202), (211), (122), (303), (214) and (401) mirror planes of rhombohedral α-Ni_3S_2 (card no.00-002-0772). The diffraction patterns show an increase in crystallinity as the temperature is raised from 190 ºC to 270 ºC. Crystallite sizes, as estimated by the Debye-Scherrer equation, show averages of 3.1 nm, 7.1 nm and 11.9 nm for nanoparticles prepared at 190 ºC, 230 ºC and 270 ºC, respectively. The crystallite sizes were corroborated by the particle sizes measured from the TEM images provided in Figure 2.17.

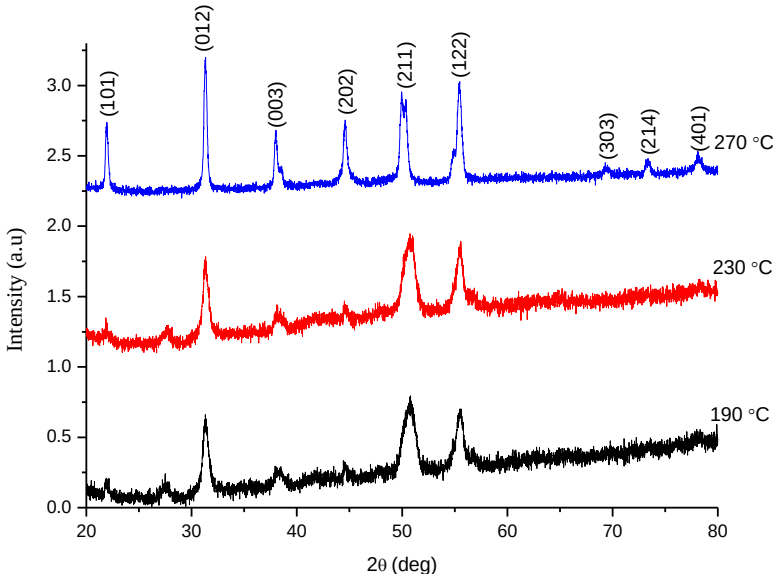

Figure 2.10: p-XRD patterns for HDA-capped nickel sulfide nanoparticles from complex (**1**).

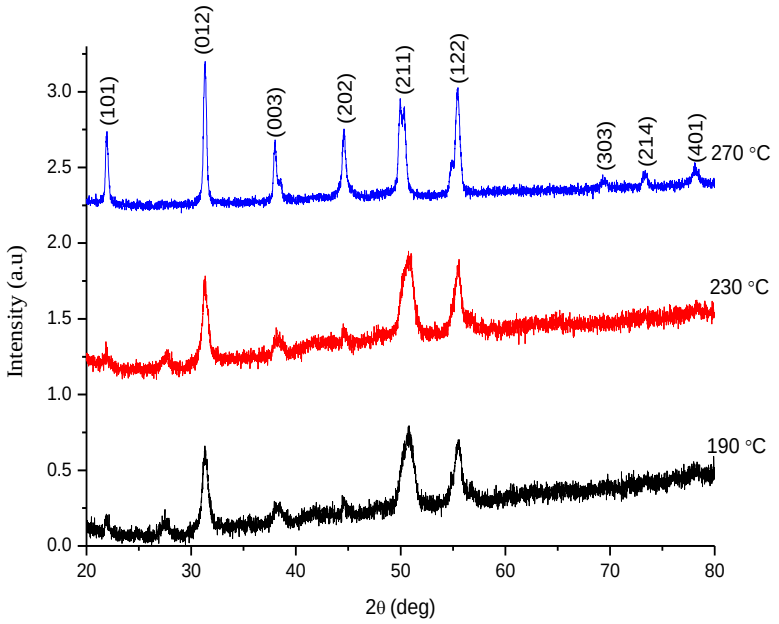

Figure 2.11: p-XRD patterns for HDA-capped nickel sulfide nanoparticles from complex (**2**).

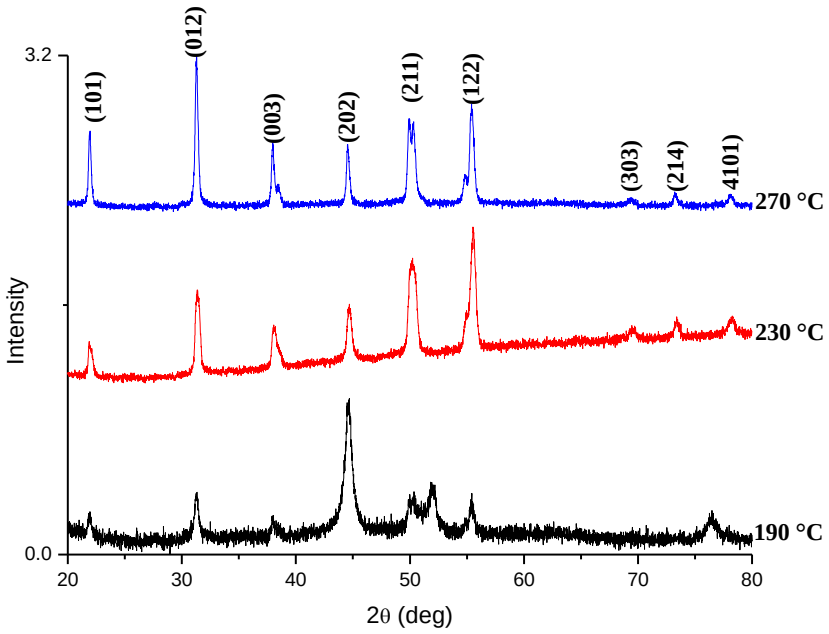

Figure 2.12: p-XRD patterns for HDA-capped nickel sulfide nanoparticles from complex (**3**).

When OLA (18 carbon alkyl chain) was used as a capping agent, both complex (**1**) and (**2**) gave mixed phase nanoparticles (Figures 2.13 and 2.14). However complex (**3**) gave a pure phase of Ni_3S_2 (Figure 2.15). The diffraction peaks for complex (**1**) and (**2**) show a predominant phase of hexagonal α-NiS at 270 °C (card number 03-065-3419) which is indexed to (100), (101), (102), and (110) planes. Unindexed peaks denoted with * for 270 °C could also be matched to a rhombohedral β-NiS (card number; 00-012-0041). At lower temperatures, 190 °C and 230 °C, unindexed peaks denoted with # were identified as cubic polydymite (Ni_3S_4) (card number: 00-047-1739) which agrees with literature reports on the formation of the phase at lower temperatures [33]. Phase transition in the nickel sulfide system as a result of an increase in temperature has been reported previously [30]. The results of the parameters and properties of the nickel sulfide nanoparticles synthesized from this work are presented in Table 2.5.

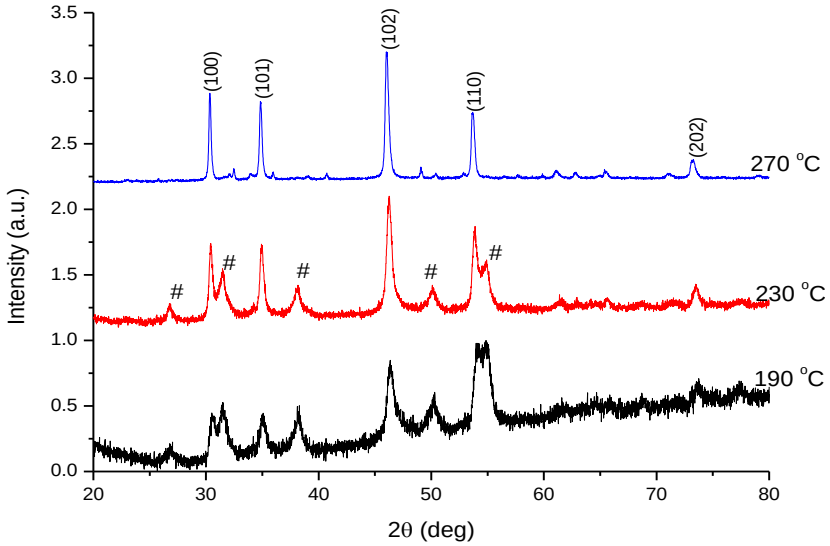

Figure 2.13: p-XRD patterns of OLA-capped α-NiS (card number 03-065-3419) nanoparticles synthesized using complex (**1**). # denotes a cubic polydymite (Ni_3S_4) phase (card number: 00-047-1739)

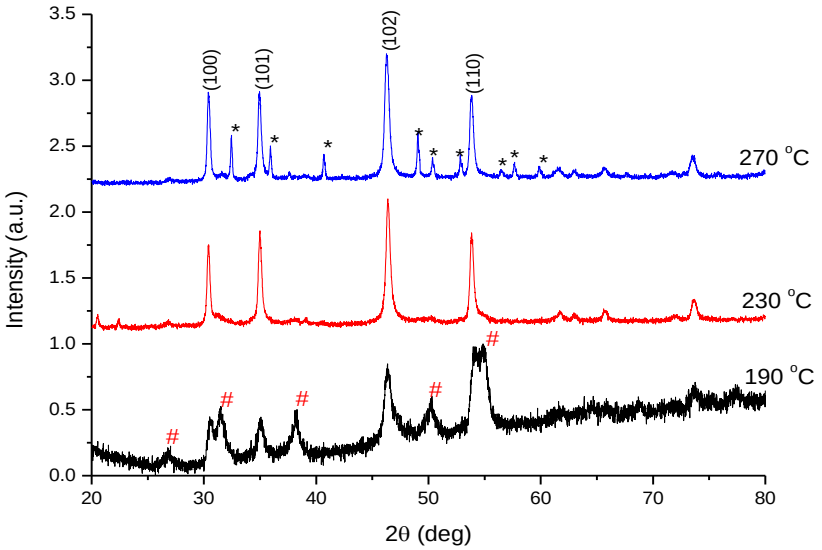

Figure 2.14: p-XRD patterns of OLA-capped α-NiS (card number 03-065-3419) nanoparticles synthesized using complex (**2**). * denotes a rhombohedral β-NiS phase (card number 00-012-0041), while # denotes a cubic polydymite (Ni_3S_4) phase (card number 00-047-1739).

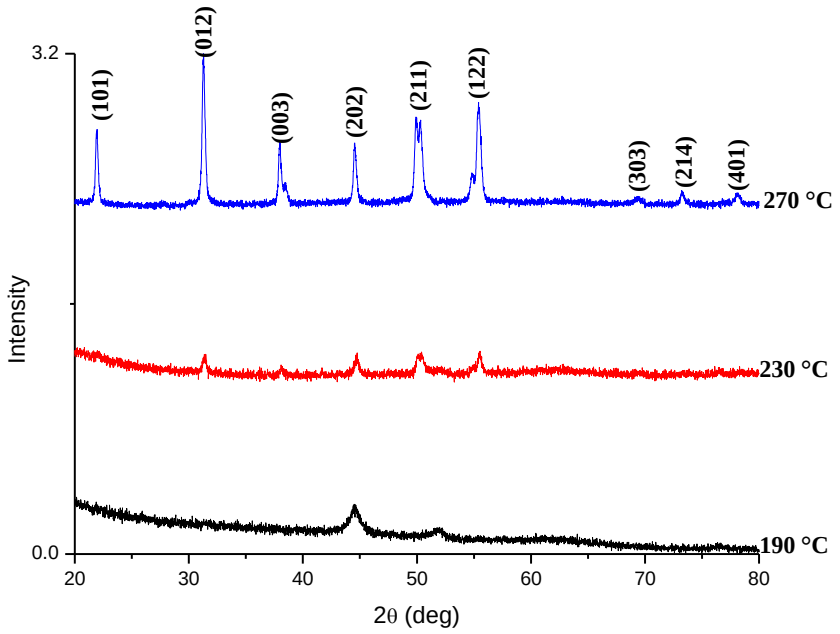

Figure 2.15: p-XRD patterns of OLA-capped nickel sulfide nanoparticles using complex (**3**).

2.3.3.2 TEM and High Resolution TEM Analyses

Figure 2.16 shows TEM images for DDA-capped nickel sulfide nanoparticles from all three complexes at various temperatures. The morphology and average particle sizes of the as-synthesized nickel sulfide nanoparticles varied with temperature and chemical nature of the precursor. Nanoplates are observed at a lower reaction temperature of 190 °C when complex (**1**) was used (Figure 2.16 a). These nanoplates with an unusual cross-like shape have been reported previously by Wu *et al.* [42]. The nanoplates in our case have four seemingly equal wings, with each lateral wing having average lengths of approximately 65.47 ± 1.24 nm. At 230 °C, irregular-shaped nanoparticles are observed (Figure 2.16 b). Complex (**2**) gave spherical nanoparticles with a relatively smaller average size of 8.23 ± 0.63 nm at 190 °C (Figure 2.16 c) while at 230 °C, short rods with average width of 6.06 ± 0.35 nm were observed (Figure 2.16 d). Figure 2.17 shows representative particle size distribution for the nickel sulfide nanoparticles; other nanoparticles are not represented, due to limitations associated with very small particle sizes which could not be measured accurately. The histograms display a Gaussian curve pattern, which is the norm for nanoparticles grown in similar experimental procedures. Narrow Gaussian curve suggests small particle size distribution, thus, monodispersed nanoparticles.

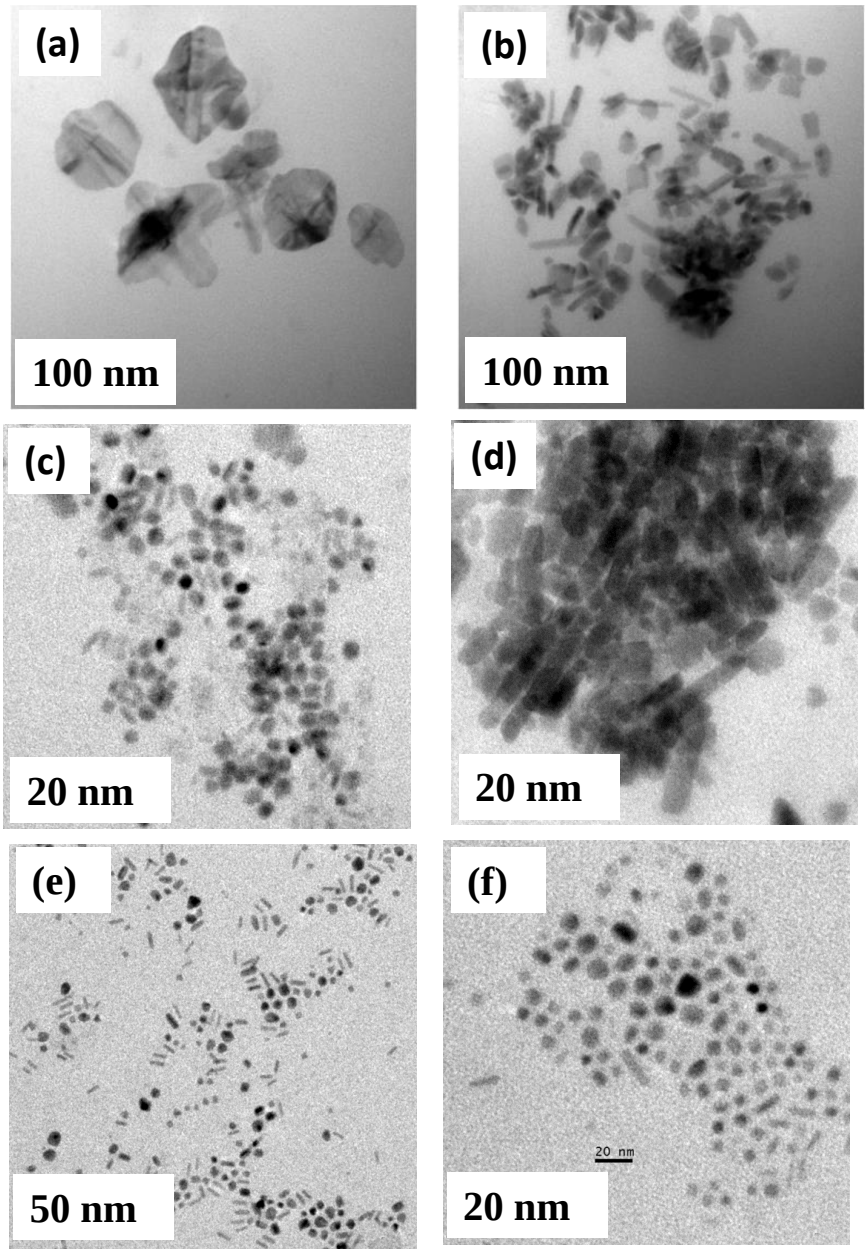

Figure 2.16: TEM images for DDA-capped nickel sulfide nanoparticles from complex (**1**) synthesized at (a) 190 °C (b) 230 °C; complex (**2**) at (c) 190 °C and (d) 230 °C and complex (**3**) at (e) 190 °C and (f) 230 °C.

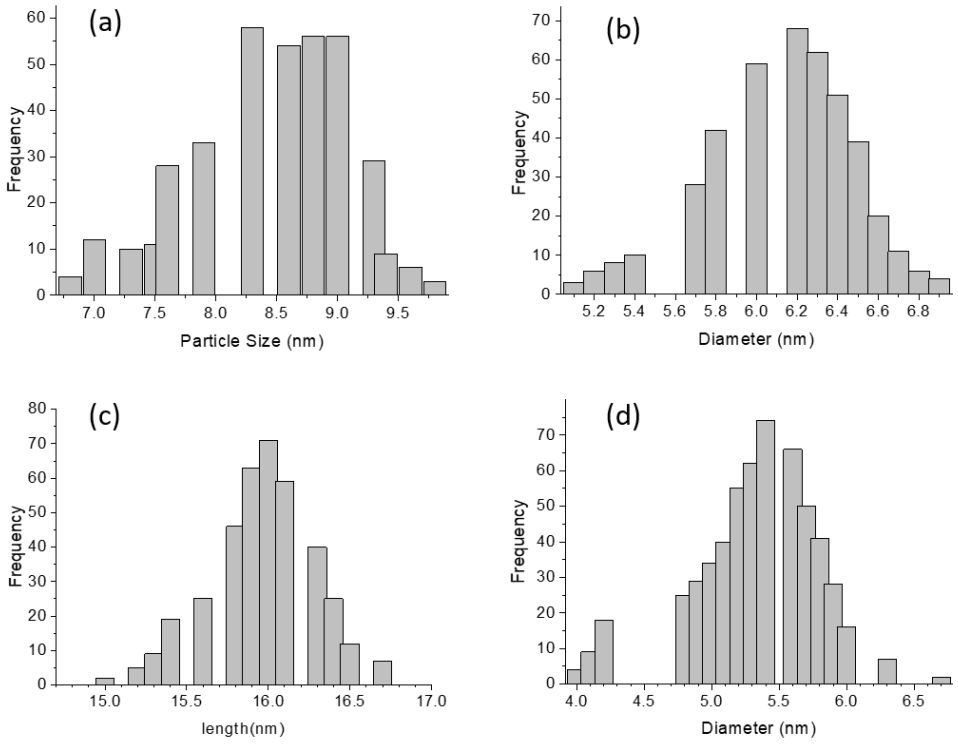

Figure 2.17: Particle size distribution for DDA-capped nickel sulfide nanoparticles synthesized from (a) complex (**2**) at 190 °C, (b) complex (**2**) at 230 °C, (c) complex (**3**) at 190 °C and (d) complex (**3**) at 230 °C.

TEM images for HDA-capped nickel sulfide nanoparticles from all three complexes are represented in Figure 2.18. Complex (**2**) gave slightly larger nanoparticles as compared to complex (**1**). The nickel sulfide nanoparticles synthesized from complex (**1**) were spherical in shape with an average diameter of 5.71 ± 0.12 nm, 9.95 ± 0.14 nm and 12.1 ± 0.57 nm at reaction temperatures of 190 °C, 230 °C and 270 °C, respectively. For complex (**2)**, the estimated particle size for the spherical nanoparticles was 2.85 ± 0.08 nm (190 °C), 7.28 ± 0.12 nm (230 °C), whereas irregular-shaped particles were formed at 270 °C their average particle size has been shown to be 11.53 ± 0.12 nm. Nanoparticles from complex (**3**) exhibited refined morphologies compared to complexes (**1**) and (**2**). At 190 °C, nanoparticles are predominantly short rods with spheres displaying average diameter of 4.69 ± 0.11 nm. At 230 °C, the average particle size of the nanoparticles increases to 7.32 ±0.12 nm and the morphology becomes more irregular. The representative particle size distribution shown in Figure 2.19 exhibit similar trend observed in DDA-capped nanoparticles in Figure 2.17.

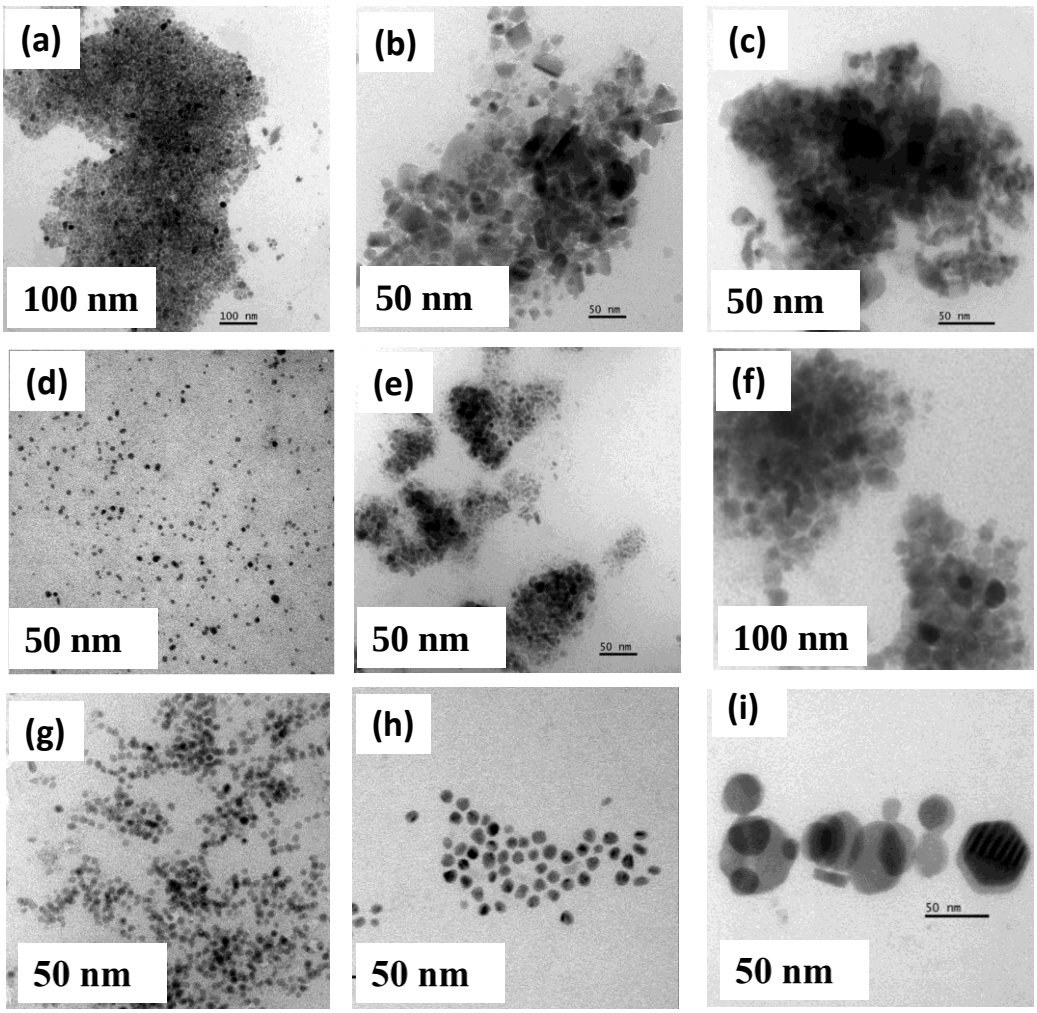

Figure 2.18: TEM images for HDA-capped nickel sulfide nanoparticles synthesized at (a) 190 °C, (b) 230 °C and (c) 270 °C from complex (**1**); (d) 190 °C, (e) 230 °C and (f) 270 °C from complex (**2**) and (g) 190 °C, (h) 230 °C and (i) 270 °C from complex (**3**).

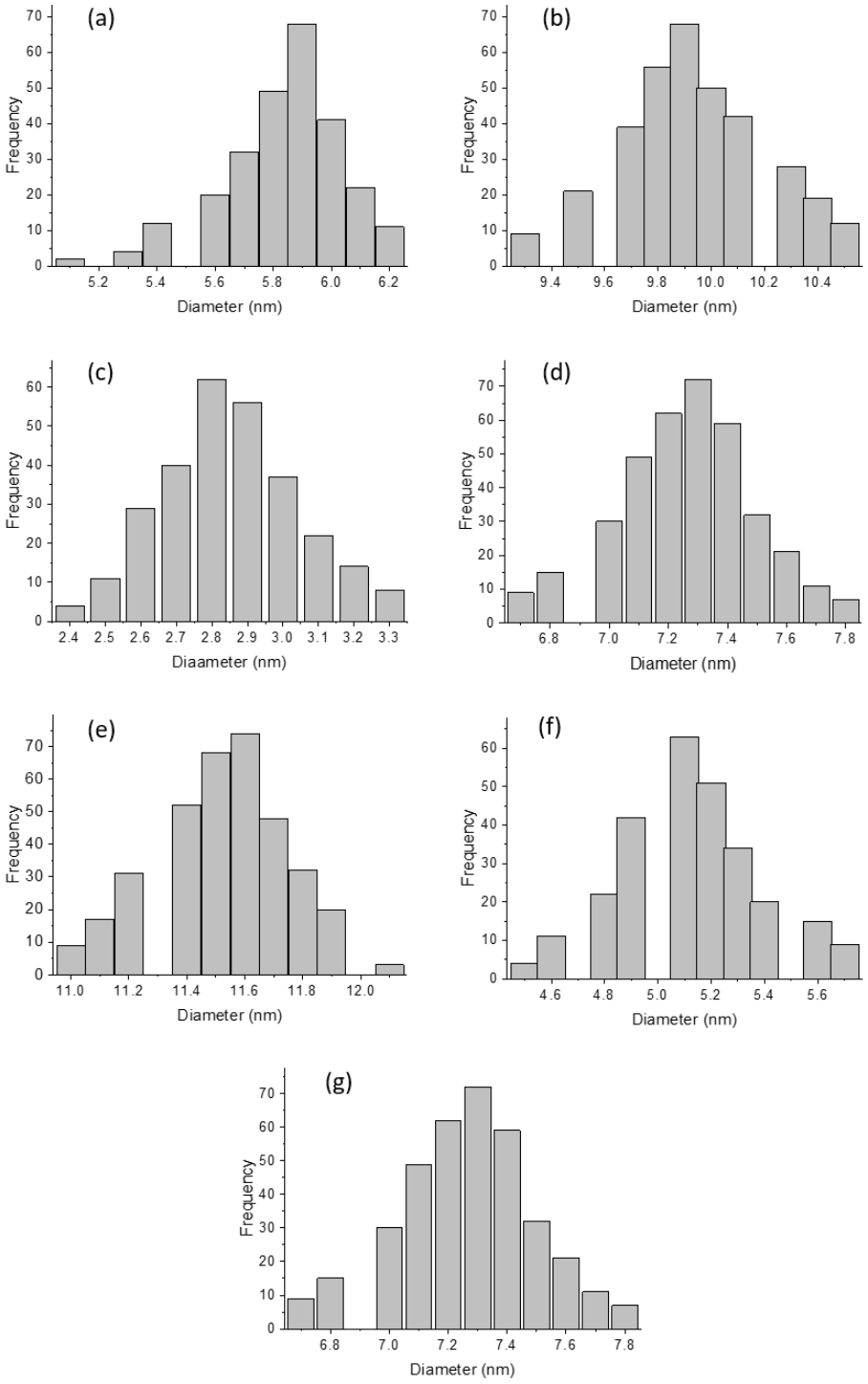

Figure 2.19: Particle size distribution for HDA-capped nickel sulfide nanoparticles synthesized from (a) complex (**1**) at 190 °C, (b) complex (**1**) at 230 °C, (c) complex (**2**) at 190 °C, (d) complex (**2**) at 230 °C, (e) complex (**2**) at 270 °C, (f) complex (**3**) at 190 °C and (g) complex (**3**) at 230 °C.

TEM images (Figure 2.20) for OLA-capped nickel sulfide nanoparticles synthesized from all complexes show the formation of close to spherical nanoparticles and irregular shaped nanoparticles, depending on the reaction parameters. The particle sizes increase with an increase in reaction temperature, as well as the nature of the complex (Figure 2.21). Complex (**3**) has better morphology as compared to complexes (**1**) and (**2**) which is attributed to their decomposition pattern. Complex (**1**) has higher thermal stability than complexes (**2**) and (**3**), hence, quicker nucleation pattern for nanoparticles and so more monodispersed nanoparticles and better morphology

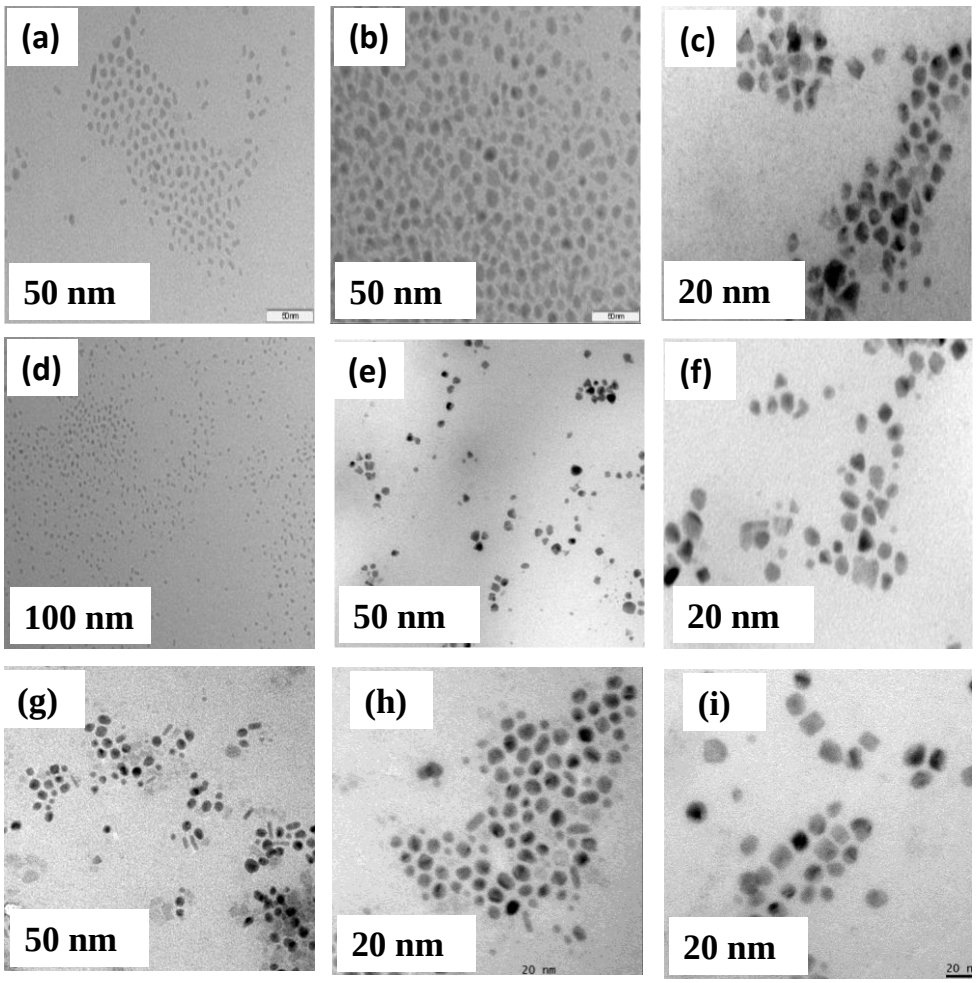

Figure 2.20: TEM images for OLA-capped nickel sulfide nanoparticles synthesized from complex (**1**) at (a) 190 °C, (b) 230 °C and (c) 270 °C; complex (**2**) at (d) 190 °C, (e) 230 °C, (f) 270 °C and complex (**3**) (g) 190 °C (h) 230 °C and (i) 270 °C.

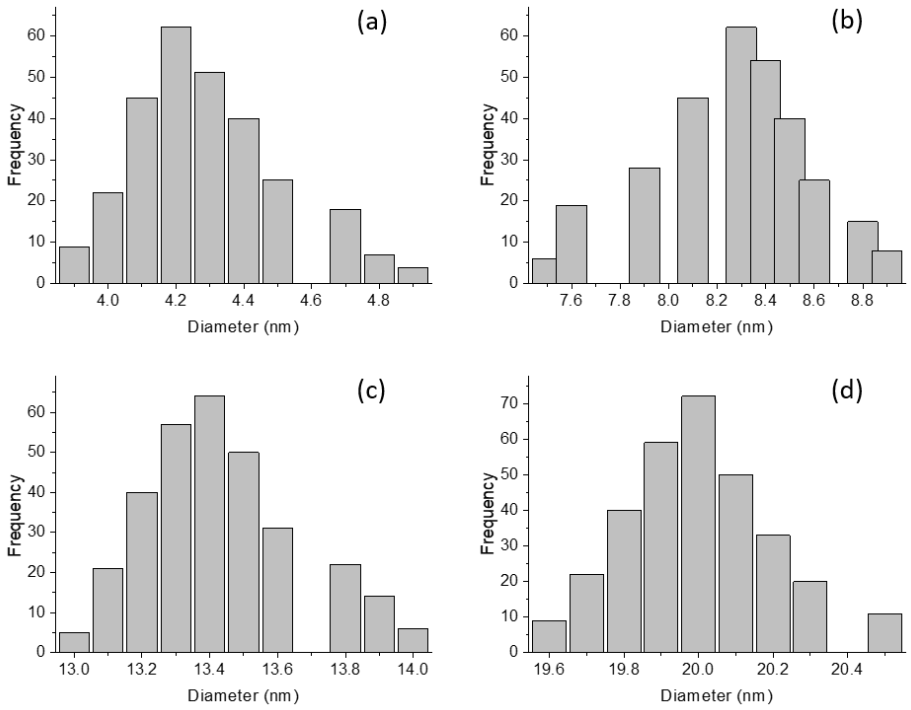

Figure 2.21: Particle size distribution for OLA-capped nickel sulfide nanoparticles synthesized from (a) complex (**1**) at 190 °C, (b) complex (**2**) at 230 °C, (c) complex (**3**) at 230 °C and (d) complex (**3**) at 270 °C.

A summary of particle size, morphology and phase observed from nanoparticles is provided in Table 2.5. The HRTEM images for selected samples is represented in Figures 2.22 a, c and d. The HRTEM image for HDA-capped nanoparticles from complex (**2**) show lattice fringes with a d-spacing of 2.85 Å (Figure 2.22 a); the corresponding SAED image corroborated to the α-Ni_3S_2 phase (Figure 2.22 b). HRTEM images for DDA-capped nanoparticles from complex (**2**) and OLA-capped NiS from complex (**1**) show lattice fringes of 2.87 Å (Figure 2.22 c) and 2.86 Å (Figure 2.22 d), respectively. All HRTEM images and the SAED image depict materials of high crystallinity.

Table 2.5: Summary of the reaction conditions, particle sizes and shapes of the obtained nickel sulfide nanoparticles.

Complex	Capping group	Temp (°C)	Morphology	Particle size/aspect ratio (nm)	Phase
(**1**)	DDA	190	Nanoplates	65.47 ± 1.24	Ni_3S_4
		230	Irregular shaped rods	7.67 ± 0.42	Ni_3S_4
	HDA	190	Spherical	5.71 ± 0.12	Ni_3S_2
		230	Spherical	9.95 ± 0.14	Ni_3S_2
		270	Irregular shape	-	Ni_3S_2
	OLA	190	Close to sphere	4.38 ± 0.11	Mixed
		230	Irregular tetrahedral shape	-	Mixed
		270	Irregular shape	-	Hex. NiS
(**2**)	DDA	190	Spherical	8.23 ± 0.63	Ni_3S_4
		230	Short rods (length)	6.06 ± 0.35	Ni_3S_4
	HDA	190	Spherical	2.85 ± 0.08	Ni_3S_2
		230	Spherical	7.28 ± 0.12	Ni_3S_2
		270	Spherical	11.53 ± 0.12	Ni_3S_2
	OLA	190	Spherical and rods	-	Mixed
		230	Irregular sphere	8.26 ± 0.21	Mixed
		270	Irregularly shaped	-	Hex. NiS
(**3**)	DDA	190	Shot rods (length)	15.86 ± 0.25	Ni_3S_4
		230	Irregular spheres	5.29 ± 0.54	Ni_3S_4
	HDA	190	Nanospheres	4.69 ± 0.11	Ni_3S_2
		230	Nanospheres	7.32 ± 0.12	Ni_3S_2
		270	Nanospheres	22.7	Ni_3S_2
	OLA	190	Rods and spheres	-	Ni_3S_2
		230	Irregular spheres	13.48 ± 0.12	Ni_3S_2
		270	Irregular spheres	20.01 ± 0.08	Ni_3S_2

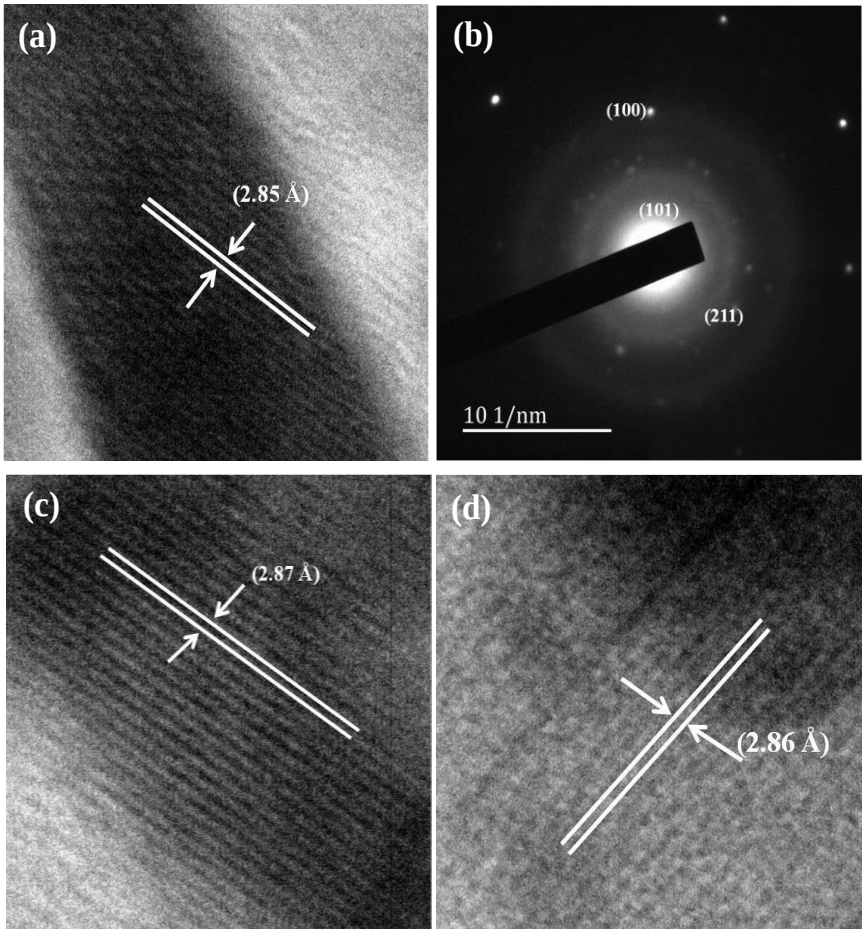

Figure 2.22: HRTEM images for; (a) HDA-capped nickel sulfide nanoparticles from complex (**2**) at 270 ºC and (b) corresponding SAED; (c) HRTEM image for DDA-capped nickel sulfide nanoparticles from complex (**2**) at 230 ºC and (d) OLA-capped nickel sulfide nanoparticles from complex (**1**) at 270 ºC.

2.3.3.3 Magnetic properties

The magnetic properties of the representative samples annealed at 230 °C were recorded at 17 °C by a vibrating sample magnetometer. The hysteresis loops are presented in Figure 2.23. The sample (DDA PIPDTC) prepared in DDA using complex (**1**) presents the magnetization of cubic-Ni_3S_4 nanoparticles at 2000 Oe of about 1.6 emu/g and a coercive field of 224 Oe. Similarly, the sample (DDA THQDTC) prepared in DDA using complex (**2**) showed cubic-Ni_3S_4 nanoparticles exhibiting magnetization of about 3.2 emu/g and a coercive field of 93 Oe, with a

saturation magnetization that is higher than that from complex (**1**) prepared under similar conditions. The coercive field of the sample prepared using complex (**1**) is higher than that from complex (**2**) both in DDA. Both samples prepared in DDA showed ferromagnetic behaviour, typical of Ni_3S_4 phase [24]. It can be seen that the rhombohedral (α-Ni_3S_2) sample (HDA THQDTC) prepared from complex (**2**) using HDA shows an almost linear plot of magnetization against applied field with almost zero coercive field which corresponds to a paramagnetic phase. The magnetic properties of nanomaterials are believed to be highly dependent on the structure and particle sizes. The coercive fields tend to correlate well with particle sizes. From Figure 2.23, the DDA Ni_3S_4 nanoparticles with higher coercive field has relatively larger particle size. These results appear consistent with transformation from single to multi-domain structure with increase in particle size [43]. The coercive fields H_C and particle sizes D are expected to vary as $H_C = a_1 - b_1/D^2$ and $H_C = a_2 + b_2/D$ for single domain and for multi-domain regions respectively where a_i and b_i are constants.

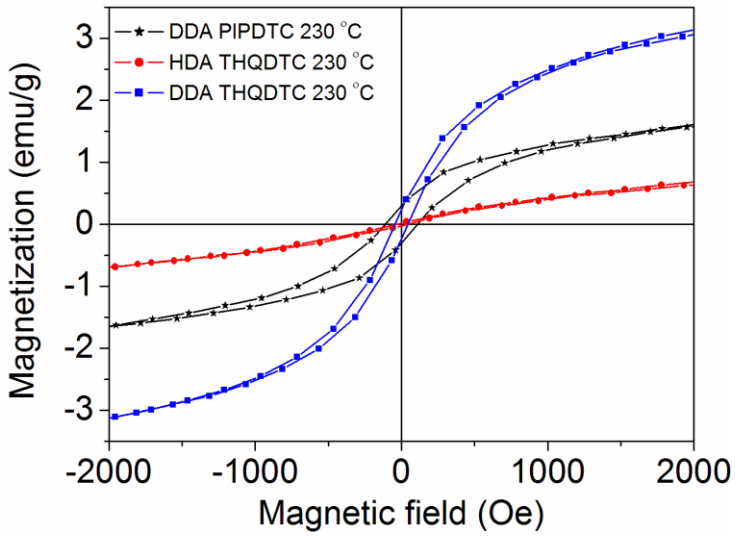

Figure 2.23: Magnetic hysteresis curves of the nickel sulfide samples synthesized by the hot injection thermal decomposition of complexes at 230 °C. The hysteresis loops were recorded at 17 °C.

2.3.3.4. Optical Properties

Absorption (UV-Vis) spectra with their corresponding tauc plots for nickel sulfide nanoparticles synthesized at various reaction conditions using complexes (**1-3**) are presented in Figures 2.24 – 2.32. The optical properties of nanoparticles obtained were evaluated. The band gap energies of the nanoparticles were estimated using Tauc plots [44]. The calculated absorption band gap energies range from 3.1 – 3.8 eV while the Tauc-estimated band gap energies ranges from 2.8 - 3.4 eV. Calculation of the band gap was done by using the maximum absorption peak on the UV-Vis micrograph. The Tauc estimated and the calculated band gaps are similar within the limits of experimental error for the estimation of absorption maxima for UV-Vis spectra. All absorption spectra show an obvious blue shift if compared to bulk nickel sulfide which absorbs at around 590 nm (2.1 eV) [21]. Calculated band gaps from absorption maxima and estimated band gap from Tauc plots for complex (**3**) is presented in Table 2.6. This was chosen as a representative of other complexes because it gave pure phase in all three capping groups. Generally, all UV-Vis spectra obtained from this work corroborate the lirature on the Ni-S systems. However, it is noteworthy that multiple absorbtion bands were occasionally observed and they may be attributed to defects and phase impurity levels in the as-synthesized nanoparticles.

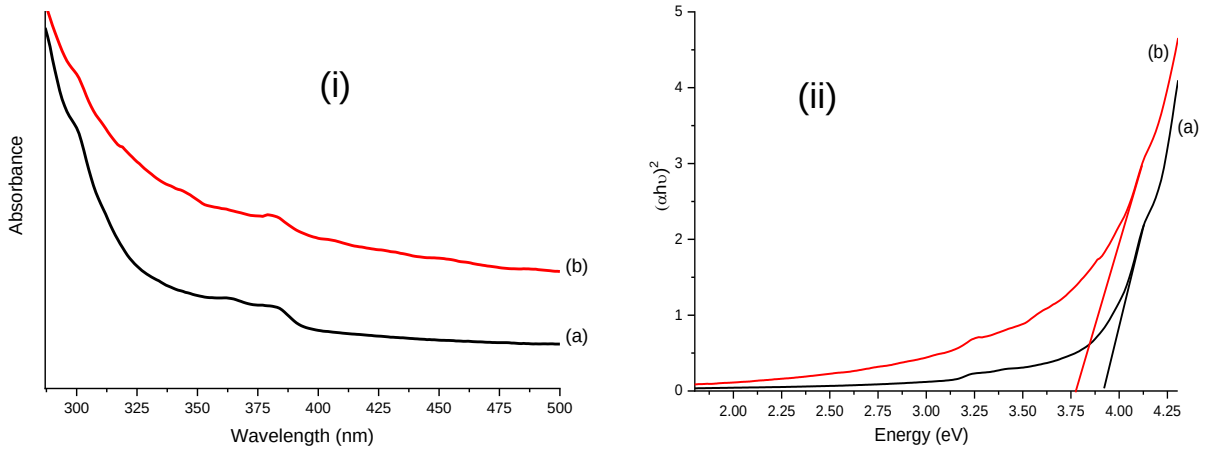

Figure 2.24: The (i) UV-Vis spectra and (ii) corresponding Tauc plots for DDA-capped nickel sulfide nanoparticles synthesized from complex (**1**) at (a) 190 °C and (b) 230 °C.

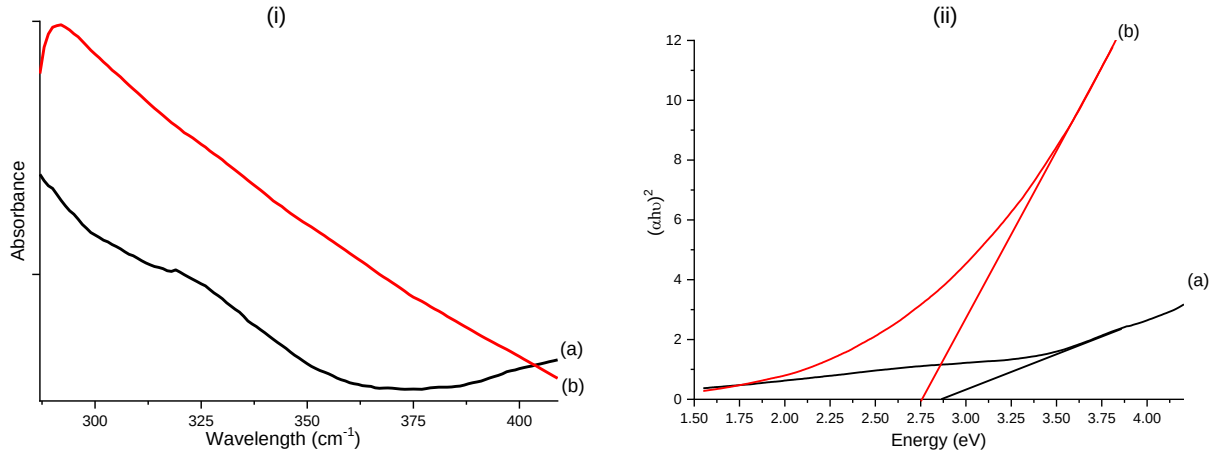

Figure 2.25: The (i) UV-Vis spectra and (ii) corresponding Tauc plots for DDA-capped nickel sulfide nanoparticles synthesized from complex (**2**) at (a) 190 °C and (b) 230 °C.

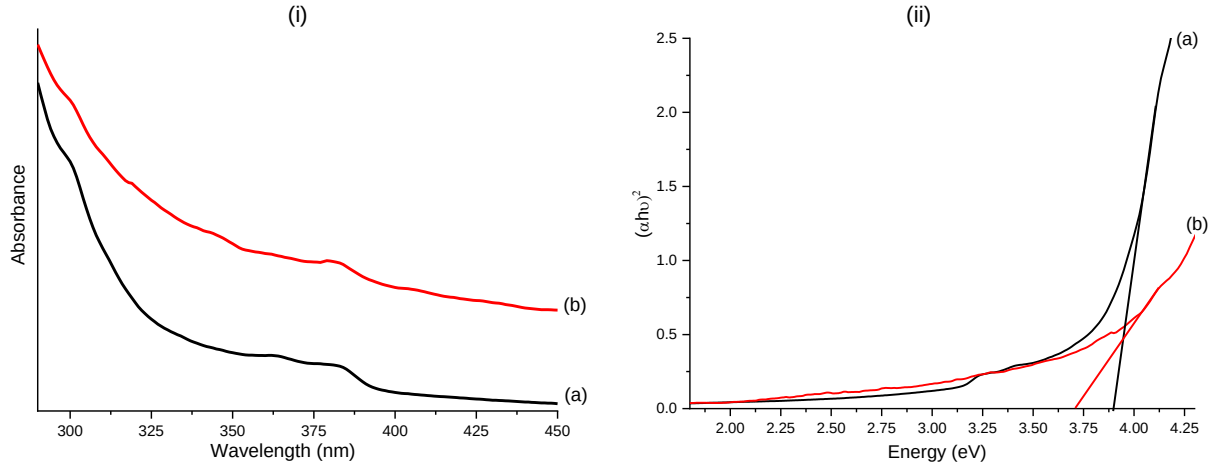

Figure 2.26: The (i) UV-Vis spectra and (ii) corresponding Tauc plots for DDA-capped nickel sulfide nanoparticles synthesized from complex (**3**) at (a) 190 °C and (b) 230 °C.

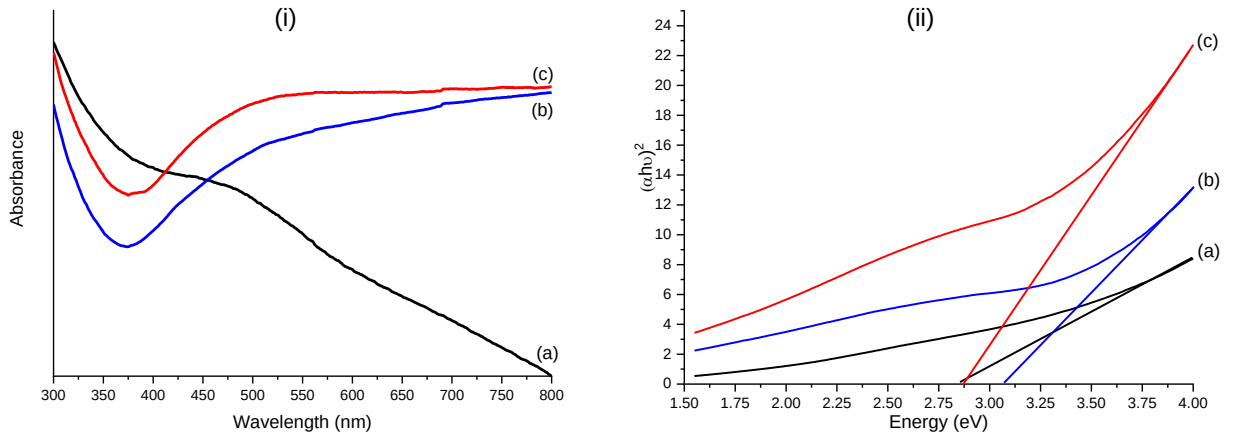

Figure 2.27: The (i) UV-Vis spectra and (ii) corresponding Tauc plots for HDA-capped nickel sulfide nanoparticles synthesized from complex (**1**) at (a) 190 °C, (b) 230 °C and 270 °C.

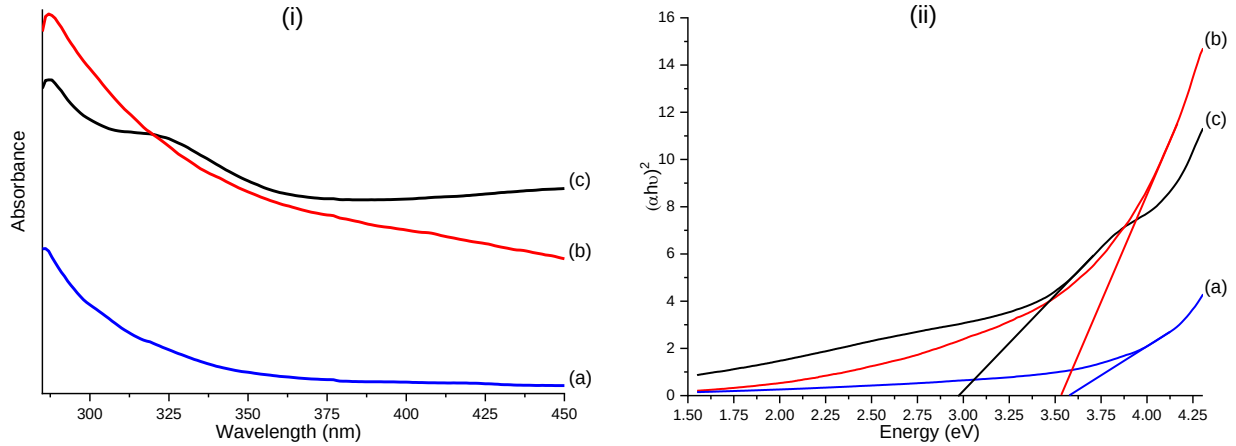

Figure 2.28: The (i) UV-Vis spectra and (ii) corresponding Tauc plots for HDA-capped nickel sulfide nanoparticles synthesized from complex (**2**) at (a) 190 °C, (b) 230 °C and 270 °C.

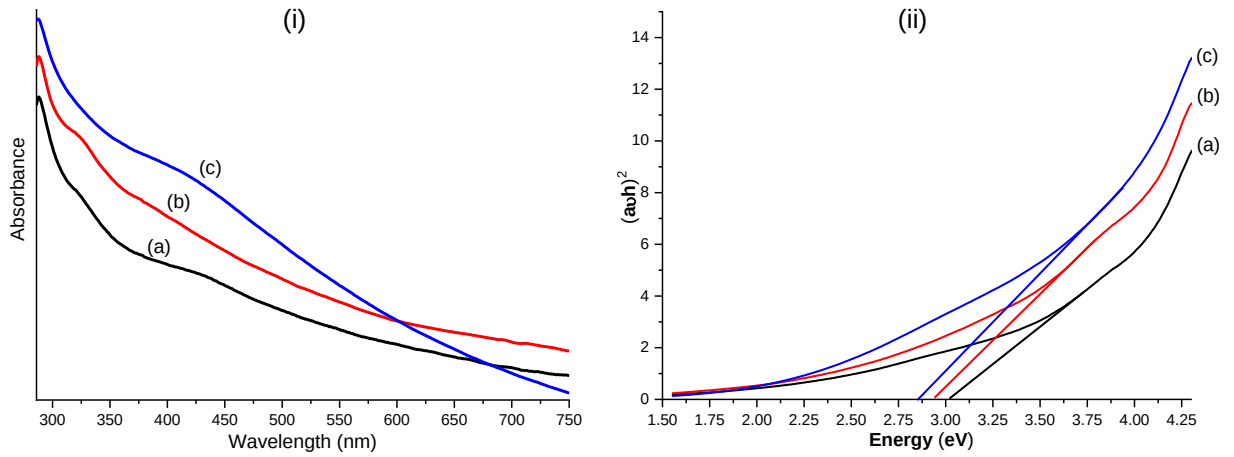

Figure 2.29: The (i) UV-Vis spectra and (ii) corresponding Tauc plots for HDA-capped nickel sulfide nanoparticles synthesized from complex (**3**) at (a) 190 °C, (b) 230 °C and 270 °C.

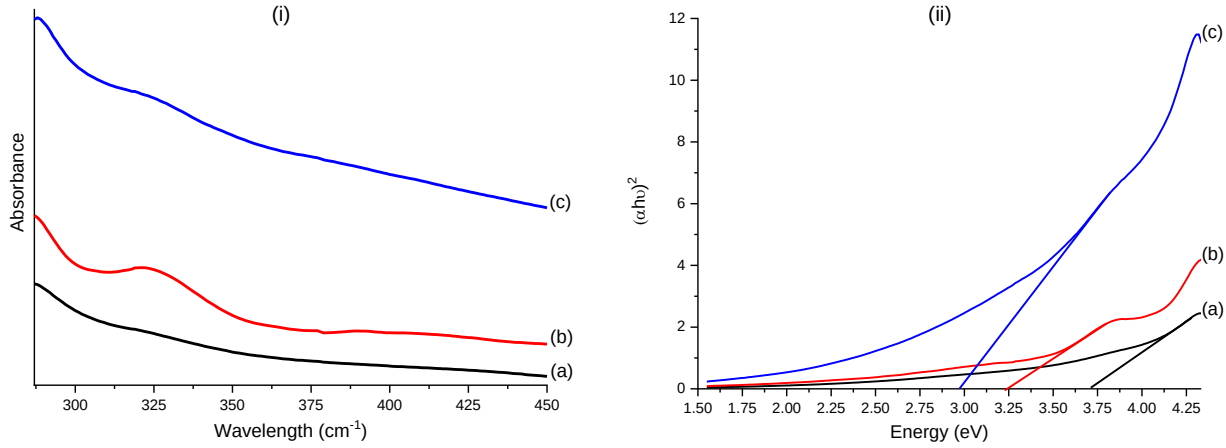

Figure 2.30: The (i) UV-Vis spectra and (ii) corresponding Tauc plots for OLA-capped nickel sulfide nanoparticles synthesized from complex (**1**) at (a) 190 °C, (b) 230 °C and 270 °C.

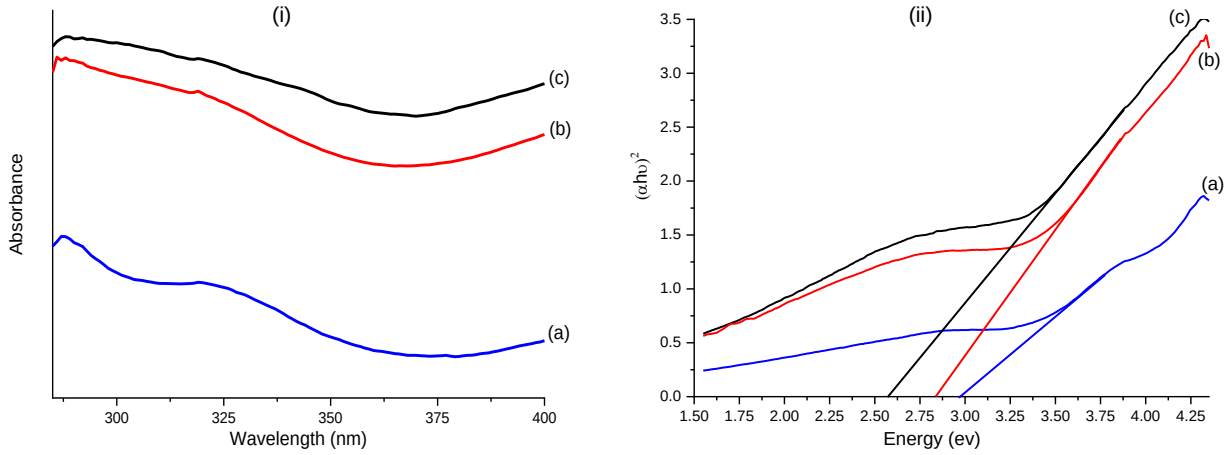

Figure 2.31: The (i) UV-Vis spectra and (ii) corresponding Tauc plots for OLA-capped nickel sulfide nanoparticles synthesized from complex (**2**) at (a) 190 °C, (b) 230 °C and 270 °C.

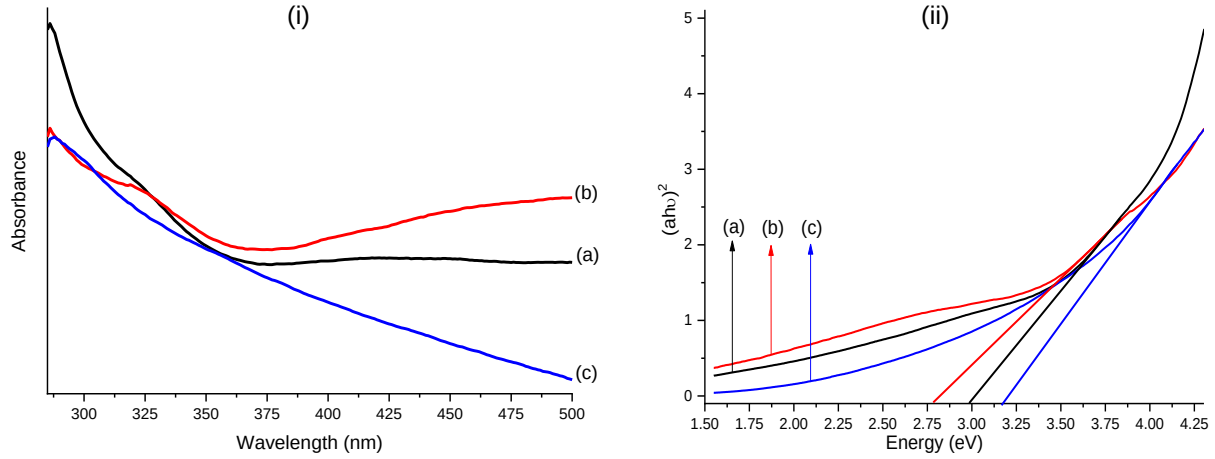

Figure 2.32: The (i) UV-Vis spectra and (ii) corresponding Tauc plots for OLA-capped nickel sulfide nanoparticles synthesized from complex (**3**) at (a) 190 °C, (b) 230 °C and 270 °C.

Table 2.6: Calculated band gap from the UV-Vis maximum absorption and estimated band gap by Tauc plots of nickel sulfide nanoparticles obtained from complex (**3**).

Capping group	Temp (°C)	Absorption maxima (nm)	Calculated eV	Tauc eV
DDA	190	382	3.24	3.2
	230	394	3.16	3.6
HDA	190	324	3.83	3.1
	230	328	3.78	2.9
	270	399	3.11	2.8
OLA	190	322	3.85	3.4
	230	329	3.77	3.2
	270	Broad absorption	-	2.9

2.4. Conclusion

Piperidine (**1**) tetrahydroquinoline (**2**) and ethyl piperazine (**3**) nickel(II) dithiocarbamate complexes have been synthesized and characterized. Improved low-temperature single X-ray crystal structures of complex (**1**) and complex (**3**) have also been elucidated. These complexes have been used as single source precursors to synthesize high quality nickel sulfide nanoparticles via a hot injection approach using dodecylamine, hexadecylamine and oleylamine as the coordinating solvents. Nickel sulfides of different mineral phases, namely: Ni_3S_4 and Ni_3S_2, have been produced. The rare pure phases produced are in agreement with previous reports, where the formation of phase-pure Ni-S systems is temperature dependent. In addition, the formation of mixed phases when oleylamine is used and the formation of Ni_3S_4 for dodecylamine (at all temperatures) suggest further studies in the field. Nanoparticles can display a variety of magnetic properties near room temperature which are dependent on the crystalline phases. The coercive field data can therefore be investigated on the basis of transformation from single to multi-domain structure. This study provides a relatively

reliable single source precursor route for preparing stoichiometric nickel sulfide nanocrystals with well-defined crystalline structures, compositions and morphologies.

2.5 References

[1] G. Kullerud, R.A. Yund, J. Petrol. 3 (1962) 126–175.

[2] J.C. Barry, S. Ford, J. Mater. Sci. 36 (2001) 3721–3730.

[3] K. Ramasamy, M.A. Malik, P. O'Brien, J. Raftery, M. Helliwell, Chem. Mater. 22 (2010) 6328–6340.

[4] M. V. Swain, J. Mater. Sci. 16 (1981) 151–158.

[5] A. Ghezelbash, B.A. Korgel, Langmuir 21 (2005) 9451–9456.

[6] J.C.& Huan Pang, Chengzhen Wei, Xuexue Li, Guochang Li, Yahui Ma, Sujuan Li, Z. Jiangshan, Sci. Rep. 4 (2014) 3577.

[7] Z. Fangming, B. Geng, Y. Guo, L. Wang, J. Alloys Compd. 482 (2009) 1–5.

[8] X. Li, J. Shen, N. Li, M. Ye, Mater. Lett. 139 (2015) 81–85.

[9] X. Sun, J. Dou, F. Xie, Y. Li, M. Wei, Chem. Commun. (Camb). 50 (2014) 9869–71.

[10] H. Geng, S.F. Kong, Y. Wang, J. Mater. Chem. A 2 (2014) 15152.

[11] L. Mi, Q. Ding, W. Chen, L. Zhao, H. Hou, C. Liu, C. Shen, Z. Zheng, Dalton Trans. 42 (2013) 5724–30.

[12] J.M. Falkowski, N.M. Concannon, B. Yan, Y. Surendranath, J. Am. Chem. Soc. 137 (2015) 7978–81.

[13] L.L. Feng, G. Yu, Y. Wu, G.D. Li, H. Li, Y. Sun, T. Asefa, W. Chen, X. Zou, J. Am. Chem. Soc. 137 (2015) 14023–14026.

[14] K.P.R. Pisharody, C. Visiting, Prog. Solid State Chem. 10 (1974) 207–270.

[15] Y. Zhang, W. Sun, X. Rui, B. Li, H.T. Tan, G. Guo, S. Madhavi, Y. Zong, Q. Yan, Small 11 (2015) 3694–3702.

[16] C. An, Z. Zhang, X. Chen, Y. Liu, Mater. Lett. 60 (2006) 3631–3634.

[17] P.F. Yin, L.L. Sun, C. Zhou, Y.H. Sun, X.Y. Han, C.R. Deng, Bull. Mater. Sci. 38 (2015) 95–99.

[18] A. Ghezelbash, M.B. Sigman, B.A. Korgel, Nano Lett. 4 (2004) 537–542.

[19] Q. Liu, A. Díaz, A. Prosvirin, Z. Luo, J.D. Batteas, Nanoscale (2014) 8935–8942.

[20] K. Aso, A. Hayashi, M. Tatsumisago, Inorg. Chem. 50 (2011) 10820–10824.

[21] M. Salavati-Niasari, G. Banaiean-Monfared, H. Emadi, M. Enhessari, Comptes Rendus Chim. 16 (2013) 929–936.

[22] A. Sobhani, M. Salavati-Niasari, Superlattices Microstruct. 59 (2013) 1–12.

[23] Y.H. R.Karthikeyan, M. Navaneethan, J. Archana, D. Thangaraju, M. Arivanandhan, Dalton Trans. 43 (2014) 17445–17452.

[24] A. Manthiram, Y.U. Jeong, J. Solid State Chem. 681 (1999) 679–681.

[25] A.L. Abdelhady, M.A. Malik, P. O'Brien, F. Tuna, J. Phys. Chem. C 116 (2012) 2253–2259.

[26] S. Mlowe, D.J. Lewis, M.A. Malik, J. Raftery, E.B. Mubofu, P. O'Brien, N. Revaprasadu, Dalt. Trans. 45 (2016) 2647–2655.

[27] J.H.L. Beal, P.G. Etchegoin, R.D. Tilley, J. Phys. Chem. C 114 (2010) 3817–3821.

[28] S.N. Shukla, P. Gaur, N. Rai, Appl. Nanosci. (2014) 583–593.

[29] A. Roffey, N. Hollingsworth, H.-U. Islam, M. Mercy, G. Sankar, C.R.A. Catlow, G. Hogarth, N.H. de Leeuw, Nanoscale 8 (2016) 11067–11075.

[30] X. Shen, J. Sun, G. Wang, J. Park, K. Chen, Mater. Res. Bull. 45 (2010) 766–771.

[31] E. Sathiyaraj, G. Gurumoorthy, S. Thirumaran, New J. Chem. 39 (2015) 5336–5349.

[32] B. Arul Prakasam, M. Lahtinen, A. Peuronen, M. Muruganandham, E. Kolehmainen, E. Haapaniemi, M. Sillanpää, Inorganica Chim. Acta 425 (2015) 239–246.

[33] N. Hollingsworth, A. Roffey, H. Islam, M. Mercy, A. Roldan, W. Bras, M. Wolthers, C.R.A. Catlow, G. Sankar, G. Hogarth, N.H. de Leeuw, Chem. Mater. 26 (21) (2014) 6281–6292.

[34] A. Radha, M. Seshasayee, G. Aravamudan, Acta Crystallogr. Sect. C Cryst. Struct. Commun. 44 (1988) 1378–1381.

[35] K.S. Siddiqi, S. a a Nami, Y. Chebude, J. Brazillian Chem. Soc. 17 (2006) 107–112.

[36] C. Anastasiadis, G. Hogarth, J.D.E.T. Wilton-Ely, Inorganica Chim. Acta 363 (2010) 3222–3228.

[37] A.G. Orpen, L. Brammer, F.H. Allen, O. Kennard, D.G. Watson, R. Taylor, J. Chem. Soc. Dalt. Trans. (1987) S1–S83.

[38] J. Einstein, F.W.B and Field, Acta Crystallogr. Sect. B Struct. Sci. Cryst. Eng. Mater. 0 (1973) 2928–2930.

[39] I.J. Bruno, J.C. Cole, M. Kessler, J. Luo, W.D.S. Momerwell, L.H. Purkis, B.R. Smith, R. Taylor, R.I. Cooper, S.E. Harris, A.G. Orpen, J. Chem. Inf. Comput. Sci. 44 (2004) 2133–2144.

[40] C.R. Groom, I.J. Bruno, M.P. Lightfoot, S.C. Ward, Acta Crystallogr. Sect. B Struct. Sci. Cryst. Eng. Mater. 72 (2016) 171–179.

[41] N. Hollingsworth, H. Islam, M. Mercy, G. Sankar, G. Hogarth, N.H. De Leeuw, (2016) 11067–11075.

[42] Y. Chan, Chem. Mater. 26(21) (2014) 6120.

[43] Q. Li, C.W. Kartikowati, S. Horie, T. Ogi, T. Iwaki, K. Okuyama, Sci. Rep. 7 (2017) 9894.

[44] R. Koole, J. Phys. Chem. C 113 (2009) 6511–6520.

CHAPTER THREE

HETEROCYCLIC DITHIOCARBAMATO-NICKEL(II) COMPLEXES: SINGLE MOLECULAR PRECURSORS FOR NICKEL SULFIDE THIN FILMS

3.1. Introduction

The synthesis of phase-pure nanomaterials of many metal chalcogenides with multiple phases remains a challenge when using bottom-up synthetic techniques [1-3]. Nickel sulfide has many phases which are notoriously difficult to control. The predominant phases produced are heazlewoodite (Ni_3S_2), polydymite (Ni_3S_4), vaesite (NiS_2) and millerite ($Ni_{1-x}S$) [4]. Generally, the nickel sulfide system contains a number of extra phases such as NiS (α and ß), NiS_2, Ni_3S_2, Ni_3S_4, and Ni_7S_6, Ni_9S_8 and α-$Ni_{3+x}S_2$ [5].

The Ni-S system is considered more complex than other transition metal sulfides systems of cobalt or iron [5, 6]. Nickel sulfide in its various stoichiometries has different and important applications as a semiconducting material [2], metal insulator [7] and as a hydrosulfurization catalyst [8, 9]. Nickel sulfide nanomaterials are also useful for application in solar cell and selective solar coating [10], IR detectors [11], and rechargeable lithium batteries [12] and the hydrogen evolution reaction (HER) [13].

The morphology of nanomaterials plays an important role to dictate properties that suit specific applications. One-dimensional materials, such as nanowires, nanorods, and nanotubes, for instance, have stimulated great interest because of their unique electrical and optical properties associated with their dimensionality [14]. Geometrically, nanorods can be elongated relative to other crystallographic orientations, thus optimizing the desired properties in nano devices [15]. Nickel sulfide nanomaterials in the form that includes urchins [16], cuboids and nanobelts [17] have also been reported.

Ni_3S_2 and NiS have related applications as semiconductors and have been widely studied for their application in lithium batteries [18] and supercapacitors [19]. Ni_3S_2 is also a potent catalyst for the HER and oxygen evolution reaction (OER) under mild conditions [20, 21]. Efficient catalysts for redox reactions of water to generate H_2 and O_2 are an important component for storage of renewable energy in the form of chemical fuels [21]. Ni_3S_2 has been reported to increase the production of hydrogen generation in reactions where it catalyses the generation of hydrogen from water at 300 °C [22].

Despite the importance of these phases, it has been a challenge to design a protocol that assures the efficient and inexpensive way of preparing them under solvothermal conditions in

their pure phases. In chapter 2, the use of different dithiocarbamate in primary amines to obtain rare phases of Ni_3S_4 and Ni_3S_2 nanoparticles via hot injection route was demonstrated [23]. Nickel sulfide thin films can be deposited by using the same complexes as a different route to stabilize the multiple phases of Ni-S via the aerosol assisted chemical vapour deposition technique. The role played by the nickel complexes during its thermal decomposition to direct certain phase for Ni-S was reported by Hogarth *et al.* [24]. It has been shown that the precursor decomposition pathway is key to the obtained Ni-S phase system. A number of studies have been performed for the preparation of Ni-S systems by changing parameters such as temperature, time, concentration and surfactants in order to tune morphologies and phases in solvothermal protocols [25].

The synthetic protocols of Ni-S system to obtain pure phases and desired morphologies for nanoparticles and thin films have been reported to pose many challenges [26, 27]. Studies indicating correlation between the use of SSPs to tune morphologies and yet obtain pure phases are few and limited. In this this chapter, the use of *bis*(piperidinyldithiocarbamato)nickel(II) (**1**), *bis*(tetrahydroquinolinyldithiocarbamato)nickel(II) (**2**) and *bis*(N'-ethyl-N-piperazinylcarbodithioato-S,S')-Nickel(II) (**3**) complexes for the deposition of phase-pure NiS thin films is reported.

3.2. Experimental details

3.2.1. Materials and methods

Hexadecyalamine (HDA) 98%, oleyamine (OLA) 99%, dodecylamine (DDA), tri-n-octylphosphine (TOP) 90%, piperidine 99%, tetrahydroisoquinoline 99%, ethylpiperazine 99%, carbon disulfide 99%, nickel acetate tetrahydrate (Sigma Aldrich), sodium hydroxide 98%, methanol 99.5%, chloroform, acetone and hexane were used as purchased without any further purification.

3.2.2. Synthesis of ligands and nickel complexes

Synthesis and characterization of ligands and complexes (**1-3**) are as described in the experimental section 2.2 of chapter 2.

3.2.3. Aerosol Assisted Chemical Vapour Deposition (AACVD) of nickel sulfide thin films

Nickel sulfide thin films were deposited on glass substrates by using single molecular precursors (**1-3**). In a typical deposition procedure, 200 mg (0.526 mmol) of [Ni(Pip-dtc)$_2$] (**1**) was dissolved in 25.0 mL of chloroform in a two-neck 100 mL round bottomed flask fitted with a glass inlet that allowed argon, the carrier gas, to pass into the solution to assist the transfer of precursor aerosols. Argon gas was controlled by a flow gauge (160 mL min^{-1}). A 1 cm x 1 cm glass substrate, thoroughly cleaned by sonication in ethanol and dried in oven, was inserted into the reactor tube, which was then placed in a Carbolite furnace. The precursor solution in a two neck-round bottomed flask, kept in a cold-water bath above the GoldAir ultrasonic humidifier (model-GMH-200), was connected to the reactor tube. The aerosol droplets of the precursor solution were transferred by the carrier gas into the hot zone of the reactor. Both the solvent and the precursor were evaporated and the precursor vapor reached the heated substrate surface where thermally induced reactions and film deposition took place. The reaction temperatures were varied at 350 °C, 400 °C, 450 °C and 500 °C. Figure 1.1 depicts the AACVD kit used in this work.

Figure 3.1: The AACVD setup during thin film deposition.

3.2.4. Characterization techniques

Characterization techniques used in this work are detailed in chapter 2 of this thesis.

3.2.4.1. Scanning electron microscopy (SEM) and Energy dispersive X-ray spectroscopy (EDX)

The surface morphology and structure of the film was determined using a Zeiss Sigma VP-03-67 field emission gun scanning electron microscopy (FEGSEM), equipped with an Oxford instrument X-max 50 EDX detector. Prior to SEM characterization, samples were carbon-coated by using a Quorum coater (Model Q150TE), to prevent samples from charging during analyses.

3.3. Results and discussion

3.3.1. Synthesis of single source precursors

The synthesis of ligands and complexes are outlined in a two-step reaction Scheme 3.1. The complex was obtained as a stable compound at room temperature, formed from the reaction between the ligand and nickel acetate tetrahydrate at a ratio of 2:1. Elemental and spectroscopic analyses corroborate the mechanistic formation of the complex as seen in the reaction scheme. Both the ligand and the complex were obtained in good yields, with the complex giving greenish crystallites soluble in common organic solvents such as chloroform and dichloromethane.

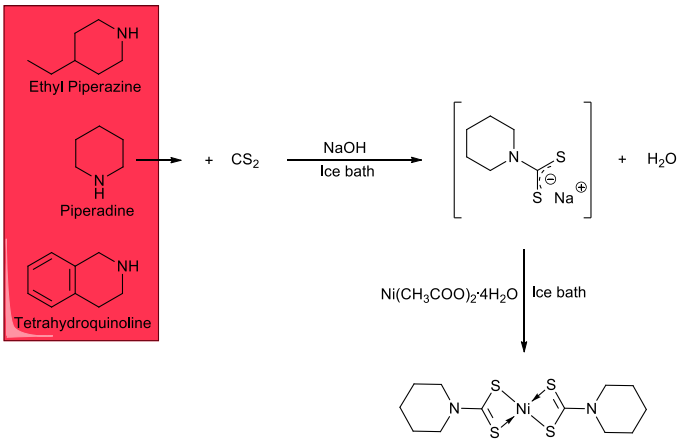

Scheme 3.1: The preparation scheme of ligands to complexes.

3.3.2. Nickel sulfide thin films

Nickel sulfide thin films were deposited on glass substrates by the aerosol assisted chemical vapour deposition (AACVD) technique, using chloroform as a solvent medium. The films were black in colour, confirming the formation of nickel sulfide materials. Film thickness was also calculated by weighing the glass substrate before deposition and after deposition using equation (**1**):

$$t = \frac{m}{A\rho} \quad \text{..... (1)}$$

where t is the thickness of the thin film deposited, m is the mass gained after deposition; A is the area of the coated thin film and is ρ is the density of nickel sulfide (5.87 g cm^{-3}). Prior to characterization the loosely bound NiS particles on the substrate were removed by etching the films in 3 % HCl for 5 s. Film thickness of NiS was determined by using gravimetric weight difference method; a sensitive micro-balance was used. Table 3.1 shows the calculated thickness for all three complexes used. The mass of these quantities was taken by weighing the mass of the glass substrate before deposition (m_1) and mass of substrate after deposition (m_2). Thus, mass of nanomaterial deposited $m = m_2 - m_1$.

Table 3.1: Film thickness of nickel sulfide thin films deposited on glass by AACVD.

Temperature °C	**Ni(Pip dtc)$_2$ (1)**	**Ni (THQ dtc)$_2$ (2)**	**Ni(Etpz dtc)$_2$ (3)**
	Thickness (*t*) in µm	**Thickness (*t*) in µm**	**Thickness (*t*) in µm**
350	4.22	4.61	4.45
400	4.67	4.82	4.62
450	4.81	4.93	4.92
500	4.94	4.95	4.94

A plot of thickness versus deposition temperature of the films is shown in Figure 3.2. The trend indicates that film thickens increases with an increase in temperature, up to a certain limit due to the formation of outer porous layer of NiS. From the graph, a very sharp increase in thickness after 400 ºC can be attributed to the higher decomposition of the aerosols at higher

temperatures. The relatively more stable complex (**1**) tend to deposit less at the beginning due to low decomposition temperature while the relatively less stable complex (**2**) has larger thickness at lower temperature.

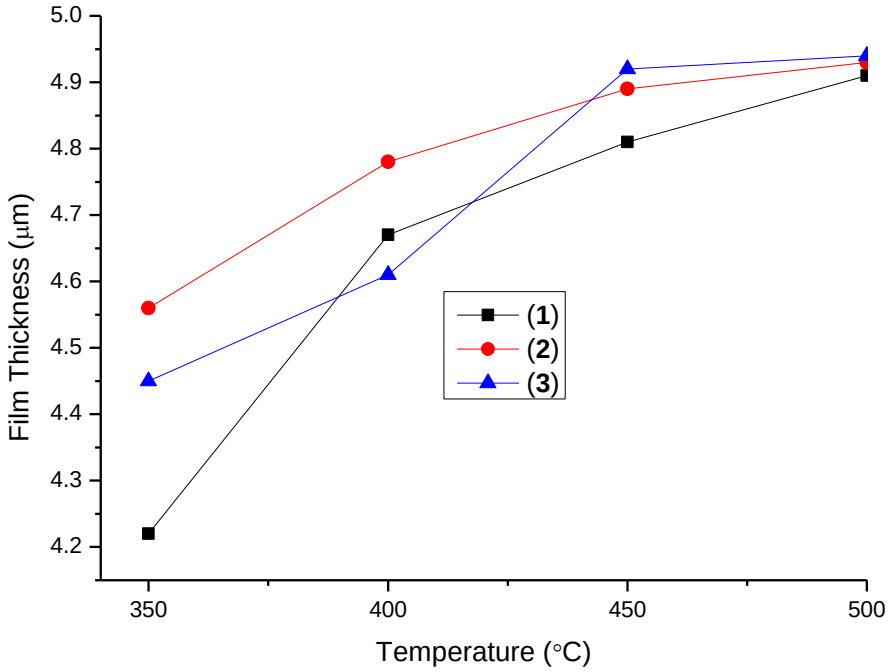

Figure 3.2: A graph showing film thickness growth versus temperature of deposition

3.3.3. SEM, EDX and Elemental Mapping analyses

The scanning electron microscopy (SEM) micrographs of the NiS thin films deposited from complex (**1**) show uniform morphologies. The deposition at 350 °C was not successful, attributed to the unconducive parameters to initiate the decomposition of complex (**1**). Deposition was only possible above 400 °C. Thin films deposited at 400 °C (Figure 3.3 b) and 450 °C (Figure 3.3 c) display mostly cubic-like and dumbbell-like morphology, respectively. Furthermore, there is evidence of nanoclusters possibly formed from agglomerated nanoparticles at both temperatures. As the temperature increases to 500 °C (Figure 3.3 d), the deposited films are composed of irregular-shaped nanoparticles which appear to form stacked structures. The EDX spectroscopy analysis indicates a percentage atomic ratio of 57.1:42.9 (Ni:S) which is in close agreement to NiS phase (Figure 3.3 e).

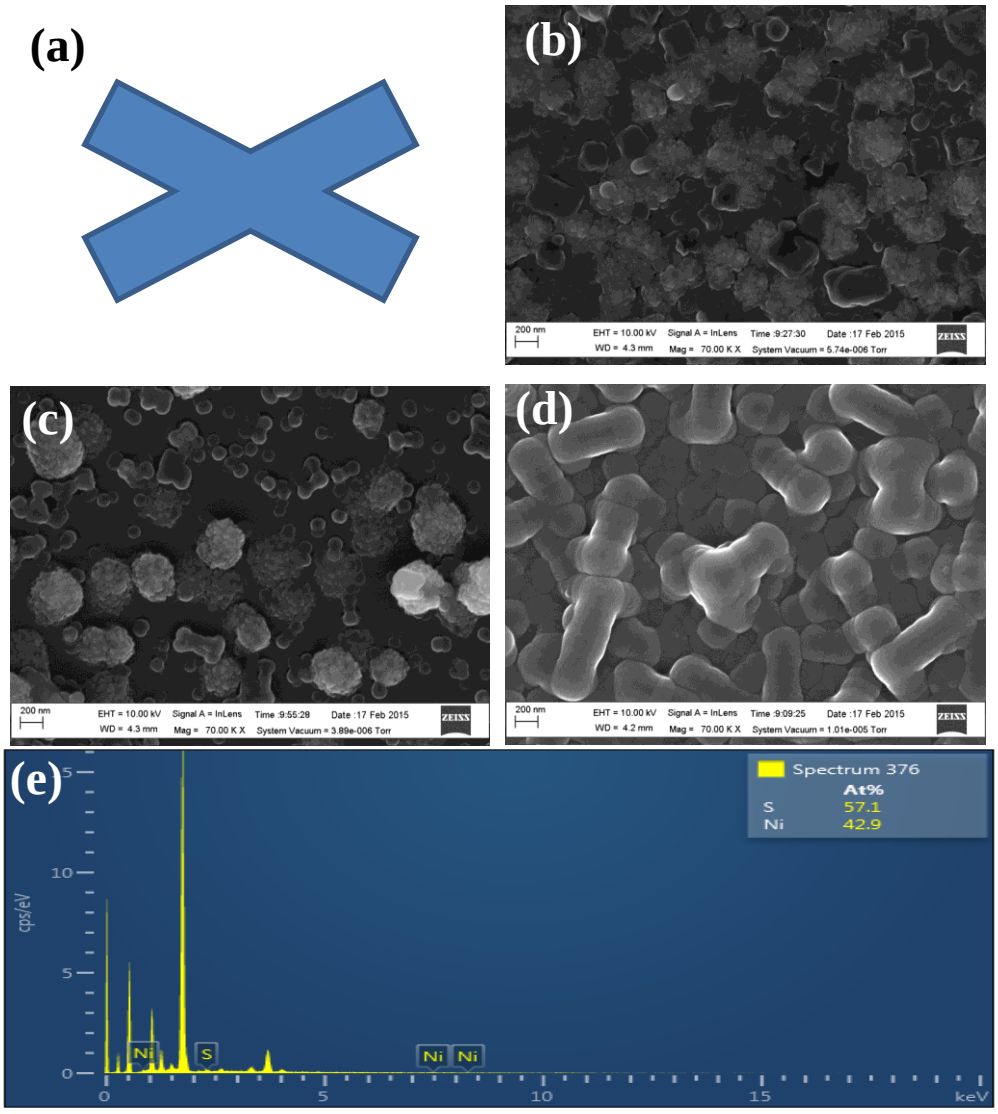

Figure 3.3: SEM images for NiS thin films deposited from complex (**1**) at (a) 350 °C, (b) 400 °C, (c) 450 °C (d) 500 °C and (e) EDX spectrum for film deposited at 400 °C. Scale bar: 200 nm. *Note: At the temperature of 350 °C there was no deposition due to high stability of complex (**1**). Deposition was only afforded when temperature was raised to 400 °C.*

Long rod-like morphology of NiS thin films deposited from complex (**2**) at 350 °C was observed (Figure 3.4 a). An increase in deposition temperature from 400 °C (Figure 3.4 b) to 450 °C (Figure 3.4 c) resulted in shorter and thicker rod-like morphology which transforms further to irregular cubic-like stacked plates at 500 °C (Figure 3.4 d). The EDX spectroscopy analysis indicated the atomic percentage ratio of 59.9:40.1 (Ni:S) which is closer to the expected values for the NiS phase (Figure 3.4 e).

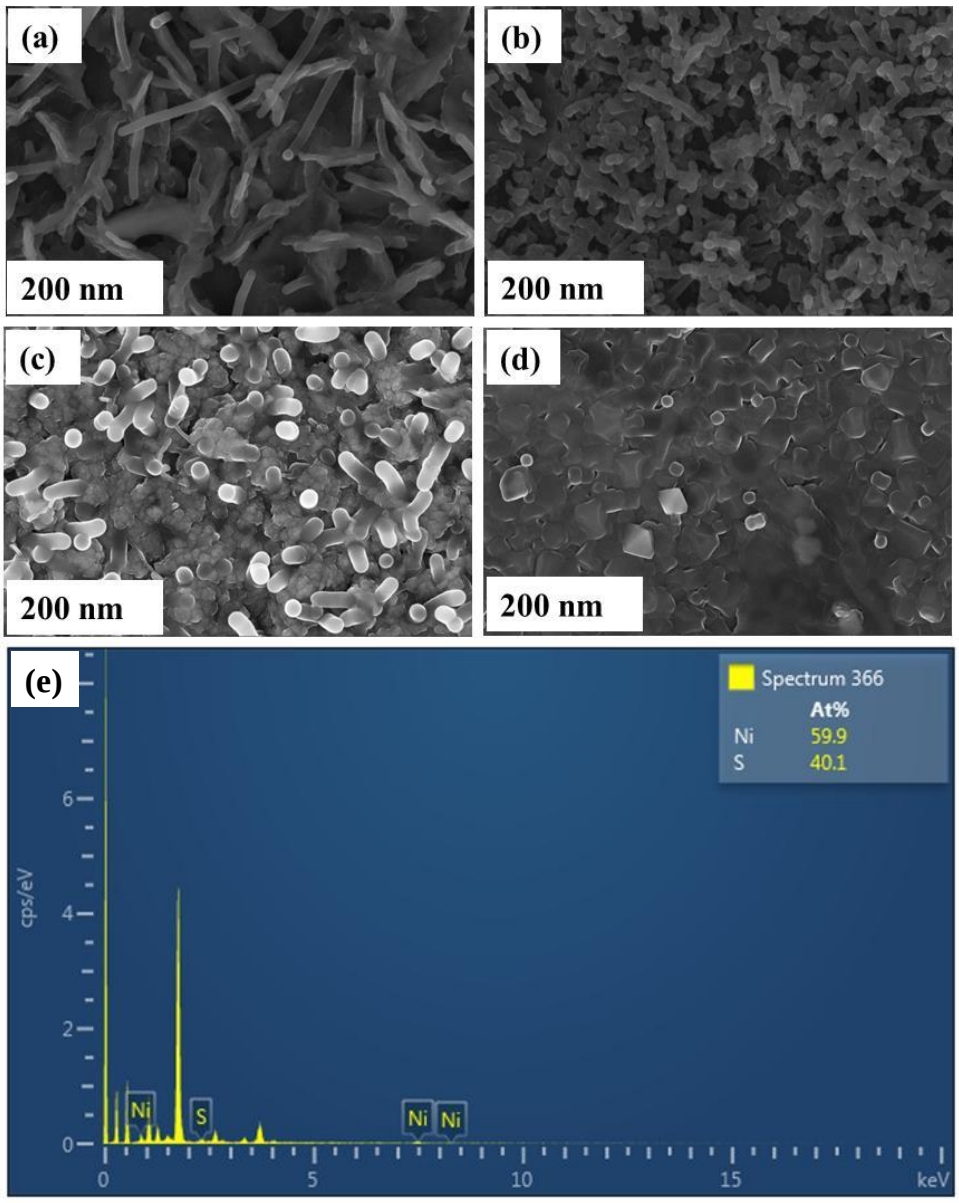

Figure 3.4: SEM images for nickel sulfide (NiS) thin films from complex (**2**) deposited at (a) 350 °C, (b) 400 °C, (c) 450 °C and (d) 500 °C.

SEM micrograph for thin films deposited from complex (**3**) at 350 °C and 400 °C displayed small fibre-like morphology (Figure 3.5 a and b, respectively). A mixture of fibre-like and cubic-like morphology was observed at deposition temperatures of 450 °C, while irregular-shaped agglomerates were observed at 500 °C. The EDX spectroscopy analysis (Figure 3.5 e) shows an elemental atomic percentage to be 62.9% for Ni and 37.1% for S which denotes good stoichiometry for NiS.

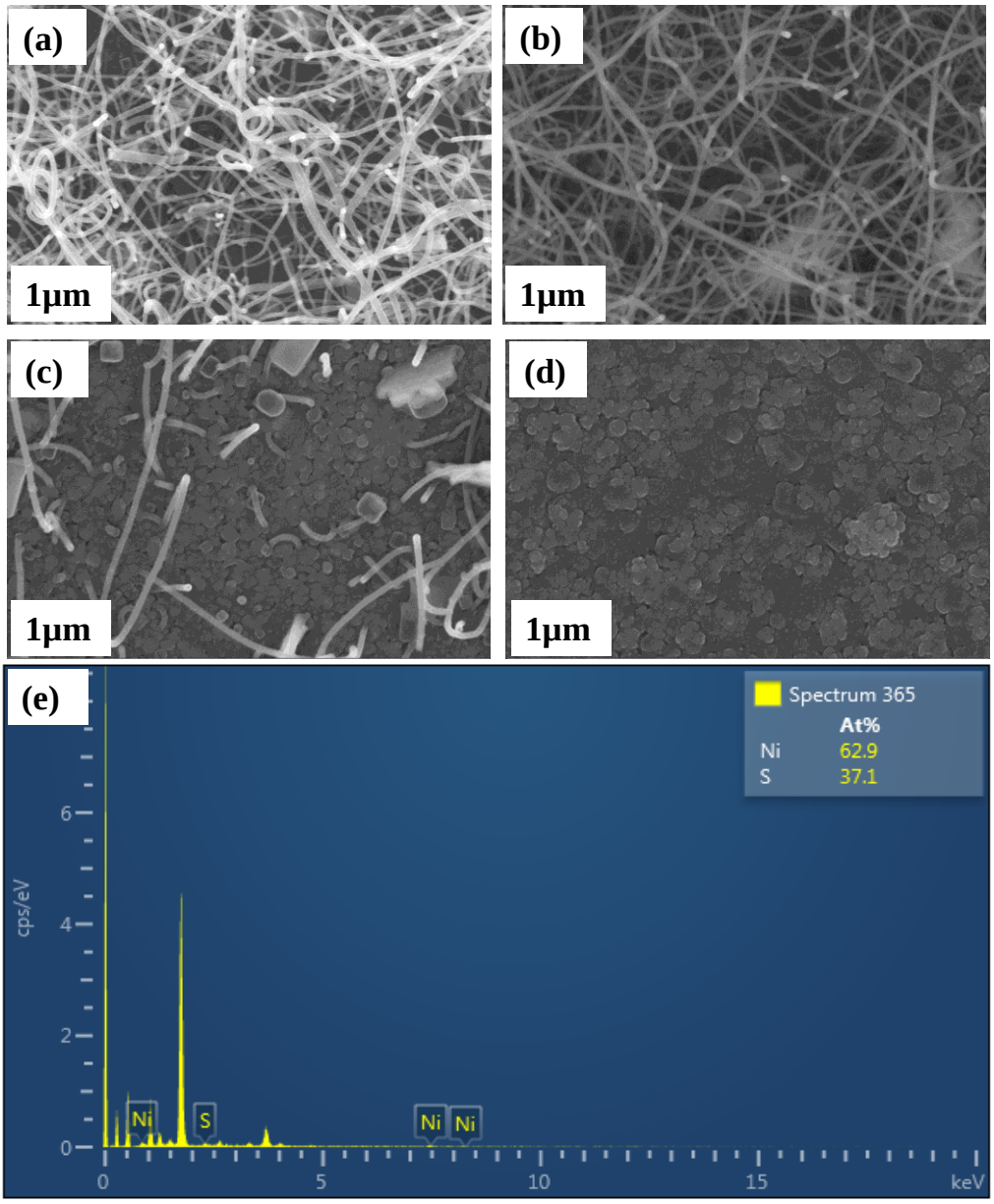

Figure 3.5: SEM images for nickel sulfide (NiS) thin films complex (**3**) deposited at (a) 350 °C, (b) 400 °C, (c) 450 °C and (d) 500 °C.

The plausible mechanism for the morphological evolution of the deposited Ni-S thin films obtained from complex (**3**) is given in Figure 3.6. Step 1 begins with the complex decomposing through the loss of the organic moiety. Since the complex is coordinated in a square planar configuration, it linearly reassembles the Ni-S part, in a stacking mode that results in the formation of fibres at lower temperatures. Step 2 involves a thermodynamic process where the fibre thickness increases possibly through the dissolution-precipitation-based mechanism

(Ostwald ripening) followed by stacking into larger fibres. These larger fibres, in step 3, ultimately start disintegrating into shorter rod-like particles which eventually agglomerate into irregular-shaped stacked particles.

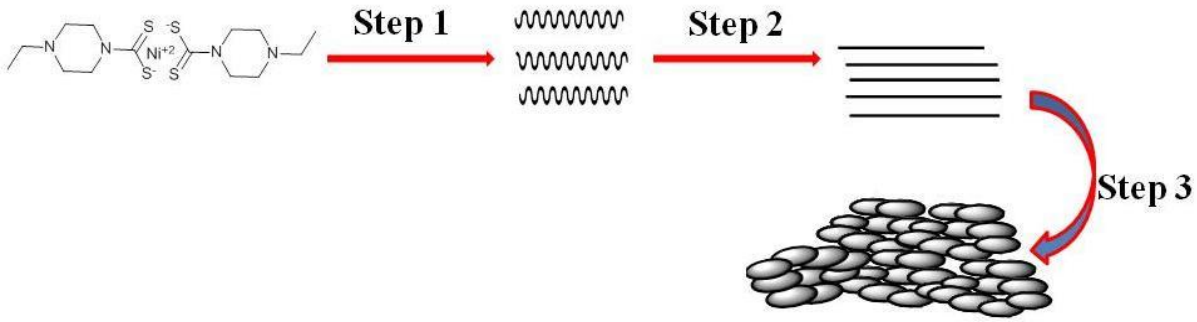

Figure 3.6: Proposed mechanistic steps for the morphology transformation of NiS thin films deposited from complex (**3**).

The elemental mapping for the representative samples is presented in Figure 3.7. There is a compositional uniformity of the films for both Ni and S elements.

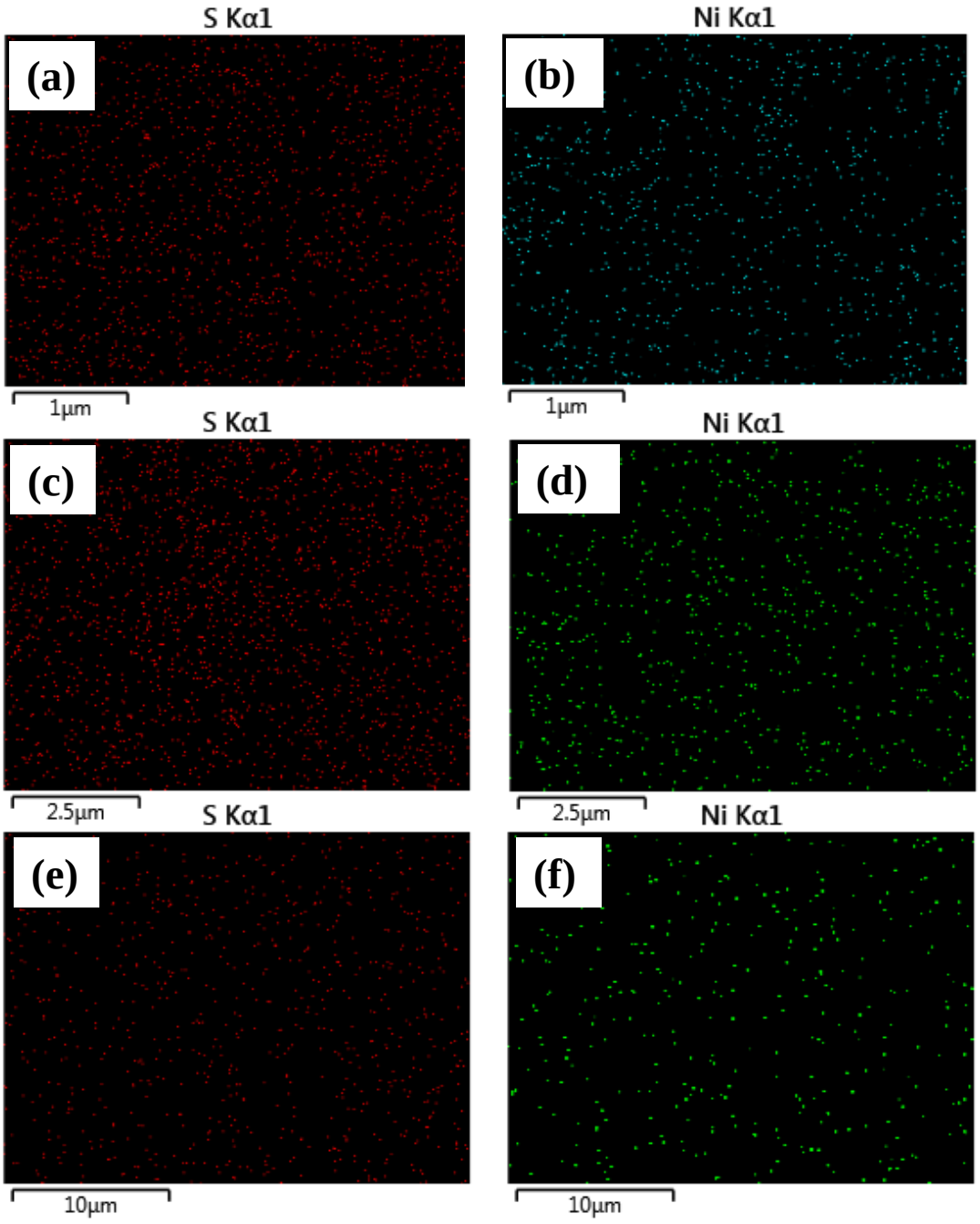

Figure 3.7: EDX spectroscopy elemental mapping on NiS thin films obtained from (a,b) complex (**1**), (c,d) complex (**2**) and (e,f) complex (**3**) at 400 °C.

3.3.4. Powder X-ray diffraction studies

The microelemental analysis of the representative thin films obtained from all three complexes using EDX spectroscopy, suggested a Ni_2S_3 phase. Surprisingly, the p-XRD patterns (Figures 3.8-3.10) were matched to millerite (rhombohedral ß-NiS, card number: 00-012-0041) with space group of R3m (160), through the reflection peaks observed at 2θ values of 32.21°, 37.34° and 67.39° indexed to (300), (220) and (600), respectively. Thus, the combined data suggests that the films are nickel-rich NiS. However, Figure 3.10 has an additional diffraction peak at 2θ value of 44.38°, marked with X. The peak was matched to a diffraction plane (202) of Ni_2S_3 (card number 01-085-1802) impurity. In all films, there is a preferential growth towards hkl plane (300), corroborating the formation of fibrous NiS.

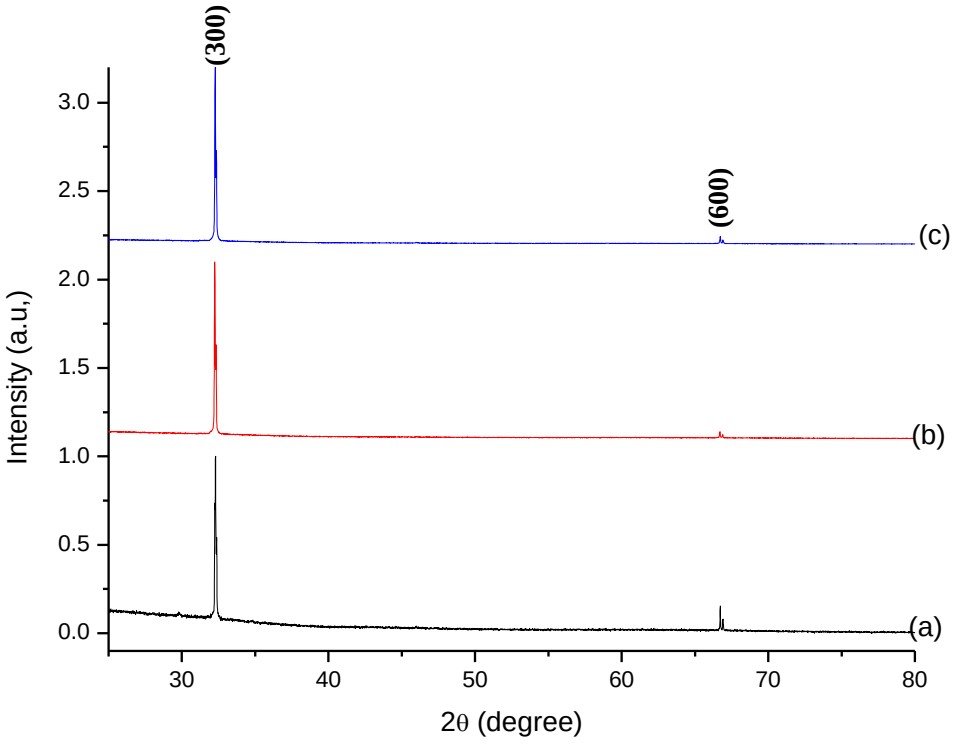

Figure 3.8: p-XRD patterns of NiS thin films deposited from complex (1) at (a) 400 °C, (b) 450 °C and (c) 500 °C.

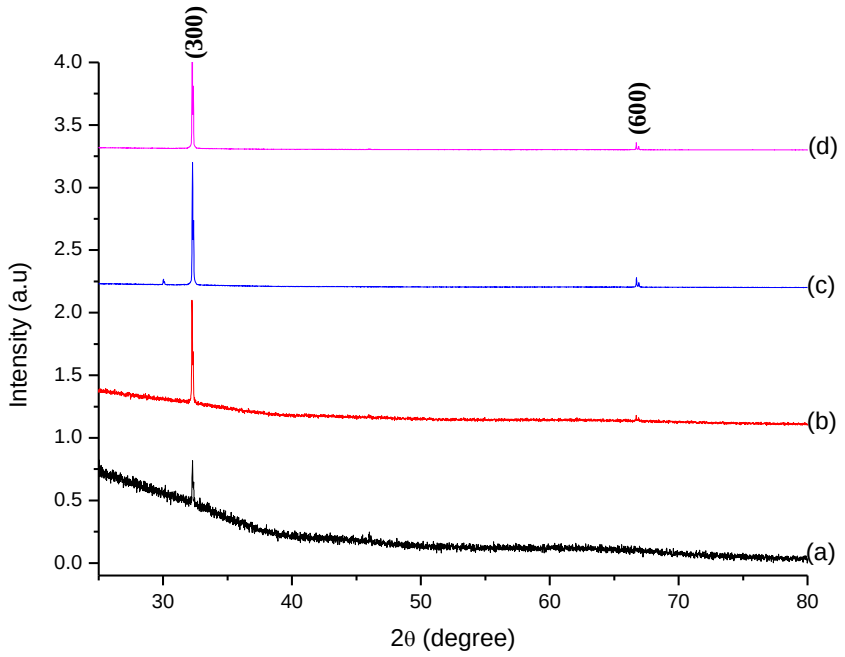

Figure 3.9: p-XRD patterns of NiS thin films deposited from complex (**2**) at (a) 350 °C, (b) 400 °C, (c) 450 °C and (d) 500 °C.

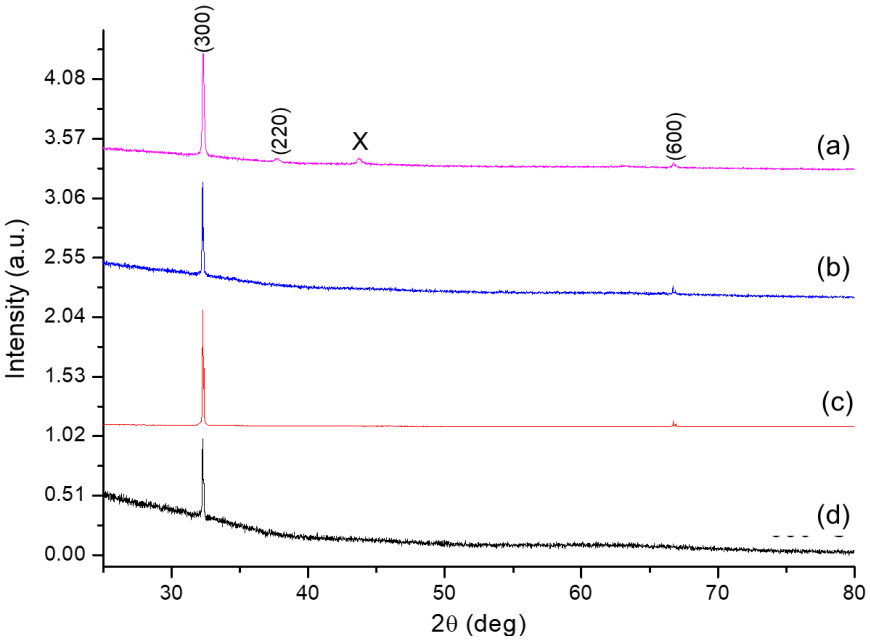

Figure 3.10: p-XRD patterns of NiS thin films deposited from complex (**3**) at (a) 350 °C, (b) 400 °C, (c) 450 °C and (d) 500 °C. X denotes a Ni_2S_3 (card number 01-085-1802) impurity.

3.3.5. Optical absorbance analysis

The absorption spectra of the NiS thin film were recorded in the UV-Vis region as shown in Figures 3.12-3.13. The absorption spectra of the NiS thin films show absorbance in the visible region of the solar spectrum. This indicates the possibility of this material to be used in photoelectrochemical cells, photovoltaics and other optoelectric devices [19]. The UV-Vis absorption spectra, specifically from complex (**1**), have a maximum absorption below 300 nm instigating high energy bang gap as a highly-quantized materials. A plausible explanation for the thin films deposited from complex (**1**) being more quantized than complexes (**2**) and (**3**) counterparts is the effect of morphology (figure 3.3). In the UV-Vis spectroscopy technique, the edges of rods or plates are able to absorb incident rays, thus, detected as highly quantized nanomaterial albeit their large lateral sizes observed in Figure 3.3.

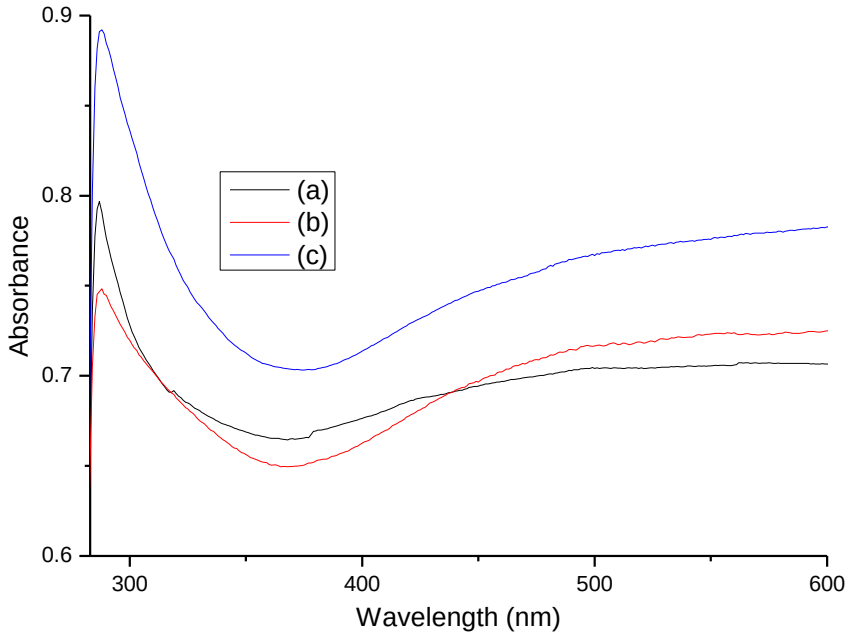

Figure 3.11: NiS thin films UV-Vis for complex (**1**) at various temperatures (a) 400 °C (b) 450 °C and (c) 500 °C.

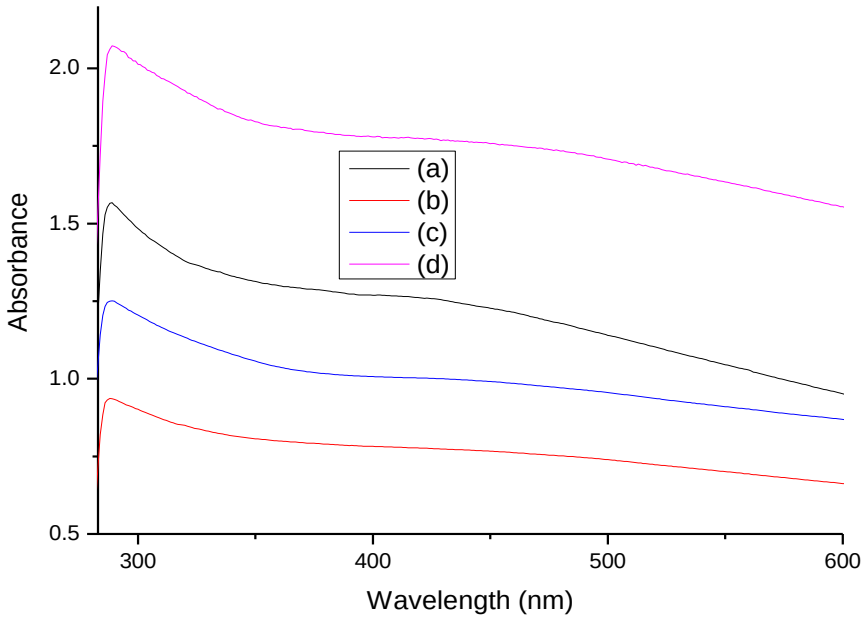

Figure 3.12: NiS thin films UV-Vis for complex (**2**) at various temperatures (a) 350 °C (b) 400 °C and (c) 450 °C and (d) 500 °C.

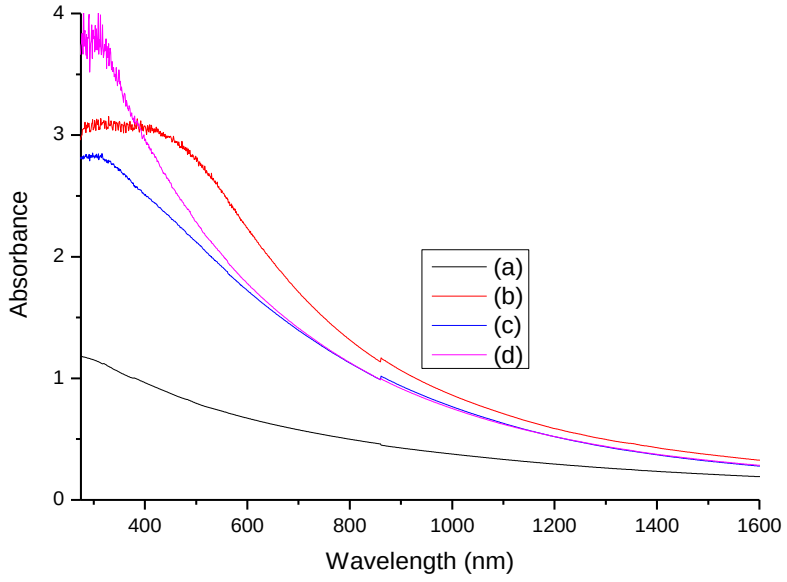

Figure 3.13: NiS thin films UV-Vis for complex (**3**) at various temperature (a) 350 °C (b) 400 °C and (c) 450 °C and (d) 500 °C

3.4. Conclusion

Aerosol assisted chemical vapour deposition (AACVD) method has been used to prepare NiS thin films. Various parameters were varied to afford both morphology and pure phase control of the as-synthesized thin films. Phase-pure NiS was obtained when thin films were deposited via AACVD using complexes (**1-3)**. As temperature increases, the particle size increases and hence the decrease in energy band gap. SEM images of the as-synthesized materials formation of particles with various shapes and sizes, dependent on synthetic conditions. UV-Vis measurements indicate quantum confinement of the as-prepared thin films.

3.5. References

[1] A.L. Abdelhady, M. A. Malik, P. O'Brien, F. Tuna, J. Phys. Chem. C 116 (2011) 2253–2259.

[2] L. Tian, L.Y. Yep, T.T. Ong, J. Yi, J. Ding, J.J. Vittal, Cryst. Growth Des. 9 (2009) 352–357.

[3] J.H.L. Beal, P.G. Etchegoin, R.D. Tilley, J. Phys. Chem. C 114 (2010) 3817–3821.

[4] G. Kullerud, R.A. Yund, J. Petrol. 3 (1962) 126–175.

[5] J.C. Barry, S. Ford, J. Mater. Sci. 36 (2001) 3721–3730.

[6] M. V. Swain, J. Mater. Sci. 16 (1981) 151–158.

[7] H.C. Hiscocks, S.E.R, Webber, J. Mater. Sci. 9 (1974) 9–11.

[8] N. Alam, M.S. Hill, G. Kociok-Köhn, M. Zeller, M. Mazhar, K.C. Molloy, Chem. Mater. 20 (2008) 6157–6162.

[9] R.D. Tilley, D.A. Jefferson, J. Phys. Chem. B 106 (2002) 10895–10901.

[10] M.-R. Gao, Y.-F. Xu, J. Jiang, S.-H. Yu, Chem. Soc. Rev. 42 (2013) 2986–3017.

[11] B.S. Harrison, Carbon Nanotub. (n.d.) 554–561.

[12] K. Aso, H. Kitaura, A. Hayashi, M. Tatsumisago, J. Mater. Chem. 21 (2011) 2987.

[13] J.M. Falkowski, N.M. Concannon, B. Yan, Y. Surendranath, J. Am. Chem. Soc. 137 (2015) 7978–81.

[14] A. Ghezelbash, B.A. Korgel, Langmuir 21 (2005) 9451–9456.

[15] D.P. Dinega, M.G. Bawendi, Angew. Chemie Int. Ed. 38 (1999) 1788–1791.

[16] X. Shen, J. Sun, G. Wang, J. Park, K. Chen, Mater. Res. Bull. 45 (2010) 766–771.

[17] L. Wang, Y.Z. Ã, H. Li, Q. Li, Y.Q. Ã, J. Solid State Chem. 183 (2010) 223–227.

18 X.Y. and T.L. Shibing Ni, J. Mater. Chem. 22 (2012) 2395–2397.

[19] B. You, Y. Sun, Adv. Energy Mater. 6 (2016) 1–7.

[20] L.L. Feng, G. Yu, Y. Wu, G.D. Li, H. Li, Y. Sun, T. Asefa, W. Chen, X. Zou, J. Am. Chem. Soc. 137 (2015) 14023–14026.

[21] S. Qu, J. Huang, J. Yu, G. Chen, W. Hu, M. Yin, R. Zhang, S. Chu, C. Li, ACS Appl. Mater. Interfaces 9 (2017) 29660–29668.

[22] Y. Wang, F. Jin, X. Zeng, C. Ma, F. Wang, G. Yao, Z. Jing, Appl. Energy 104 (2013) 306–309.

[23] C. Gervas, S. Mlowe, M.P. Akerman, I. Ezekiel, T. Moyo, N. Revaprasadu, Polyhedron 122 (2017) 16–24.

[24] N. Hollingsworth, A. Roffey, H. Islam, M. Mercy, A. Roldan, W. Bras, M. Wolthers, C.R.A. Catlow, G. Sankar, G. Hogarth, N.H. de Leeuw, Chem. Mater. 26 (21) (2014) 6281–6292.

[25] A. Roffey, N. Hollingsworth, H.-U. Islam, M. Mercy, G. Sankar, C.R.A. Catlow, G. Hogarth, N.H. de Leeuw, Nanoscale 8 (2016) 11067–11075.

[26] A. Ghezelbash, M.B. Sigman, B.A. Korgel, Nano Lett. 4 (2004) 537–542.

[27] Y.H.R. Karthikeyan, M. Navaneethan, J. Archana, D. Thangaraju, M. Arivanandhan, Dalton Trans. 43 (2014) 17445–17452.

[28] D.C. Onwudiwe, P. a Ajibade, Int. J. Mol. Sci. 12 (2011) 1964–78.

[29] I.J. Bruno, J.C. Cole, M. Kessler, J. Luo, W.D.S. Momerwell, L.H. Purkis, B.R. Smith, R. Taylor, R.I. Cooper, S.E. Harris, A.G. Orpen, J. Chem. Inf. Comput. Sci. 44 (2004) 2133–2144.

[30] C.R. Groom, I.J. Bruno, M.P. Lightfoot, S.C. Ward, Acta Crystallogr. Sect. B Struct. Sci. Cryst. Eng. Mater. 72 (2016) 171–179.

[31] Q. Liu, A. Díaz, A. Prosvirin, Z. Luo, J.D. Batteas, Nanoscale 6 (2014) 8935–42.

[32] C.-H. Lai, M.-Y. Lu, L.-J. Chen, J. Mater. Chem. 22 (2012) 19.

[33] A.G. Orpen, L. Brammer, F.H. Allen, O. Kennard, D.G. Watson, R. Taylor, J. Chem. Soc. Dalt. Trans. (1987) S1–S83.

[34] A.L. Patterson, Phys. Rev. 56 (1939) 978–982.

[35] R. Koole, J. Phys. Chem. C 113 (2009) 6511–6520.

[36] M. Salavati-Niasari, G. Banaiean-Monfared, H. Emadi, M. Enhessari, Comptes Rendus Chim. 16 (2013) 929–936.

CHAPTER FOUR

FACILE SYNTHESIS OF BIFUNCTIONAL Co_xS_y NANOPLATES FOR EFFICIENT H_2/O_2 EVOLUTION AND SUPERCAPACITANCE

4.1. Introduction

The crises on the depletion of fossil fuels coupled with an exponential increase in energy demand has motivated researchers in developing efficient, reliable, economical and environmentally-friendly materials for energy storage and energy generation applications[1-3]. As a result, recent efforts include a search for alternative and novel fabrication routes to afford various materials bearing interesting properties suitable for hydrogen evolution and supercapacitors application. Supercapacitors are better used for energy storage devices as compared to conventional batteries, due to their outstanding power density and long cycle life [3-6]. The current use of carbon-based electrodes can provide high power density, however, they exhibit low energy density [7]. On the other hand, transition metal oxides are known to exhibit high energy densities, although cycle life is sacrificed [3].

Water splitting for hydrogen generation is highly desirable as a clean and cheaper source of energy. However, the reaction requires suitable catalysts to overcome high energy barriers necessary for the splitting process [8,9]. Currently, precious metals such as platinum and gold are highly efficient and durable catalysts. However, cost-effective and widely accessible materials are required for widespread applications. Hence, cheaper, earth-abundant and durable materials have been identified for both energy generation and/or energy storage devices.

Recently, the potential of transition metal sulfides (TMS) have been explored for energy applications, such as supercapacitors, fuel cells, and batteries [10-13]. Cobalt sulfide is an important member of TMS and a potential candidate for energy applications [14-16]. The cobalt sulfide system is however complex, due to phase diversity related to stoichiometric ratios such as CoS, CoS_2, Co_2S_3, Co_3S_4, Co_9S_8, and $Co_{1-x}S$ [17]. Nonetheless, the high redox activity of cobalt sulfide is responsible for the enhanced electrochemical capacitance performance. Likewise, it also effectively catalyzes the redox electrolytes in dye-sensitized solar cells (DSSCs), an indication of suitable replacement for highly expensive Pt counter electrodes. Thus, this efficient performance makes cobalt sulfide a promising system for energy applications [18]. Xing *et al*. used hydrothermally-synthesized CoS_2 nanocrystallites for supercapacitor applications; specific capacitance of 237 F/g at 1 A/g was obtained [19]. The material showed high stability, as well as 7.4 % of specific capacitance was lost over 2000 cycles. In another example, CoS nanocrystals synthesized by a simple bio-molecule-assisted hydrothermal method, showed stable capacitance

of 363 F/g with a loss of only 13 %, even after an increase of scan rate by 10-fold [20]. Examples of cobalt sulfide nanocomposites have been made, such as titania-CoS nanocomposites which have showed high specific capacitance of 370 F/g and excellent cycle stability in KOH electrolyte [21].

Different synthetic methods have been used for the fabrication of cobalt sulfide nanomaterials. However, only a few literature reports have demonstrated the incorporation of single source precursors, as opposed to the traditional multiple source precursor routes. The use of single source precursors is often advantageous and desirable because of the presence of preformed bonds between metal and the chalcogen atom; they are mainly metal-organic compounds [22-26]. Of the few examples is *Bis(*diethyldithiocarbamato)cobalt(II) complex which has been used as a single source precursor to deposit CoS thin films by the drop-casting method followed by thermal treatment [27]. The films were subsequently used as counter electrodes in dye-sensitized solar cells. *Tris*(methyl-n-hexyldithiocarbamato)cobalt(III) complex was used by O'Brien *et al*.[28] to deposit $Co_{1-x}S$, CoS_2, and Co_3S_4 thin films by the AACVD method. NiAs-type hexagonal $Co_{1-x}S$ thin films have been deposited by AACVD using thio- and dithiobiuret complexes of cobalt; nanoparticles of the $Co_{1-x}S$ and Co_4S_3 phases are obtained from the same complex, depending on reaction conditions [29, 30]. The solvent-mediated thermolysis of *di*-*t*-butyldithiophosphinatocobalt(II) complex in tri-*n*-octylphosphineoxide (TOPO) and hexadecylamine (HDA) has yielded cubic Co_9S_8 nanoparticles [31].

In this chapter, synthesis of the novel complex, [*tris*(morpholinodithiocarbamato)cobalt(III)] (**4**), and elucidation of its single-crystal X-ray structure, is reported. The complex was then used as a single source precursor to prepare cobalt sulfide nanoplates by the hot injection method at three different temperatures. The synthesized nanoplates at two selected temperatures, 230 °C and 260 °C, have been evaluated for H_2/O_2 evolution reaction and supercapacitance activities. The study indicates that cobalt sulfide is an efficient bifunctional material for energy applications.

4.2. Experimental details

4.2.1. Materials

Morpholine, carbon disulfide, cobalt chloride hexahydrate, oleylamine (OLA), sodium hydroxide (99%), methanol (99.5%), chloroform, acetone and hexane were used as purchased (Sigma Aldrich) without any further purification.

4.2.2. Synthesis of ligand and cobalt complex

The synthesis of morpholino-dithiocarbamate ligand was performed using the procedure reported by Gervas *et al.* [32].

The Co(III) complex was synthesized by a slow addition of a 25 mL aqueous solution of $CoCl_2 \cdot 6H_2O$ (2.25 g, 9.43 mmol) to a 30 mL aqueous solution of the ligand (18.86 mmol) at room temperature. The resulting reaction mixture was stirred vigorously for 45 min. The precipitate, [*tris*(morpholinodithiocarbamato)cobalt(III)] (**4**), was separated by vacuum filtration, washed with copious amount of deionized water and dried in a vacuum desiccator at 80 °C overnight. Yield: 91%. Microanalysis: Calculated for $C_{15}H_{24}CoN_3O_3S_6$: C, 33.02; H, 4.43; N, 7.70. Found: C, 33.54.11; H, 4.62; N, 7.93. IR (cm^{-1}, ATR): 975, *v* (C═S); 1417, *v* (C═N); 1623, *v*(C-N); 471, *v* (Co–S).

4.2.3. Synthesis of Co_xS_y nanoparticles

In a typical procedure, 200 mg of the complex was uniformly dispersed in 2.0 mL of oleylamine (OLA) by sonication and injected into preheated OLA (6.0 mL) in a three-necked flask at the desired temperature of 190 °C, 230 °C or 260 °C. The temperature would momentarily drop by 10-15 °C upon injection with the solution immediately turning black. The reaction temperature was maintained for 2 hours, after which the heating was stopped. A 30.0 mL mixture of methanol and acetone (v/v 1:1) was used for precipitation of OLA-capped Co_xS_y nanoparticles, which were then further washed with the same solvent mixture and separated by centrifugation. The supernatant was discarded and the dried solids (nanoparticles) were used for further characterization.

4.2.4. Characterization techniques

Other characterization techniques used in this work are detailed in chapter 2 of this thesis.

4.2.4.1. Electrochemical studies for supercapacitance application

Electrochemical characterizations of the samples were performed using the three-electrode system. Working electrodes were prepared by coating a mixture of Co_xS_y (80 wt.%), acetylene black (10 wt.%), and polyvinylidene difluoride (10 wt.%) in N-methyl pyrrolidinone (NMP) on to a nickel foam. A platinum wire and saturated calomel electrode were used as a counter and a reference electrode in 3M KOH as an electrolyte. A supercapacitor device was fabricated using two working electrodes separated by ion transporting layer. The size of the device was 0.25 cm^2. Before assembling the device, both working electrodes and ion-transporting layer were soaked in the 3 M KOH for 1 hr. Versa STAT 4-500 electrochemical workstation (Princeton Applied Research, USA) was used to perform cyclic voltammetry, galvanostatic charge-discharge, and electrochemical impedance spectroscopy (EIS) measurements. EIS measurements were carried out by applying an AC voltage with 10 mV amplitude in a frequency range from 0.05 Hz to 10 kHz at open circuit potential.

4.2.4.2. Electrocatalytic studies for H_2/O_2 evolution studies

Electrocatalytic behavior of the Co_xS_y samples, for catalytic activities for Oxygen and hydrogen evolution studies, was also examined using standard three electrode system consisting of samples on nickel foam as a working electrode, platinum wire as a counter electrode and saturated calomel electrode (SCE) as a reference in 1M KOH electrolyte. Electrocatalytic testing included linear sweep voltammetry (LSV), cyclic voltammetry (CV), chronoamperometry and electrochemical impedance spectroscopy (EIS). LSV was performed at a scan rate of 1 mV/s in both OER and HER region. The potential was converted to RHE using the Nernst equation. All the ElS measurements were recorded in a frequency range of 0.05 Hz to 10 kHz with an applied 10 mV of AC amplitude.

4.3. Results and discussion

4.3.1 Cobalt complex and thermogravimetric analyses

The complex (**4**) was synthesized by the simple metathetical reaction. It was observed that the Co^{2+} in the metal salt was oxidized *in-situ* during the reaction to Co^{3+} in the final complex (**4**). This *in-situ* oxidation phenomenon of cobalt is well reported in literature [33]. The phenomenon, however, has no adverse effect on the stability of the complex in its solid state at lower temperatures as demonstrated by thermogravimetric analysis (TGA). The complex (**4**) shows high thermal stability up to 300 °C, after which a sharp single-step decomposition was observed (Figure 4.1). A major mass loss of 77 % was observed, attributed to the evolution of volatile organic components. The residue corresponds to the formation of CoS_2 phase (*ca*. 22 %).

The synthesis of nanoparticles was easily carried out in oleylamine (OLA), even at 200 °C, lower than the decomposition temperature of complex (**4**). The strong nucleophilic character of the amine group in OLA is primarily responsible for initiating the decomposition of the complex at low temperatures [22]. Furthermore, previous reports indicate that primary amines substitute the secondary amine of the dithiocarbamates, which causes the breakdown of the molecular precursors [34, 35]. The use of OLA also has an advantage of effectively capping the nanoparticles due to the long alkyl chain [36].

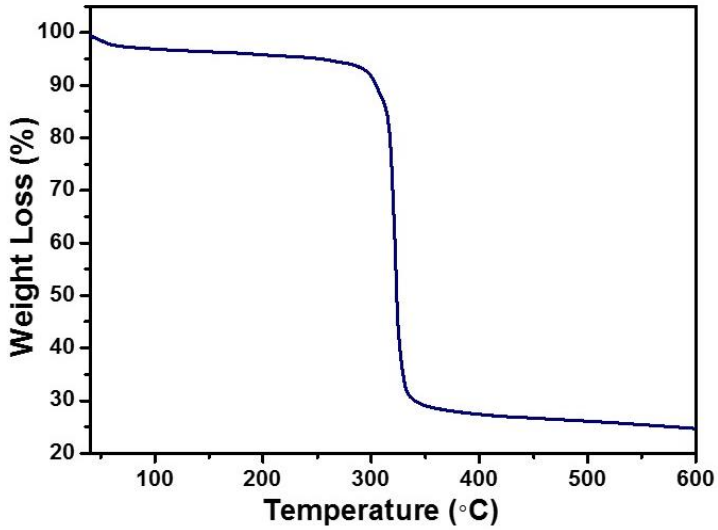

Figure 4.1: Thermogravimetric curve for $[Co(Mordtc)_3]$ complex (**4**).

4.3.2 Single crystal X-ray crystallography structure for complex (4)

The complex [tris(morpholinodithiocarbamato)Co(III)] (**4**) was analysed by single crystal X-ray diffraction; crystal and structure refinement data are given in Table 4.1. The solid-state structure shows that the asymmetric unit comprises two metal chelate molecules and a single methylene chloride solvent molecule. Each metal chelate could thus be described as a hemi-solvate. The present structure represents a new polymorph of a compound previously studied by X-ray diffraction experiments [37]. A search of the Cambridge Structural Database (CSD) [37] shows three previously reported polymorphs of the compound. The CSD reference codes are IHAROY (*P*-1, CH_3CN monosolvate), MCDTCO (*C*2/*c*, benzene monosolvate) and MRDTCO (*P*-1, CH_2Cl_2 monosolvate). The previously reported compounds all have a single chelate molecule in the asymmetric unit associated with various solvent molecules [38-40]. It is interesting to note that the present structure bucks the trend in that the asymmetric unit comprises two independent molecules with each a different enantiomer, i.e. lambda and delta. The mirror symmetry of the two molecules is illustrated in Figure 4.2, in which each of the molecules has been individually rotated to highlight their approximate mirror symmetry. In addition to being a new polymorph the present structure also offers a significant improvement in the quality of the X-ray data. As illustrated by data collection at lower temperature, an improved R_{int} and R_1 value as well as an improved C–C bond accuracy. The asymmetric unit of the compound is shown in Figure 4.3.

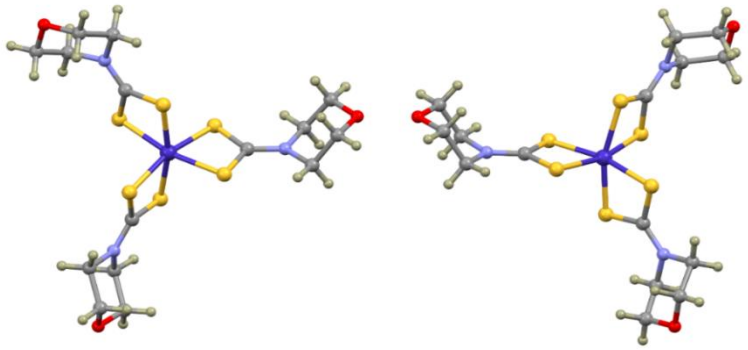

Figure 4.2: Independent manipulation of the molecules comprising the asymmetric unit shows that they are lambda and delta coordination enantiomers. Each of the molecules exhibits approximate D3 symmetry, though all the atoms are unique.

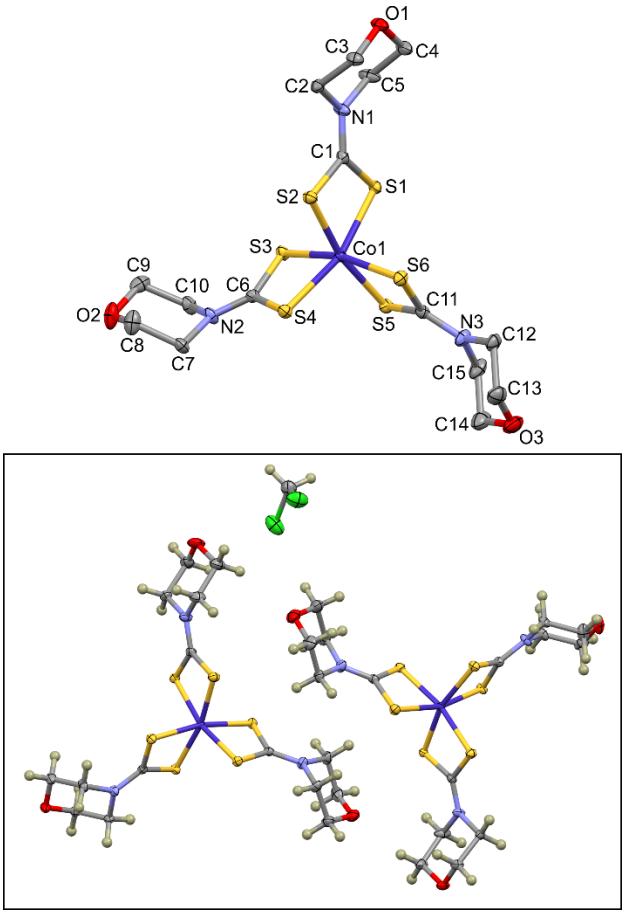

Figure 4.3: [Top] Displacement ellipsoid plot of molecule one of the asymmetric unit indicating the atom numbering scheme. Atoms are rendered at 50% probability; hydrogen atoms are omitted for clarity. [Inset] Asymmetric unit of [tris(morpholinodithiocarbamato)Co(III)] (**4**) showing the two independent molecules as well as the dichloromethane molecule of solvation (CCDC 1570707).

Table 4.1: Crystal structure and structure refinement details for *tris*(morpholinodithiocarbamato)cobalt(III) (**4**).

Crystal Data	**Complex (4)**
Chemical formula	$2(C_{15}H_{24}CoN_3O_3S_6)\cdot CH_2Cl_2$
Molar Mass (g mol^{-1})	1176.25
Crystal system, space group	Triclinic, *P*-1
Temperature (K)	100(2)
a, *b*, *c* (Å)	12.168(1), 15.602(2), 15.814(2)
α, β, γ(°)	118.724(3), 90.984(3), 110.073(3)
V (Å^3)	2411.7(4)
Z	2
Radiation type	Mo*K*α
μ (mm^{-1})	1.37
Crystal size (mm)	0.42 × 0.29 × 0.21
Data collection	
Diffractometer	Bruker Apex Duo CCD diffractometer
Absorption correction	Multi-scan, *SADABS*, Bruker 2014
T_{min}, T_{max}	0.671, 0.746
No. of Measured, independent and observed [$I > 2\sigma(I)$] reflections	53897, 14314, 13120
R_{int}	0.029
Refinement	
$R[F^2 > 2\sigma(F^2)]$, $wR(F^2)$, S	0.025, 0.063, 1.03
No. of reflections	14314
No. of parameters	532
No. of restraints	0
H-atom treatment	H-atom parameters constrained.
$\Delta\rho_{max}$, $\Delta\rho_{min}$ (e Å^{-3})	1.04, –0.83

Each of the two metal structures in the asymmetric unit adopts an approximately octahedral coordination geometry with the cobalt(III) metal centre coordinated by three monoanionic dithiocarbamate-derived ligands. The bond parameters describing the metal centre are summarised in Table 4. 2.

Table 4.2: Selected bond parameters describing the coordination sphere of the cobalt(III) metal centre in molecules one and two of the asymmetric unit.

Bond	Length (Å)	Bond	Angle (°)
Co1–S1	2.2712(5)	S1–Co1–S4	163.12(2)
Co1–S2	2.2630(5)	S2–Co1–S5	167.33(2)
Co1–S3	2.2500(4)	S3–Co1–S6	165.61(2)
Co1–S4	2.2878(6)	S1–Co1–S2	76.50(2)
Co1–S5	2.2613(5)	S3–Co1–S4	76.81(1)
Co1–S6	2.2827(4)	S5–Co1–S6	76.40(1)
Co2–S7	2.2522(6)	S7–Co2–S10	168.12(2)
Co2–S8	2.2840(5)	S8–Co2–S11	166.10(2)
Co2–S9	2.2675(4)	S9–Co2–S12	167.89(2)
Co2–S10	2.2630(6)	S7–Co2–S8	76.63(2)
Co2–S11	2.2589(5)	S9–Co2–S10	76.80(1)
Co2–S12	2.2741(4)	S11–Co2–S12	76.77(1)

The data in Table 4.2 highlight the constrained coordination geometry imposed by the four-membered coordination sphere. The small bite of the ligand leads to a significantly acute intraligand S–Co–S angle: *ca.* 76.5°. An additional consequence of this small ligand bite is that the trans interligand S–Co–S bond angles are constrained to approximately 167°; significantly less than the optimum of 180°. The result is a somewhat distorted octahedron. The Co–S bond lengths are all comparable, having an average distance of 2.268 Å with a standard deviation of 0.012 Å. These data are consistent with the notion that there is delocalisation of electrons over the dithiocarbamate group. Localisation of the formal negative charge of the ligand on one of the sulfur atoms would yield two different bond lengths corresponding to the difference in

electrostatic attraction between the ligand donor atoms and metal centre. The proposed delocalisation of electrons is further supported by the similarity of the C–S bond lengths which average 1.712 Å with a standard deviation of only 0.006 Å for the twelve bonds. A Mogul structural search shows that the Co–S bond lengths compare favourably with those of related structures in the CSD, the mean value is reported as 2.27(1) Å. The N-morpholine rings have all adopted a chair configuration, as is typically observed for this class of molecules when coordinated to transition metal ions [39, 41, 42] The mean C–N bond length measures 1.325 Å with a standard deviation of 0.002 Å for the six measured values. This is shorter than a typical C–N single bond and is indicative of significant double bond character as a consequence of electron delocalisation.

The structure contains solvent accessible voids which account for 6.2% of the unit cell volume (149 Å) (Figure 4.4). This was calculated using a probe radius of 1.2 Å using Mercury 3.10.2. In the present structure these voids are occupied by well-ordered dichloromethane molecules. These voids do not represent open channels in the lattice, but are cavities formed during crystallisation. Since the voids are closed the crystals with the volatile dichloromethane solvent are stable for several weeks under ambient conditions.

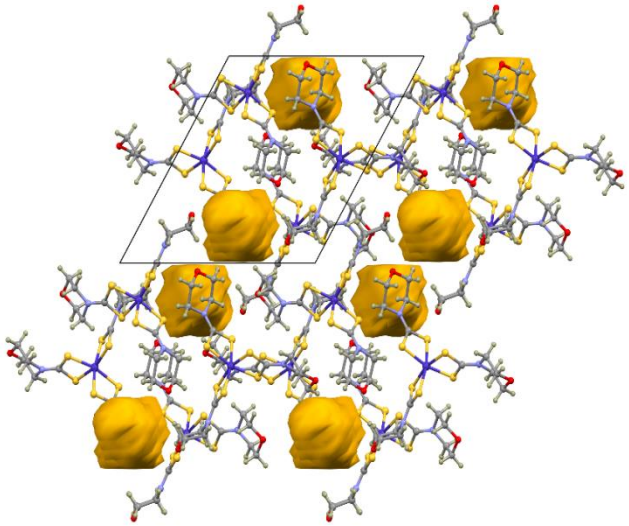

Figure 4.4: Voids (shown as yellow surfaces) in the lattice of tris(morpholinodithiocarbamato)Co(III)] (**4**). In the present structure these voids are occupied by dichloromethane molecules. The lattice is shown viewed down the *c*-axis.

Analysis of the three-dimensional structure indicates several stabilising C–H···O and C–H···S intermolecular interactions. The significance of these interactions was adjudicated by comparison of their length with the sum of the van der Waals radii of the interacting atoms. The geometric parameters of the intermolecular interaction are summarised in Table 4. 3. Assuming an approximate correlation between the interaction distances and their relative strengths, the C–H···O interactions old considered moderately strong being *ca*. 0.4 Å shorter than the sum of the radii of the interacting atoms. Application of the same reasoning would suggest the C–H···S interactions are weaker. This is understandable if interactions of this nature are to be considered on electrostatic grounds.

Table 4.3: Geometric parameters of the intermolecular interactions.

Bond	D–H (Å)	H···A (Å)	D···A (Å)	Length – vdW*	D–H···A (°)
C4–H4A···O6	0.990	2.326	3.209(2)	-0.394	148.1
C29–H29B···O2^{i}	0.990	2.285	3.271(3)	-0.435	174.1
C9–H9A···O4^{ii}	0.991	2.292	3.268(3)	-0.428	168.4
C2–H2A···S11^{iii}	0.990	2.896	3.622(1)	-0.104	130.9
C3–H3A···S7^{iii}	0.990	2.676	3.607(2)	-0.324	156.7
C5–H5B···S10^{iv}	0.990	2.836	3.716(2)	-0.164	148.4
C24–H24B···S3^{iv}	0.989	2.827	3.778(2)	-0.173	161.4
C28–H28B···S10^{iv}	0.989	2.796	3.738(1)	-0.204	159.3

*interaction distance subtracted by the sum of the van der Waals radii of the interacting atoms.

Symmetry codes: (i) x, 1+y, z; (ii) x, 1+y, 1+z; (iii) –x, 1-y, 1-z; (iv) 1-x, 1-y, 1-z

4.3.3. Phase Purity and morphology analyses

The choice of performing the synthesis of the nanoparticles at three different temperatures aimed at establishing a thermal influence on morphology phase. The morphology of the synthesized nanoparticles was observed by transmission electron microscopy (TEM). At 230 °C, the crystallites showed the hexagonal faceted discotic-like structures, whereas cubic or plate-like structures with truncated edges were obtained at a higher temperature of 260 °C (Figure 4.5). Furthermore, the crystallites sizes increase with temperature. The higher temperature increases the rate of the decomposition of the precursor and also weakens the capping effect of the OLA, rendering it less effective. Similarly, the increased growth and thermodynamic aspects result in increased size and obtained morphology.

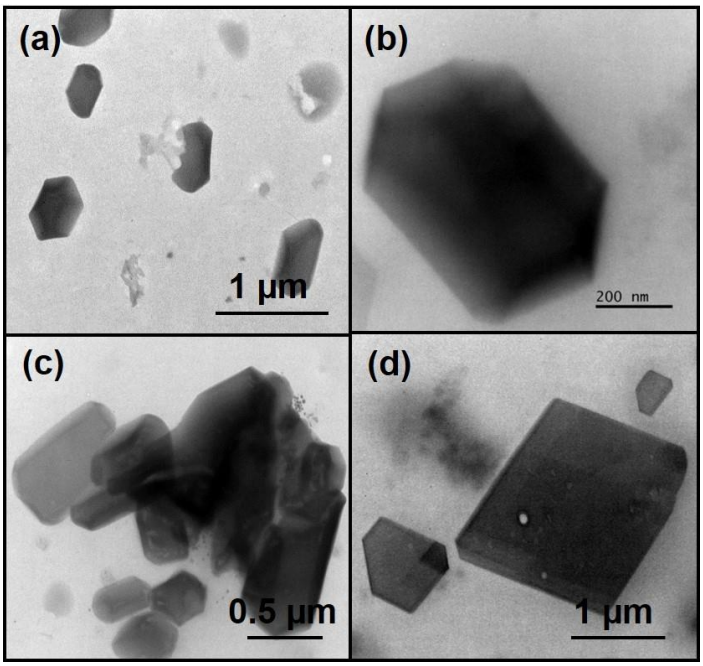

Figure 4.5: TEM images of OLA-capped Co_xS_y platelets synthesized at (a-b) 230 °C (c-d) 260 °C.

The nanoparticles were characterized by powder X-ray crystallography (p-XRD) to determine the phase purity; however, the cobalt-rich samples generally fluoresce strongly under CuKα radiation. The energy of the Kα radiation of copper is higher than the k-absorption edge of cobalt; hence, cobalt fluoresces strongly and give rise to the noisy and inconclusive diffraction pattern. For the same reason, fluorescence was dominant in both samples and peaks were not very prominent due to the noisy background especial at lower temperature of 190 °C (Figure 4.6 a). The increase in temperature generally enhances the crystallinity, which was shown by the comparatively pronounced peaks for the nanoparticles prepared at 260 °C (Figure 4.6 c). A close examination of the peaks agreed with a mixture of the linnaeite (Co_3S_4) (ICDD #00-047-1738) as a major phase identified with intense peaks and minor peaks for cattierite (CoS_2) (ICDD #01-089-3056) phase as an impurity.

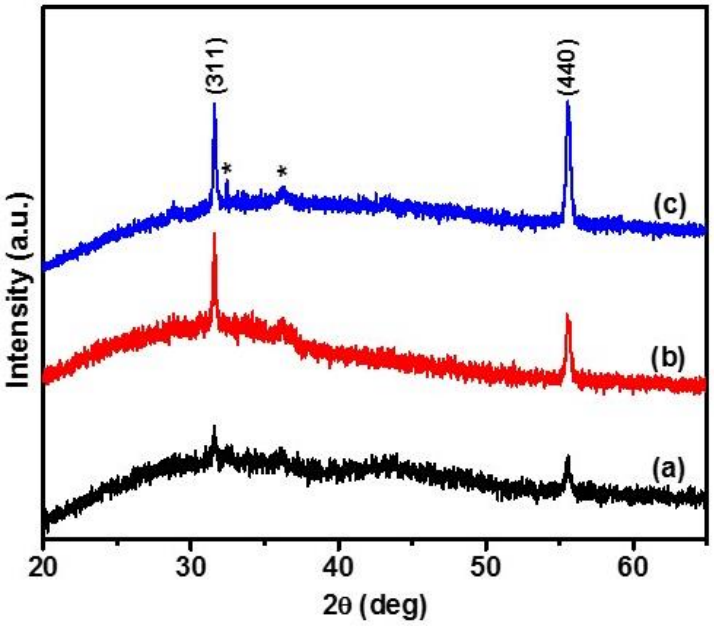

Figure 4.6: p-XRD micrograph for the nanoparticles prepared at various temperatures a) 190 °C, b) 230 °C and c) 260 °C.

4.3.5 OER/HER electrocatalyst studies

The activity of Co_xS_y samples was studied as OER electrocatalyst in 1.0 M KOH electrolyte using linear sweep voltammetry (LSV). The polarization curves for Co_xS_y samples in OER potential range are given in Figure 4.7 a. For simplicity, nanoparticles prepared at 230 °C and 260 °C are referred to as **CoS-1** and **CoS-2**, respectively. It can be clearly observed that **CoS-2** had a lower overpotential (276 mV) to generate a current density of 10 mA/cm^2 than **CoS-1** (307 mV). The Tafel slopes were further used to measure the OER kinetics of Co_xS_y samples. From the Figure 4.7 (b), **CoS-1** and **CoS-2** showed the Tafel slopes of 96 and 82 mV/dec, respectively. The lower Tafel slope of **CoS-2** suggested faster electron transfer and OER kinetics, which conformed to the lower overpotential and better electrocatalyst performance compared to **CoS-1**. From the observation of OER performance, Co_xS_y materials prepared in this work exhibit relatively higher catalytic efficiency compared to other Co_xS_y-based OER catalysts reported in literature. Zhao and co-workers fabricated nanoporous, hollow Co_3S_4 nanosheets through the anion exchange reaction of $Co(OH)_2$ nanosheets with S^{-2} ions as an oxygen evolution anode in alkaline media. This Co_3S_4 electrode required an overpotential of 363 mV to generate a

current density of 10 mA/cm^2 with a Tafel slope of 90 mV/dec.[4] The cobalt sulfide/nitride (or co-doped) - porous carbon core-shell nanocomposites synthesized by Chen *et al*.[5] by a facile one-step sulfurization and carbonization of ZIF-67 showed an overpotential of 0.47 V for 10 mA cm^{-2} current density. The comparison with recently reported OER Co-based catalysts is given in Table 4.4.

Electrochemical impedance spectroscopy (EIS) measurements were used to study the electrocatalytic properties. Figure 4.7 c and Figure 4.7 e showed the Nyquist plots (Z_{real} vs Z_{img}) of **CoS-1** and **CoS-2** at various potentials, respectively. It was clear that for both Co_xS_y samples, the curves from Nyquist plots started to convert to a small semicircle from a straight line with the increase in the potential. This was because the increase in the potential offered faster reaction which leads to the reduction of the smaller radius of semicircle at the low-frequency region, indicating better activity of Co_xS_y electrodes at higher potential. From the further comparison of Nyquist plots of **CoS-1** and **CoS-2** at 0V (at open circuit potential) and 0.45V (vs SCE, most close to the overpotential at 10 mA/cm^2), it can be observed that the **CoS-2** had shorter length at 0V and a smaller diameter of the semicircle at 0.45V, which indicated the lower charge-transport resistance and faster electron transfer rate. This can be further confirmed by the lower total impedance IZI as a function of the frequency of **CoS-2** than CoS-1 from Figure 4.7 d and Figure 4.7 f. Therefore, the better conductive property and faster electron transfer of **CoS-2** obtained from EIS measurements suggested an improved electrocatalytic performance which is consistent with the better OER activity.

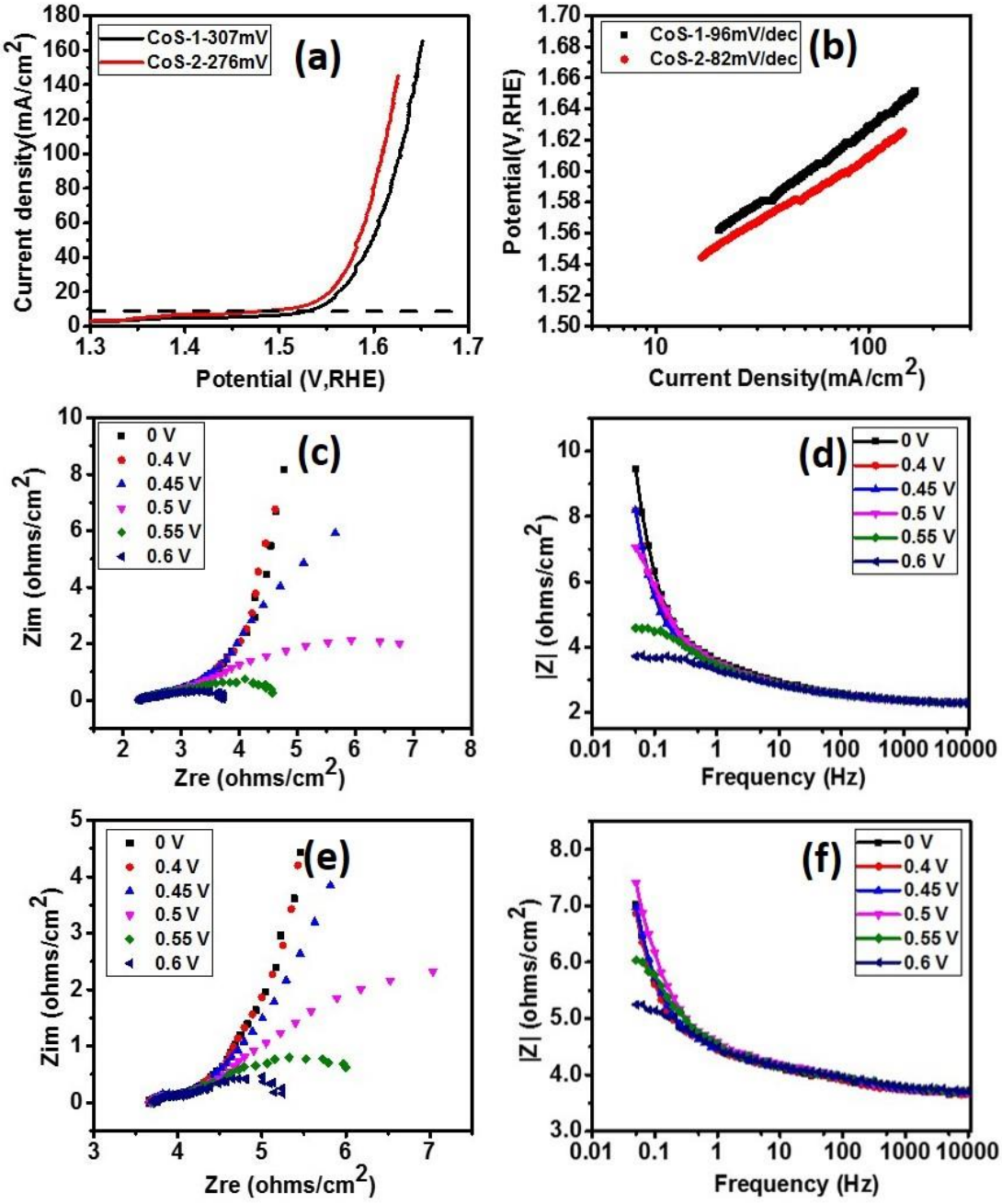

Figure 4.7: (a) Polarization curves and (b) Tafel slopes for **CoS-1** and **CoS-2** samples in OER range. (c) Nyquist plots and (d) IZI vs frequency plots for CoS-1 at various OER over potentials. (e) Nyquist plots and (f) IZI vs frequency plots for CoS-2 at various OER over potentials.

Table 4.4: Comparison of OER performance of some recently reported Co-based electrocatalysts.

Catalyst	Overpotential (mV) at 10 mA/cm^2	Tafel Slope (mV/decade)	Reference
Co_3O_4	410	110	[6]
Co_3O_4/$NiCo_2O_4$	340	88	[6]
Co_3O_4	356	68	[7]
CoP/C	360	66	[8]
CoP	290	65	[9]
Co0.5Fe0.5S@N-MC	410	159	[10]
N-Co9S8	548	241	[11]
Co9S8/Graphene	441	94	[11]
N-Co9S8/Graphene	409	83	[11]
CoS/Ti mesh	361	64	[12]
CP/Co-S	363	101	[13]
CP/CTs/Co-S	306	72	[13]
Bulk CoS2	290	160	[14]
A-CoS4.6O0.6PNCs	300	67	[14]
Co9S8 /CNFs	512	78	[15]
Co9S8@MoS2 /CNFs	430	61	[15]
Co9S8(600)/N,S-GO	400	96	[16]
CoS2(500)/N,S-GO	390	80	[16]
CoS2(400)/N,S-GO	380	75	[16]
CoS-1	307	96	**This work**
CoS-2	276	82	**This work**

Chronoamperometry, linear sweep voltammetry, and EIS measurements were used to evaluate the long-term durability of Co_xS_y electrodes. As seen in Figure 4.8 a, both samples showed a constant current density for over 16 hours, indicating the stable behavior of little negative effect on current density with increasing time. Figure 4.8 b displayed the LSV polarization curves of the **CoS-2** at various cycles. There was a very small difference (2 mV at 10 mA/cm^2) in overpotential after 2,000 cycles of polarization measurements. Moreover, the almost completely overlapping Nyquist plots at 0V and 0.5V after 1st, 1000th and 2000th polarization measurement further confirmed the excellent durability of **CoS-2** sample (Figure 4.8 c and Figure 4.8 d).

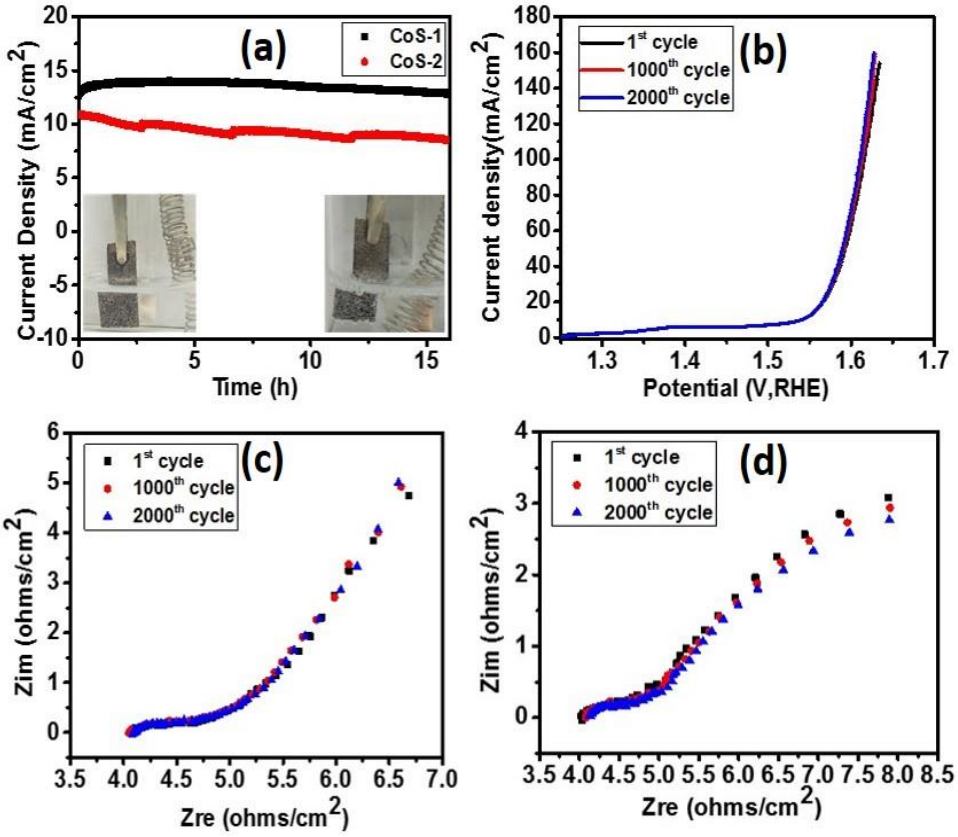

Figure 4.8: Durability test of Co_xS_y electrocatalyst for OER using (a) chronoamperometry (inset figure shows oxygen evolution during this experiment from **CoS-1** and **CoS-2** electrode), (b) linear sweep voltammetry, Nyquist plots at (c) 0V and (d) 0.5V of **CoS-2**.

The HER electrocatalytic performance of Co_xS_y samples was also investigated. The polarization curves of **CoS-1** and **CoS-2** in HER potential range were given in Figure 4.9 a. As seen, the **CoS-1** and **CoS-2** showed similar activities with almost overlapping polarization curves and very close overpotential at 10 mA/cm^2. It can be further observed from the Figure 4.9 b that **CoS-1** and **CoS-2** display similar Tafel slopes of 159 and 154 mV/dec. A relatively lower Tafel slope for **CoS-2** suggested superior HER catalytic kinetics. The 3-dimensional graphene/cobalt sulfide nanoflake composite was prepared by Wang *et al*.[17] as hydrogen evolution catalysts, which need an overpotential about 320 mV to reach 10 mA/cm^2. Zhu *et al*.[15] reported a cubic cobalt sulfide–layered molybdenum disulfide core-shell/carbon nanofibers showing excellent electrocatalytic activities with an overpotential of 190mV. Table 4.5 displays the comparison of Co_xS_y samples synthesized in this work with other recently reported Co-based HER catalysts in the alkaline medium.

The Nyquist plots at various HER overpotentials of **CoS-1** (Figure 4.9 c) and **CoS-2** (Figure 4.9 e) showed the same phenomenon with the Nyquist plots at OER overpotentials, the curves becoming semicircles from straight lines and the radius of semicircles decreasing. This phenomenon was consistent with the reduction of total impedance IZI with the increase of negative potential for both Co_xS_y samples in Figure 4.9 d and Figure 4.9 f, indicating lower charge transfer resistance.

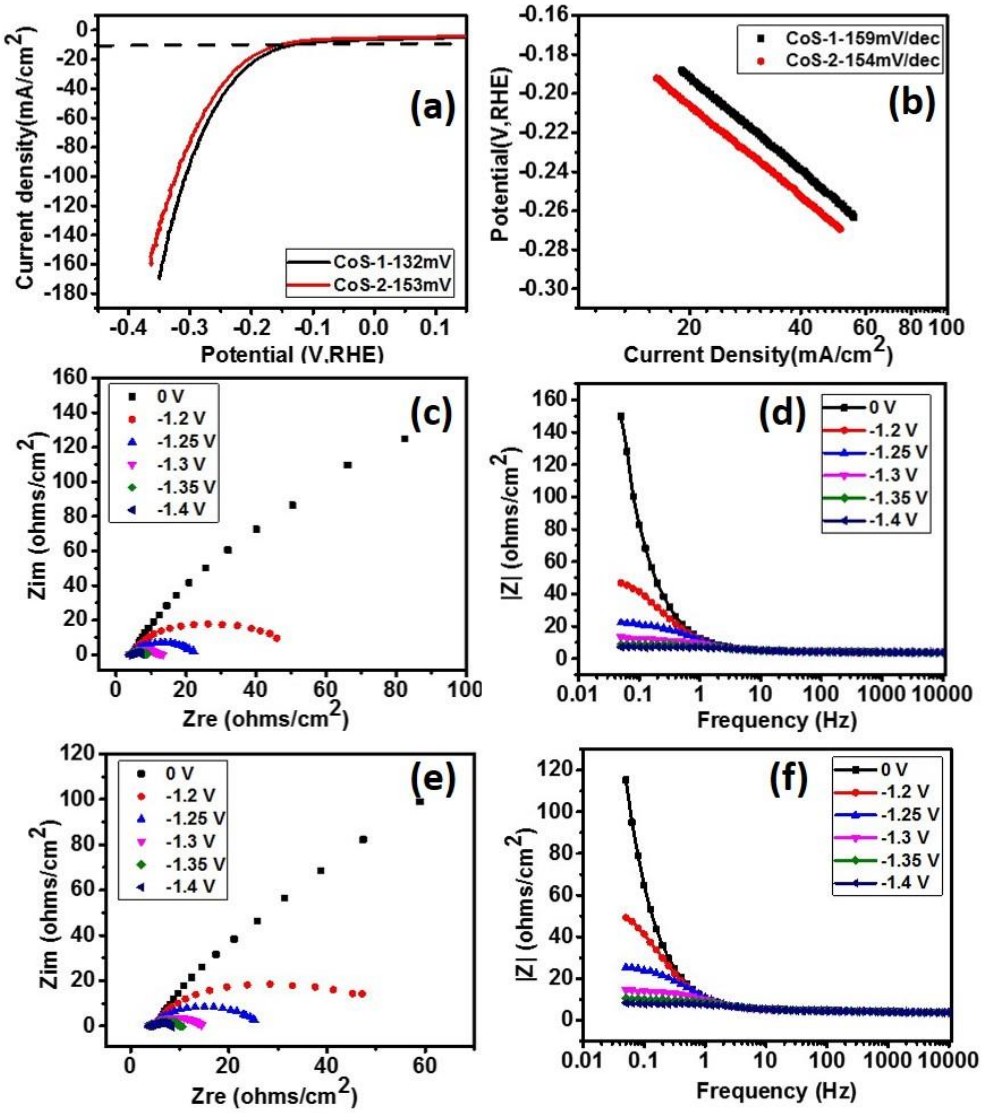

Figure 4.9: (a) Polarization curves and (b) Tafel slopes for **CoS-1** and **CoS-2** samples in HER range. (c) Nyquist plots and (d) IZI vs frequency plots for **CoS-1** at various HER overpotentials. (e) Nyquist plots and (f) IZI vs frequency plots for **CoS-2** at various HER overpotentials.

Table 4.5: Comparison of HER performance of some recently reported Co-based electrocatalysts in alkaline medium.

Catalyst	Overpotential (mV) at 10 mA/cm^2	Tafel Slope (mV/decade)	Reference
CoO_x@CN	~220	115	[18]
Porous N-C/Co NP	298	131	[19]
Co@N-C	210	108	[20]
EG/$Co_{0.85}Se$	~320	223	[21]
EG/$Co_{0.85}Se$/NiFe-LDH	260	160	[21]
Zn-Co-S Nanosheets	415	139	[22]
Zn-Co-S Nanoplates	304	131	[22]
Zn-Co-S Nanoneedles	234	109	[22]
CP/Co-S	357	138	[13]
CP/CTs/Co-S	190	131	[13]
Co_9S_8@C	250	-	[23]
CoS_2	244	133	[24]
CoS-1	132	159	**This work**
CoS-2	153	154	**This work**

Note: References are attached at the end of the chapter as Appendix 4.1

The electrochemical double layer capacitance (Cdl) was used to study the electrochemically-active surface area of Co_xS_y samples by plotting half of the difference in positive and negative current densities of the cyclic voltammogram curves in the non-faradaic region (potential range 0.87-0.92V vs. RHE) at various scan rates (Figure 4.10). The Cdl of **CoS-2** was calculated to be 8.2 mC/cm^2, which was more than double that of **CoS-1** (3.5 mC/cm^2). The much higher Cdl of **CoS-2** suggested a larger effective electrochemical surface area to provide electron transfer and H_2/O_2 evolution reactions.

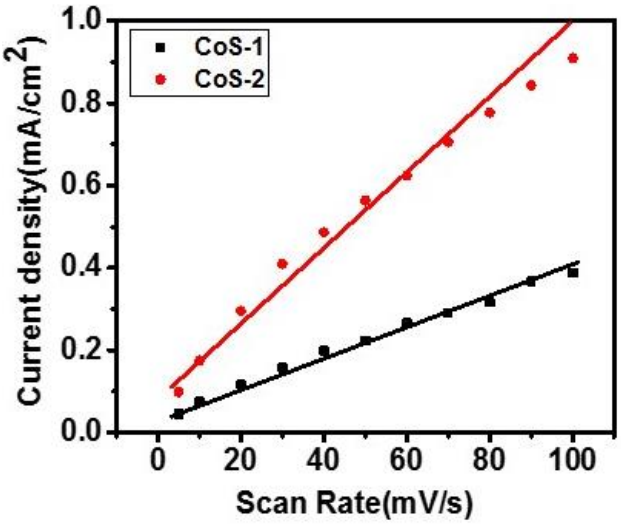

Figure 4.10: The electrochemical double layer capacitance (Cdl).

4.3.6. Supercapacitor performances studies

The supercapacitor performances of Co_xS_y samples were also studied in a 3M KOH solution. The galvanostatic charge-discharge curves of **CoS-1** and **CoS-2** at various current densities are given in Figures 4.11 a and d, respectively. A clear set of non-linear curves suggested typical pseudocapacitance behaviors attributed to Faradaic redox reactions at the Co_xS_y samples surface.

Both samples need adequate time to complete a charge-discharge cycle, with the decrease of current density. Of most significance, **CoS-2** displayed longer charge and discharge time than **CoS-1** at the same current density, instigating relatively larger charge storage capacity. From the cyclic voltammograms of Co_xS_y samples (Figure 4.11 b and e), it can be observed that occurrence of redox peaks furtherly suggested reversible redox reactions. The peak current density increased and the potential difference between the oxidation reaction and reduction reaction expanded gradually with increasing the scan rate.

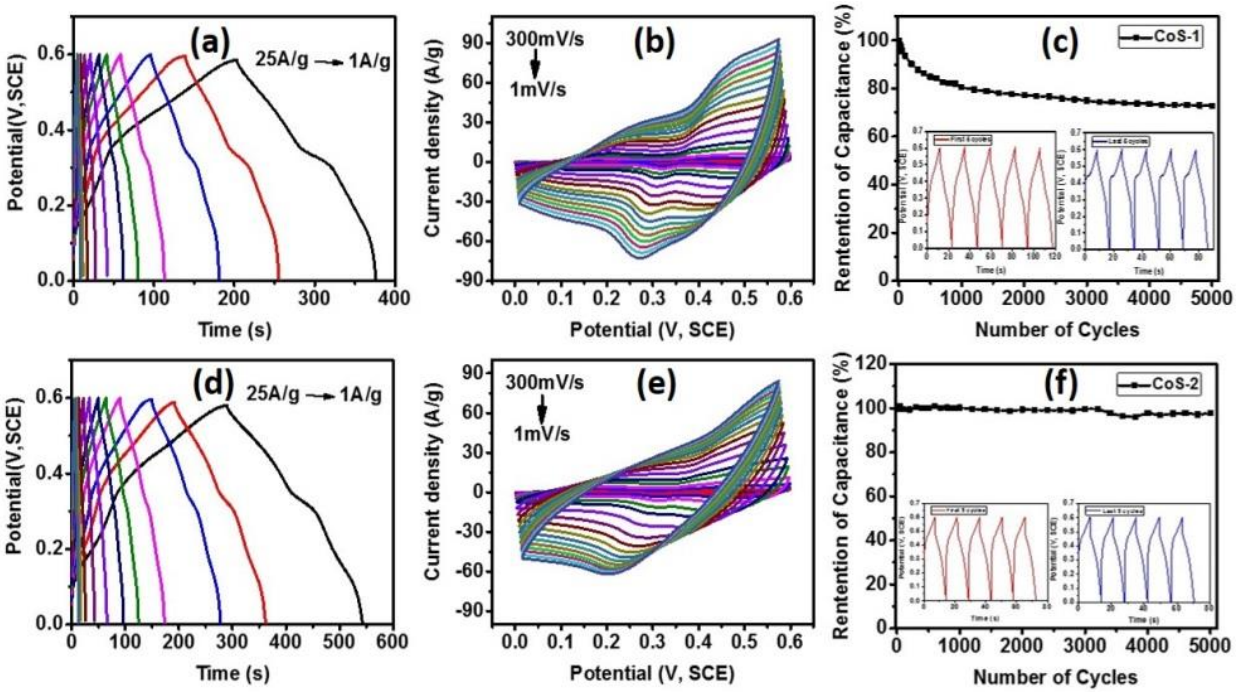

Figure 4.11: Galvanostatic charge-discharge curves of (a) **CoS-1** and (d) **CoS-2** at various current densities in 3M KOH electrolyte. CV curves of (b) **CoS-1** and (e) **CoS-2** at various scan rates in 3M KOH electrolyte. Cyclic stability plot for (c) **CoS-1** and (f) **CoS-2** sample using galvanostatic charge-discharge measurements (inset figure shows the first and last 5 charge-discharge cycles).

Galvanostatic charge-discharge measurements for 5000 cycles were used to evaluate the long-term supercapacitor performance of Co_xS_y samples. As seen in Figure 4.11 c, the capacitance retention of **CoS-1** showed a drop in the first 1000 cycles, followed by constant retention behaviour. There was a 27 % reduction in the retention of capacitance after 5000 cycles. However, **CoS-2** have an outstanding stable capacitance retention with a 97 % remaining after 5000 cycles with exactly same shapes and similar charging/discharging times of GCD curves compared with the GCD curves of first 5 cycles (Figure 4.11 f). The **CoS-2** sample exhibited the best stability compared to results obtained from other Co_xS_y-based materials in Table 4.6. The ultralong $CoS_{1.097}$ nanotube networks assembled by interlaced nanoflakes synthesized by Liu and co-workers through solvothermal method showed capacity retention of 85 % after 500 cycles. [25 a] And Ghosh *et al.*[25 b] have used a two-step hydrothermal approach to prepare rGO-based hybrid composites with Co_3S_4 grown on Ni foam; the composite

showed a good stability of 96.6 % capacitance remaining over 3000 cycles. Some of the stability results of other Co_xS_y-based samples are provided Table 4.6.

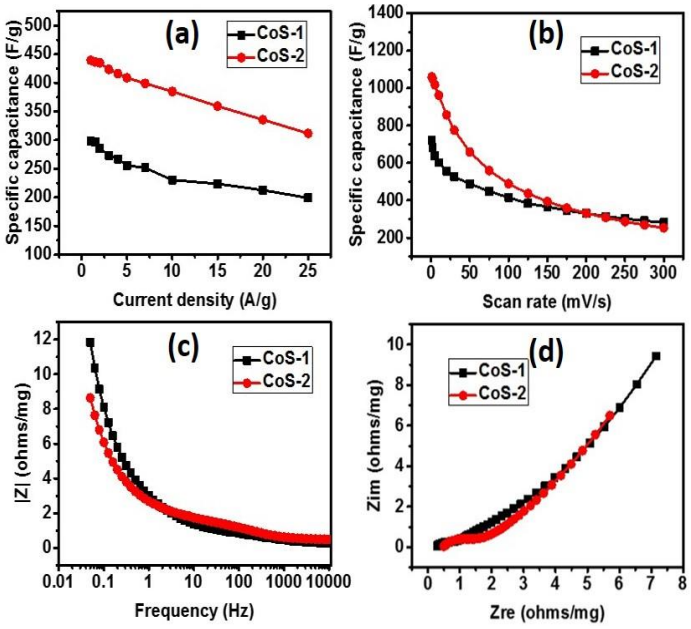

Figure 4.12: Variation of specific capacitance as a function of (a) current density and (b) scan rate for Co_xS_y samples. (c) Z_{real} vs Z_{img} plots and (d) IZI vs frequency plots for Co_xS_y samples in 3M KOH.

Figures 4.12 a and b showed the specific capacitance of Co_xS_y samples calculated from the GCD data and CV data as a function of current densities and scan rates, respectively. It was clear that at a lower scan rate and lower current density, higher specific capacitances were observed, which was attributed to adequate time provided for redox reactions. The maximum specific capacitance for CoS-2 sample is 440 F g^{-1} and 1059 F g^{-1} which were calculated from its GCD and CV curves at a current density of 1 A g^{-1} and a scan rate of 1 mV s^{-1}, respectively. The values are higher than those recorded for the hollow cobalt sulfide hexagonal nanosheets (326 F g^{-1}) [26] and cobalt sulfide nanoparticles (475 F g^{-1}).[27] The lower total impedance IZI, and Z_{real}, Z_{img} of CoS-2 in 3M KOH further indicated the better conductive property, which was consistent to the better supercapacitor performance and the previous results from EIS measurements in 1M KOH (Figure 4.12 c and d).

Table 4.6: Comparison of specific capacitance and stability results of other reported Co_xS_y-based samples.

Samples	Specific capacitance (F/g)	Stability Retention (%)	Reference
ST-CoS	156	~	[28]
Microwave-assisted CoS	224	97% after 1000 cycles	[28]
3D graphene/CoS	443	86% after 5000 cycles	[17]
CoS	~435	62% after 2000 cycles	[29]
CoS/graphene composite hydrogel	564	94.8% after 2000 cycles	[29]
$CoS_{1.097}$	526	57% after 3000 cycles	[30]
CNT@ $CoS_{1.097}$	815	66% after 3000 cycles	[30]
Flower-like CoS	586	91% after 1000 cycles	[31]
TiO2 nanotube/CoS	400	~80% after 1000 cycles	[32]
Cobalt sulfide nanotubes	285	86.5% after 1000 cycles	[33]
CoS-1	298	73% after 5000 cycles	**This work**
CoS-2	440	97% after 5000 cycles	**This work**

Note: References for this table is attached at the end of this chapter as appendix 4.1

4.4. Conclusion

The single source precursor *tris*(morpholinodithiocarbamato)cobalt(III) complex (**4**) has been prepared and fully characterized. It was then used as a single source precursor to synthesize Co_xS_y nanoparticles via an oleylamine-mediated hot injection method. The thermogravimetric analysis and powder X-ray diffraction and thermogravimetric studies showed the formation of cobalt sulfide nanoparticles.

The nanoparticles were then evaluated in energy generation and energy storage studies. CoS-2 sample (260 °C) displayed better electrochemical and electrocatalytic performances than CoS-1 (230 °C). Furthermore, CoS-2 had a lower overpotential (276 mV) to generate a current density of 10 mA/cm^2 than CoS-1 (307 mV), indicative of the superiority of CoS-2 in terms of electrocatalytic performance.

The maximum specific capacitance for CoS-2 sample is 440 F g^{-1} and 1059 F g^{-1} which were calculated from the GCD curve and CV curve of CoS-2 at a current density of 1 A g^{-1} and a scan rate of 1 mV s^{-1}, respectively. These results for CoS-2 showed higher electrochemical performance efficiencies compared to CoS-1 and other Co_xS_y-based materials.

4.5. References

[1] M. Winter and R.J.Brodd, Chem. Rev. 104 (2004) 4245–4269.

[2] K. Ramasamy, R. K. Gupta, S. Palchoudhury, S. Ivanov and A. Gupta, *Chemistry of Materials*, 2014, **27**, 379-386.

[3] G. Wang, L. Zhang and J. Zhang, *Chemical Society Reviews*, 2012, **41**, 797-828.

[4] F. Zhao, Y. Wang, X. Xu, Y. Liu, R. Song, G. Lu and Y. Li, *ACS applied materials & interfaces*, 2014, **6**, 11007-11012.

[5] B. Conway, V. Birss and J. Wojtowicz, *Journal of Power Sources*, 1997, **66**, 1-14.

[6] E. Mitchell, A. Jimenez, R. K. Gupta, B. K. Gupta, K. Ramasamy, M. Shahabuddin and S. R. Mishra, *New Journal of Chemistry*, 2015, **39**, 2181-2187.

[7] Y. Zhang, H. Feng, X. Wu, L. Wang, A. Zhang, T. Xia, H. Dong, X. Li and L. Zhang, *International journal of hydrogen energy*, 2009, **34**, 4889-4899.

[8] P. Xiao, M. A. Sk, L. Thia, X. Ge, R. J. Lim, J.-Y. Wang, K. H. Lim and X. Wang, *Energy & Environmental Science*, 2014, **7**, 2624-2629.

[9] J. Deng, P. Ren, D. Deng, L. Yu, F. Yang and X. Bao, *Energy & Environmental Science*, 2014, **7**, 1919-1923.

[10] M.-R. Gao, J.-X. Liang, Y.-R. Zheng, Y.-F. Xu, J. Jiang, Q. Gao, J. Li and S.-H. Yu, *Nature communications*, 2015, **6**, 5982.

[11] D. Voiry, H. Yamaguchi, J. Li, R. Silva, D. C. Alves, T. Fujita, M. Chen, T. Asefa, V. B. Shenoy and G. Eda, *Nature materials*, 2013, **12**, 850.

[12] L. Cao, S. Yang, W. Gao, Z. Liu, Y. Gong, L. Ma, G. Shi, S. Lei, Y. Zhang and S. Zhang, *Small*, 2013, **9**, 2905-2910.

[13] H. Yu, C. Zhu, K. Zhang, Y. Chen, C. Li, P. Gao, P. Yang and Q. Ouyang, *Journal of Materials Chemistry A*, 2014, **2**, 4551-4557.

[14] K.-J. Huang, J.-Z. Zhang, G.-W. Shi and Y.-M. Liu, *Materials Letters*, 2014, **131**, 45-48.

[15] F. Tao, Y.-Q. Zhao, G.-Q. Zhang and H.-L. Li, *Electrochemistry Communications*, 2007, **9**, 1282-1287.

[16] Y. Sun, C. Liu, D. C. Grauer, J. Yano, J. R. Long, P. Yang and C. J. Chang, *Journal of the American Chemical Society*, 2013, **135**, 17699-17702.

[17] C. Rao and K. Pisharody, *Progress in Solid State Chemistry*, 1976, **10**, 207-270.

[18] S. Peng, L. Li, H. Tan, R. Cai, W. Shi, C. Li, S. G. Mhaisalkar, M. Srinivasan, S. amakrishna and Q. Yan, *Advanced Functional Materials*, 2014, **24**, 2155-2162.

[19] J.-C. Xing, Y.-L. Zhu, Q.-W. Zhou, X.-D. Zheng and Q.-J. Jiao, *Electrochimica Acta*, 2014, **136**, 550-556.

[20] P. Justin and G. R. Rao, *international journal of hydrogen energy*, 2010, **35**, 9709-9715.

[21] R. S. Ray, B. Sarma, A. L. Jurovitzki and M. Misra, *Chemical Engineering Journal*, 2015, **260**, 671-683.

[22] M. D. Khan, J. Akhtar, M. A. Malik, M. Akhtar and N. Revaprasadu, *New Journal of Chemistry*, 2015, **39**, 9569-9574.

[23] M. D. Khan, S. Hameed, N. Haider, A. Afzal, M. C. Sportelli, N. Cioffi, M. A. Malik and J. Akhtar, *Materials Science in Semiconductor Processing*, 2016, **46**, 39-45.

[24] M. Khan, M. Malik, J. Akhtar, S. Mlowe and N. Revaprasadu, *Thin Solid Films*, 2017, **638**, 338-344.

[25] A. A. Memon, M. Dilshad, N. Revaprasadu, M. A. Malik, J. Raftery and J. Akhtar, *Turkish Journal of Chemistry*, 2015, **39**, 169-178.

[25] C.K. Das, ACS Appl. Mater. Interfaces (2014).

[26] R. A. Hussain, A. Badshah, N. Haider, M. D. Khan and B. Lal, *Journal of Chemical Sciences*, 2015, **127**, 499-507.

[27] M. Congiu, L. Albano, F. Decker and C. Graeff, *Electrochimica Acta*, 2015, **151**, 517-524.

[28] F. Srouji, M. Afzaal, J. Waters and P. O'Brien, *Chemical Vapor Deposition*, 2005, **11**, 91-94.

[29] K. Ramasamy, M. A. Malik, P. O'Brien and J. Raftery, *Dalton Transactions*, 2010, **39**, 1460-1463.

[30] K. Ramasamy, W. Maneerprakorn, M. A. Malik and P. O'Brien, *Philosophical Transactions of the Royal Society of London A: Mathematical, Physical and Engineering Sciences*, 2010, **368**, 4249-4260.

[31] W. Maneeprakorn, M. A. Malik and P. O'Brien, *Journal of Materials Chemistry*, 2010, **20**, 2329-2335.

[32] C. Gervas, S. Mlowe, M. P. Akerman and N. Revaprasadu, *New Journal of Chemistry*, 2018.

[33] D. P. Dutta, G. Sharma and I. Gopalakrishnan, *Materials Letters*, 2008, **62**, 1275-1278.

[34] N. Mntungwa, M. Khan, S. Mlowe and N. Revaprasadu, *Materials Letters*, 2015, **145**, 239-242.

[35] N. Hollingsworth, A. Roffey, H.-U. Islam, M. Mercy, A. Roldan, W. Bras, M. Wolthers, C. R. A. Catlow, G. Sankar and G. Hogarth, *Chemistry of Materials*, 2014, **26**, 6281-6292.

[36] Y. K. Jung, J. I. Kim and J.-K. Lee, *Journal of the American Chemical Society*, 2009, **132**, 178-184.

[37] C. F. Macrae, I. J. Bruno, J. A. Chisholm, P. R. Edgington, P. McCabe, E. Pidcock, L. Rodriguez Monge, R. Taylor, J. van de Streek and P. A. Wood, *J. Appl. Cryst*., 2008, **41,** 466-470, Mercury CSD.

[38] J. Zhang, F. Jian, L. Lu, X. Yang, X. Wang, *J.Chem.Cryst.* 2001, **31**, 251

[39] R.J.Butcher, E.Sinn, *J.Am.Chem.Soc.* 1976, **98**, 2440

[40] P.C.Healy, E.Sinn, *Inorg.Chem.* 1975, **14**, 109

[41] P.Deplano, E.F.Trogu, F.Bigoli, M.A.Pellinghelli, *J.Chem.Soc.,Dalton Trans.* 1987, 2407

[42] F.G.Herring, J.M.Park, S.J.Rettig, J.Trotter, Can.J.Chem. 1979, **57**, 2379

Appendix 4.1

References

[1] W. Zhao, C. Zhang, F. Geng, S. Zhuo and B. Zhang, *ACS Nano*, 2014, **8**, 10909–10919.

[2] B. Chen, R. Li, G. Ma, X. Gou, Y. Zhu and Y. Xia, *Nanoscale*, 2015, **7**, 20674–20684.

[3] H. Hu, B. Guan, B. Xia and X. W. Lou, *J. Am. Chem. Soc.*, 2015, **137**, 5590–5595.

[4] C. K. Ranaweera, C. Zhang, S. Bhoyate, P. K. Kahol, M. Ghimire, S. R. Mishra, F. Perez, B. K. Gupta and R. K. Gupta, *Mater. Chem. Front.*, 2017, **1**, 1580–1584.

[5] J. Ryu, N. Jung, J. H. Jang, H. J. Kim and S. J. Yoo, *ACS Catal.*, 2015, **5**, 4066–4074.

[6] Y.-P. Zhu, Y.-P. Liu, T.-Z. Ren and Z.-Y. Yuan, *Adv. Funct. Mater.*, 2015, **25**, 7337–7347.

[7] M. Shen, C. Ruan, Y. Chen, C. Jiang, K. Ai and L. Lu, *ACS Appl. Mater. Interfaces*, 2015, **7**, 1207–1218.

[8] S. Dou, L. Tao, J. Huo, S. Wang and L. Dai, *Energy Environ. Sci.*, 2016, **9**, 1320–1326.

[9] T. Liu, Y. Liang, Q. Liu, X. Sun, Y. He and A. M. Asiri, *Electrochem. commun.*, 2015, **60**, 92–96.

[10] J. Wang, H. X. Zhong, Z. L. Wang, F. L. Meng and X. B. Zhang, *ACS Nano*, 2016, **10**, 2342–2348.

[11] P. Cai, J. Huang, J. Chen and Z. Wen, *Angew. Chemie Int. Ed.*, 2017, **56**, 4858–4861.

[12] H. Zhu, J. Zhang, R. Yanzhang, M. Du, Q. Wang, G. Gao, J. Wu, G. Wu, M. Zhang, B. Liu, J. Yao and X. Zhang, *Adv. Mater.*, 2015, **27**, 4752–4759.

[13] P. Ganesan, M. Prabu, J. Sanetuntikul and S. Shanmugam, *ACS Catal.*, 2015, **5**, 3625–3637.

[14] Y. Wang, J. Tang, B. Kong, D. Jia, Y. Wang, T. An, L. Zhang and G. Zheng, *RSC Adv.*, 2015, **5**, 6886–6891.

[15] H. Jin, J. Wang, D. Su, Z. Wei, Z. Pang and Y. Wang, *J. Am. Chem. Soc.*, 2015, **137**, 2688–2694.

[16] X. Li, Z. Niu, J. Jiang and L. Ai, *J. Mater. Chem. A*, 2016, **4**, 3204–3209.

[17] J. Wang, D. Gao, G. Wang, S. Miao, H. Wu, J. Li and X. Bao, *J. Mater. Chem. A*, 2014, **2**, 20067–20074.

[18] Y. Hou, M. R. Lohe, J. Zhang, S. Liu, X. Zhuang and X. Feng, *Energy Environ. Sci.*, 2016, **9**, 478–483.

[19] X. Wu, X. Han, X. Ma, W. Zhang, Y. Deng, C. Zhong and W. Hu, *ACS Appl. Mater. Interfaces*, 2017, **9**, 12574–12583.

[20] L. L. Feng, G. D. Li, Y. Liu, Y. Wu, H. Chen, Y. Wang, Y. C. Zou, D. Wang and X. Zou, *ACS Appl. Mater. Interfaces*, 2015, **7**, 980–988.

[21] H. Zhang, Y. Li, G. Zhang, P. Wan, T. Xu, X. Wu and X. Sun, *Electrochim. Acta*, 2014, **148**, 170–174.

[22] S. Liu, C. Mao, Y. Niu, F. Yi, J. Hou, S. Lu, J. Jiang, M. Xu and C. Li, *ACS Appl. Mater. Interfaces*, 2015, **7**, 25568–25573.

[23] Z. Yang, C.-Y. Chen and H.-T. Chang, *J. Power Sources*, 2011, **196**, 7874–7877.

[24] F. Tao, Y. Q. Zhao, G. Q. Zhang and H. L. Li, *Electrochem. commun.*, 2007, **9**, 1282–1287.

[25] B. You, N. Jiang, M. Sheng and Y. Sun, *Chem. Commun.*, 2015, **51**, 4252–4255.

[26] X. Meng, J. Deng, J. Zhu, H. Bi, E. Kan and X. Wang, *Sci. Rep.*, 2016, **6**, 1–9.

[27] J. Y. Lin, S. Y. Tai and S. W. Chou, *J. Phys. Chem. C*, 2014, **118**, 823–830.

[28] F. Luo, J. Li, H. Yuan and D. Xiao, *Electrochim. Acta*, 2014, **123**, 183–189.

[29] R. S. Ray, B. Sarma, A. L. Jurovitzki and M. Misra, *Chem. Eng. J.*, 2015, **260**, 671–683.

[30] H. Wan, X. Ji, J. Jiang, J. Yu, L. Miao, L. Zhang, S. Bie, H. Chen and Y. Ruan, *J. Power Sources*, 2013, **243**, 396–402.

CHAPTER FIVE

EFFECT OF CATIONIC DISORDER ON THE ENERGY GENERATION AND ENERGY STORAGE APPLICATIONS OF $Ni_xCO_{3-x}S_4$ THIOSPINEL

5.1. Introduction

Various electroactive materials such as transition metal sulfides (*e.g.* NiS_x, CuS_x, and CoS_x) [1,2], carbonaceous materials [3], oxides of transition metals [4] and conducting polymers [5] are regarded as good materials for supercapacitors. However, the cycling performance of transition metal sulfides is not satisfactory as they pulverize electrode materials in the course of cycling, which leads to poor electrical connectivity to electrode materials from current collectors. Similarly, the low capacitance of carbon-based materials, average electronic conductivity and high costs for transition metal oxides such as $RuO_x.nH_2O$, as well as poor cyclic stability of conducting polymers, make supercapacitors fabricated from these materials less efficient [6].

Recently, oxide and sulfide-based ternary compounds of cobalt and nickel have attracted the attention of researchers due to their high efficiency in energy generation and energy storage devices. Ternary metallic oxides such as $NiCo_2O_4$, have been considered appropriate for the fabrication of supercapacitors, being a better-conducting material than the binary oxides of the parent metals, *i.e.* nickel and cobalt [7-9]. However, $NiCo_2O_4$ shows less electron conductivity when compared to its sulfide counterpart, $NiCo_2S_4$. Furthermore, the Ni-Co-S system provides the material with improved performance and stability as compared to the oxide counterpart and their binary counterparts, Co-S and Ni-S [10-12].

Thiospinels are sulfur based ternary compounds that exist in the spinel structure, whose general formula is AB_2S_4 (where $A = M^{+2}$ and $B = M^{+3}$). Such a structure is said to be built on a closely packed array of S^{-2} ions, with A^{+2} and B^{+3} metallic ions occupying the tetrahedral and octahedral sites respectively [13]. This means that the ternary Ni-Co-S system such as $NiCo_2S_4$, with a normal spinel structure, has the synergetic effect from both Ni^{+2} and Co^{+3} in the presence of S^{-2}. Hence, making the material better suited for both electrochemical activities, as well as electrocatalytic activities for H_2 and O_2 evolution reactions.

Ternary Ni-Co-S system exhibits superior quality on electrocatalytic activities for oxygen and hydrogen evolution studies [14, 15]. The bimetallic catalysts of Fe, Ni, Co

with the chalcogen atom (S, Se, Te) are potentially efficient candidates because of their natural abundance and hence low cost [16]. Furthermore, they display high electrocatalytic activity, especially when attached to relatively smaller organic molecules [17]. Bimetallic chalcogenides fit in better than binary sulfides due to synergetic effects of the transition metal atoms that often exhibit collective higher catalytic activity in different chemical environments.

Various protocols have been used to fabricate $NiCo_2S_4$. They include hydrothermal methods [16], electrochemical depositions [18], anion exchange methods [19], controlled sulfurization methods [20], and chemical bath deposition [21]. The hydrothermal method is the predominant protocol used in the preparation of $NiCo_2S_4$ as it is considered to be cost-effective and environment friendly, as compared to other protocols. Lou and co-workers synthesized hollow nanofibers, ball-in-ball hollow spheres and onion-like $NiCo_2S_4$ particles via the ion-exchange method [22-24]. The controlled growth of $NiCo_2S_4$ nanosheets on a graphene matrix was shown to lead to superior supercapacitive performance [9]. Peng *et al.*[25] reported the hydrothermal synthesis of a $NiCo_2S_4$-RGO hybrid and investigated its electrochemical performance.

In ternary and/or quaternary semiconductors, stoichiometric variations play an important role and this composition tunability is the key property to their characteristics and device performance [26]. Non-stoichiometric compounds are rarely desirable; in II-V or III-V compounds, it results in low-performing device characteristics. However, for ternary materials, this is not necessarily always true. It was observed for Cu/$AgInS_2$ nanomaterials that the In-rich compounds are better emitters as compared to Ag- or Cu-rich compositions [27]. Similarly, a slight cationic disorder in $AgBiS_2$ results in a significant change in electronic properties [28]. Although, there are some examples of cationic disorders of I-III-V compounds, the effect of cationic disorder on energy storage and/or energy generation performance of thiospinels is not very well explored.

The use of single molecular precursors is often known to give superior results in nanomaterials synthesis, as it makes use of preformed bonds with the decomposition product easily predicted [29-33]. Furthermore, they are equally suitable for the synthesis of nanomaterials and deposition of thin films [34-38].

In this chapter, a facile one-pot synthesis of $Ni_xCo_{3-x}S_4$ thiospinel nanoparticles was designed, involving the thermolysis of stoichiometric nickel and cobalt dithiocarbamate complexes in a primary amine solvent. This protocol has enabled the tuning of morphology and stoichiometry of $Ni_xCo_{3-x}S_4$. It was observed that the nanoparticles synthesized at 200 °C were cobalt-rich, whereas higher temperature (250 °C) results in the nickel-rich material. The effect of stoichiometric disorder of metals, on the energy storage and energy generation properties, has been thoroughly examined.

5.2. Experimental details

5.2.1. Materials

Ethyl piperazine 99%, carbon disulfide 99%, nickel acetate (Sigma Aldrich), cobalt chloride hexahydrate (Sigma Aldrich), oleylamine (OLA) 99%, sodium hydroxide (99%), methanol (99.5%), chloroform, acetone, and hexane were used as purchased without any further purification.

5.2.2. Synthesis of ligands and metal (Ni, Co) complexes

Ethyl piperazine dithiocarbamate ligand and the corresponding nickel/cobalt complexes were synthesized using the procedures described elsewhere [39].

The synthesis of complexes is detailed as follows: $Ni(CH_3CO_2)_2{\cdot}4H_2O$ (2.35 g, 9.43 mmol) was dissolved in the deionized water (25.0 mL), and then added drop-wise to the solution of the ethyl piperazine dithiocarbamate ligand (4.00 g, 18.86 mmol) at room temperature. The reaction mixtures were stirred for 45 min, and the precipitates were vacuum filtered, washed with deionized water and dried in an oven at 80 °C overnight. Yield: 81%. Microanalysis: Calculated for $C_{14}H_{26}N_4NiS_4$: C, 38.45; H, 5.99; N, 12.81. Found: C, 38.36; H, 6.01; N, 12.93. IR (cm^{-1}, ATR): 1006.93, *ν* (C═S); 1431, *ν* (C═N); 1499.69, *ν* (C-N); 452-360, *ν* (Ni–S).

The cobalt complex was prepared by dissolving $CoCl_2{\cdot}6H_2O$ (2.25 g, 9.43 mmol) in deionized water (25.0 mL), followed by the drop-wise addition to the aqueous solution of ligand (4.00 g, 18.86 mmol). Yield: 91%. Microanalysis: Calculated for

$C_{21}H_{39}CoN_6S_6$: C, 40.23; H, 6.27; N, 13.41. Found: C, 40.11; H, 6.08; N, 13, 62. IR (cm^{-1}, ATR): 1012.45, *v* (C═S); 1455, *v* (C═N); 1522.61, *v* (C-N).

5.2.3. Preparation of $NiCo_2S_4$ nanosheets

In a typical procedure, stoichiometric amounts of nickel and cobalt complexes (1:1) were dissolved in 3.0 mL of OLA as a dispersing/coordinating solvent and injected into OLA (5.0 mL) preheated at 200 °C. A temperature drop of about 15 °C was observed and the solution immediately turned black. The reaction temperature was maintained at 200 °C for 2 hours, after which the heating was stopped. A 30.0 mL mixture of methanol and acetone (v/v 1:1) was used for precipitation of OLA-capped $Ni_xCo_{3-x}S_4$ nanoparticles, which were then washed and separated by centrifugation. The reaction was also conducted at temperature of 250 °C, under similar conditions.

5.2.4 Characterization techniques

Characterization techniques used in this work as detailed in chapter 2 of this thesis.

5.2.4.1. X-ray photonelectron spectrometry (XPS)

X-ray photoemission spectroscopy (XPS) measurements were acquired at room temperature by means of a SPECS PHOIBOS 150 electron energy analyzer, using a Al K_α monochromatised photon source ($h\nu$ = 1486.71 eV). The overall (photon+analyser) energy resolution was set to 0.8 eV for survey spectra and to 0.6 eV for all the high-resolution XPS spectra reported in this work.

5.2.4.2. Inductively coupled plasma-optical emission spectroscopy (ICP-OES)

Inductively coupled plasma (ICP) was performed using a Perkin Elmer Optical Emission Spectrometer Optima 5300 DV. Standards (1000 ppm Ni, Co and S) were purchased from Fluka.

5.3. Results and discussion

5.3.1. Synthesis of ligand and metal (Co, Ni) complexes and thermogravimetric analyses

The synthesis of the Co complex (**5**) proceeded in a similar manner to the morpholino-dithiocarbamate derivative mentioned in chapter 4, *i.e.* the *in-situ* oxidation from Co^{+2} in metal salt to Co^{+3} in the complex [40].

The thermal stability of the complexes was investigated by the thermogravimetric analysis (TGA) technique and is shown in Figure 5.1. The Ni complex (**3**) decomposes in two steps, where a major mass loss of 72 % was observed at 324 °C, followed by a minor weight loss of 7.3 % around 385 °C (Fig 5.1 (b)). The two steps are attributed to loss of volatile organic by-products and sulfur atoms, respectively. Complex **(5)** shows single step decomposition with a weight loss of 79.16 % at 289 °C (Fig. 5.1 (a)). The residues obtained from the complex **(3)** (21.09%) and complex **(5)** (20.84%) were found to be very close to the calculated values for NiS (20.75%) and CoS (20.82%), respectively. The use of oleylamine (OLA) has two major advantages; the long alkyl chain helps in the effective capping of the nanoparticles [41], and the primary amine can catalyze the breakdown of the molecular precursors, initiating decomposition at low temperature [42]. Both nickel and cobalt sulfide systems can exist in spinel structures *i.e.* Co_3S_4 and Ni_3S_4. Similarly, a combination of both in different ratios can also be used for generation of thiospinel lattice, such as $NiCo_2S_4$, $CoNi_2S_4$ and $(Ni,Co)_3S_4$. Most of the work has been done on energy applications of $NiCo_2S_4$ but the nickel-incorporated Co_3S_4 (*i.e.* $Ni_xCo_{3-x}S_4$) has received minor attention. Both complexes show high thermal stability, however, $Ni_xCo_{3-x}S_4$ nanoparticles were synthesized with ease in OLA, at a temperature quite lower than the decomposition temperature as indicated by TGA (Figure 5.1)

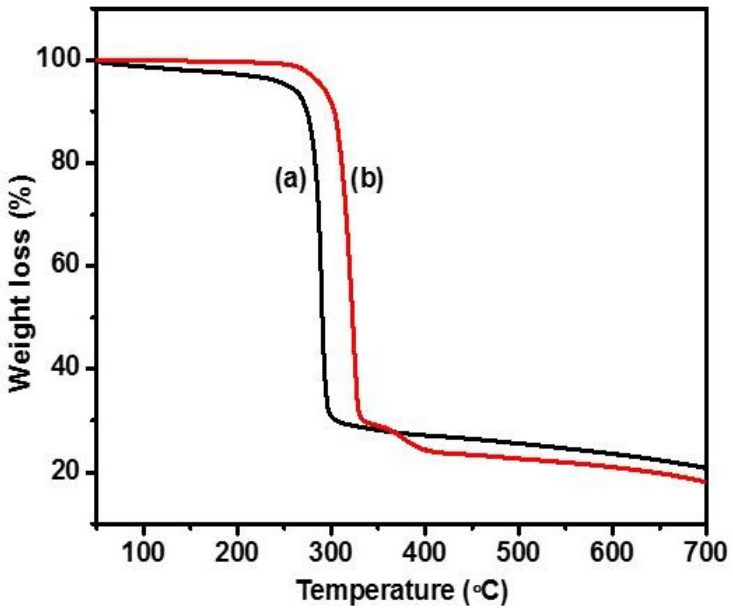

Figure 5.1: Thermogravimetric analysis plots for (a) $[Co(Etpzdtc)_3]$ (**5**), and (b) $[Ni(Etpzdtc)_2]$ (**3**) complexes.

5.3.2. Phase purity, christallinity and morphology analyses

The complexes $[Ni(Etpzdtc)_2]$ (**3**) and $[Co(Etpzdtc)_3]$ (**5**) were dispersed in OLA in stoichiometric amounts (1:1), and subsequently injected in OLA preheated at 200 °C and/or 250 °C, under similar reaction conditions. The effect of temperature was examined on the morphology, crystallinity, and composition of the synthesized $Ni_xCo_{3-x}S_4$ nanoparticles.

The phase of the synthesized OLA-capped $Ni_xCo_{3-x}S_4$ nanoparticles was determined by p-XRD measurements (Figure 5.2). The diffraction peaks of the nanoparticles synthesized in both reaction temperatures were indexed to the (220), (311), (400), (422), (511), (440), (533), (444) and (553) planes, which match well with the standard pattern for $NiCo_2S_4$ (card number: 01-073-1704). The diffraction peaks are respectively positioned at 2θ = 26.84°, 31.58°, 38.32°, 47.40°, 50.47°, 55.31°, 65.10°, 69.29°, 78.76°. There was no detectable impurities, secondary phase or unassigned peaks. The intensity of the peaks was however comparatively less pronounced at a lower reaction temperature (200 °C) than at a higher reaction temperature of 250 °C.

Coordinating solvents can reduce the decomposition temperature of both precursors; however, crystallinity can only be enhanced by increasing the temperature. The absence of common binary phases, such as NiO, CoO, NiS, and CoS confirms the phase purity of ternary nanomaterials prepared from single molecular precursors. The p-XRD displays typical behaviour of cobalt-rich minerals *i.e.* the rising trend of the diffraction pattern from the baseline. It is attributed to the energy of the Kα radiation of copper being higher than the k-absorption edge of cobalt; hence, cobalt fluoresces strongly and gives rise to such behaviour. The calculation of the lattice constant *a* using diffraction peak (311) resulted in 9.319 Å, which is in agreement with previous reports [21].

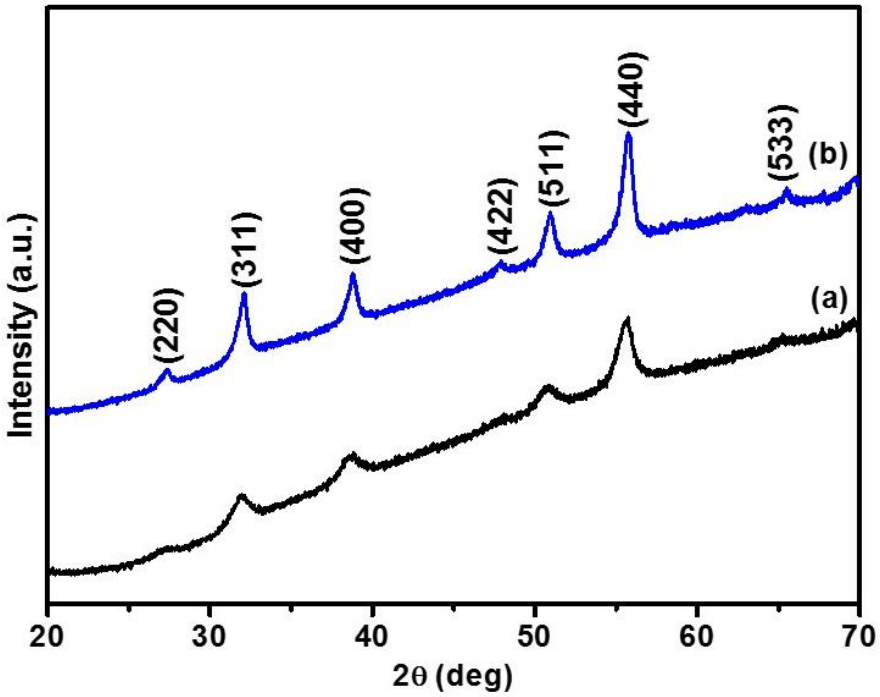

Figure 5.2: p-XRD pattern for OLA-capped $NiCo_2S_4$ synthesized at (a) 200 °C and (b) 250 °C.

The morphology of the nanomaterials was analysed by the microscopic imaging technique (Figure 5.3). The synthesis of $Ni_xCo_{3-x}S_4$ at 200 °C indicates the formation of nanosheets. The sheets were stacked and showed a poly-dispersed nature, whereas, the size of the nanosheets was in the order of microns. The crystalline nature of the nanosheets was indicated by clear lattice fringes and the presence of well-defined diffraction spots in the selective area electron diffraction (SAED) pattern (Figure 5.3 b). Similar sheet-like morphology was observed for $Ni_xCo_{3-x}S_4$ synthesized at 250 °C (Figure

5.3 c). However, the rate of nucleation increases many folds with an increase in temperature, hence, growth defects such as twinning and some stacking faults were observed (Figure 5.3 d). Figure 5.3 e shows high-angle annular dark-field (HAADF) image and the elemental mapping indicates a uniform distribution of all elements in the sample. The composition by ICP analysis indicates that the sample prepared at 200 °C was cobalt-rich and the exact composition of the sample was found to be $Ni_{1.22}Co_{1.50}S_{4.31}$ (henceforth referred to as **NiCoS-1**), whereas, the sample synthesized at 250 °C was nickel-rich, and a stoichiometric composition of $Ni_{1.63}Co_{1.18}S_{4.17}$ (henceforth referred to as **NiCoS-2**) was observed.

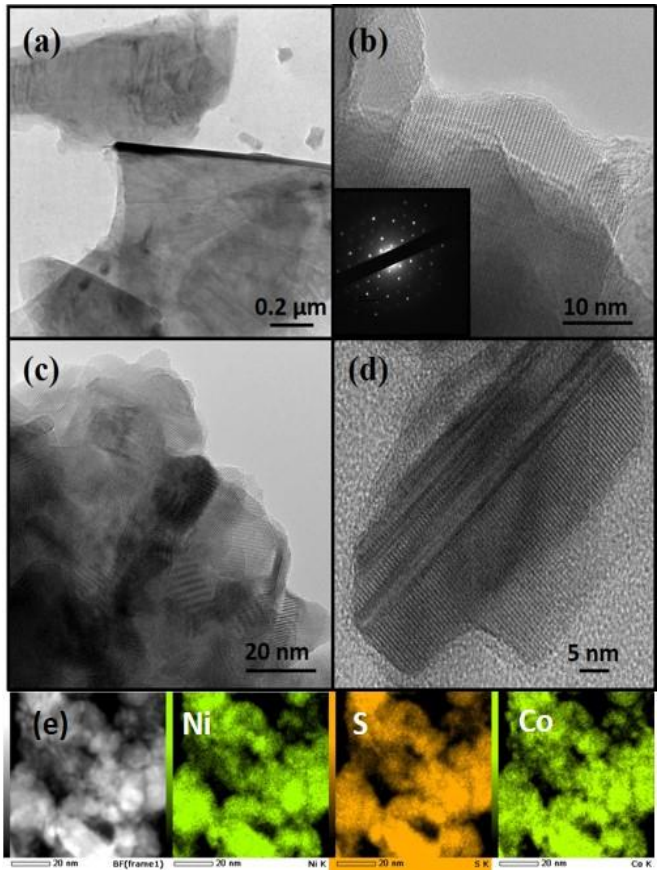

Figure 5.3: TEM images for OLA-capped $NiCo_2S_4$ synthesized at (a-b) 200 °C (c-d) 250 °C and (e) shows HAADF image along with elemental mapping of nanosheets synthesized at 200 °C.

5.3.3. XPS Measurements for the ternary samples (NiCoS-1 and NiCoS-2)

The XPS measurements were performed to investigate the electronic structure and the oxidation states of Ni, Co, and S in both samples of the $Ni_xCo_{3-x}S_4$ series. Figure 5.4 a shows the comparison of the wide scans for the investigated samples. Spectra show all expected peaks, as well as those of O, C, and N. O may be derived from the exposure of the sample to the atmosphere, whereas C and N, present in very moderate quantities, derive from the use of oleylamine.

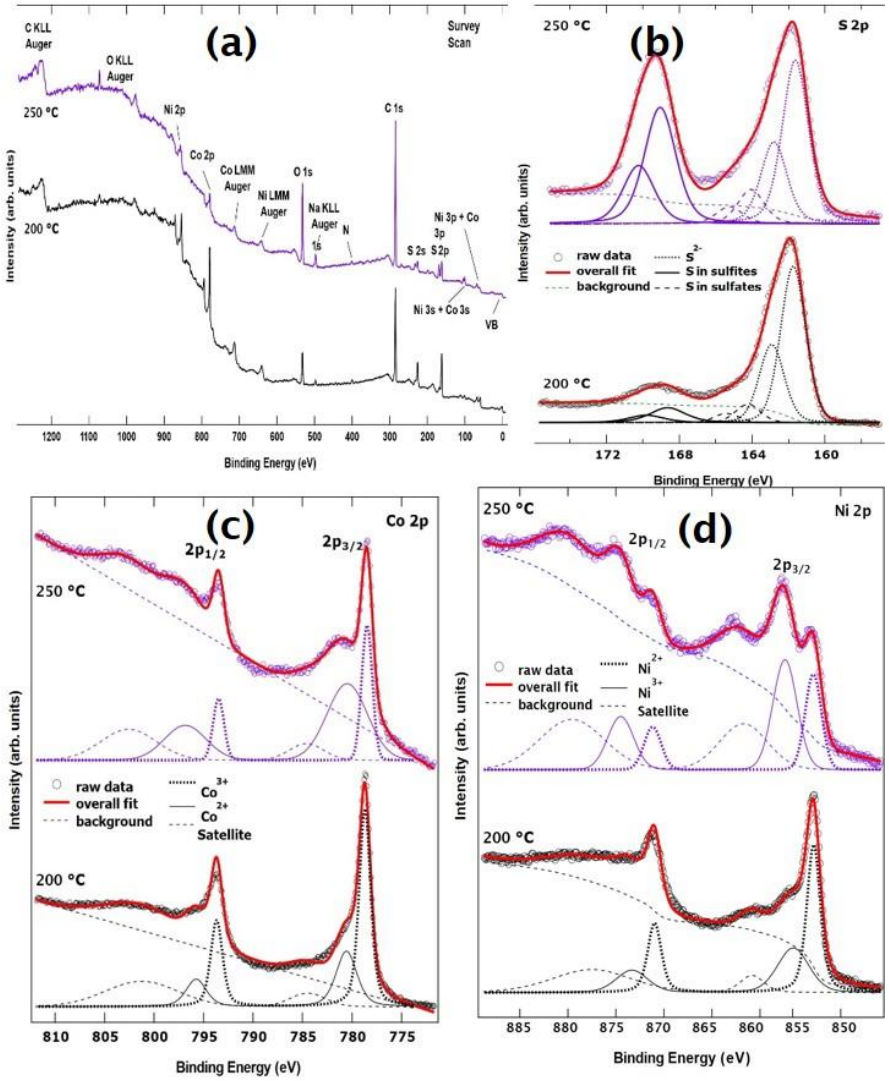

Figure 5.4: (a) XPS survey spectra (b) S 2p core level spectra (c) Co 2p core level spectra and (d) Ni 2p core level spectra for both samples synthesized at 200 °C and 250 °C.

Figure 5.4 c shows the Co 2p core level for the investigated samples. The Co 2p binding energy region is dominated by two sharp peaks located at ~779 eV and ~794 eV binding energy, and two broad peaks at ~780.5 eV and ~796.5 eV, which correspond to the Co $2p_{3/2}$ and Co $2p_{1/2}$ spin-orbit components for Co^{3+} and Co^{2+} oxidation states, respectively. The identification of Co^{2+} and Co^{3+} oxidation states is consistent with literature reports on similar NiCo-based systems [43-45]. In addition to the main peaks, two weak shake-up satellites were detected at about 6.5 eV towards higher binding energy from the Co^{3+} peaks. The line shape of this core level was fitted using three spin-orbit doublets, as shown in Figure 5.4. Each doublet is separated by a spin-orbit splitting of approximately 15.1 eV. The overall fit to the experimental data (thick line) shows good agreement with the raw data. Table 5.1 displays the Co $2p_{3/2}$ binding energy of the three doublets, as well as the area ratio between Co^{2+}/Co^{3+} oxidation states. It was clearly demonstrated that the area changes quite drastically from one sample to the other, reflecting an intrinsic difference in the electronic structure within the series.

Table 5.1: Binding energies of the Co $2p_{3/2}$ peak for Co^{3+} and Co^{2+} oxidation states, and Co^{2+} satellite. The last column shows the Co^{2+}/Co^{3+} intensity ratio from the fitted doublets.

Sample	**BE Co^{3+} (eV)**	**BE Co^{2+} (eV)**	**Co^{2+} satellite**	**Intensity ratio (Co^{2+}/Co^{3+})**
NiCoS-1	778.72	780.59	784.5	0.50
NiCoS-2	778.51	780.52	784.63	2.13

Figure 5.4 d shows the comparison of the fitted Ni 2p XPS core level spectra. The Ni $2p_{3/2}$ and $2p_{1/2}$ spectral regions are composed of three spin-orbit doublets corresponding to Ni^{3+}, Ni^{2+} and a broad shake-up satellite of the Ni^{3+} species, respectively. As for the Co 2p core level, the fitted components, together with a Shirley-type background, are provided in Figure 5.4. Table 5.2 displays the Ni $2p_{3/2}$ binding energy of the three doublets, as well as the area ratio between Ni^{2+}/Ni^{3+} oxidation states. Interestingly, the ratios for Ni oxidation states have an opposite trend with respect to

those for Co. This was anticipated since charge neutrality of the samples had to be ensured.

Table 5.2: Binding energies of the Ni $2p_{3/2}$ peak for Ni^{2+} and Ni^{3+} oxidation states, and Ni^{3+} satellite. The last column shows the Ni^{2+}/Ni^{3+} intensity ratio from the fitted doublets.

Sample	BE Ni^{2+} (eV)	BE Ni^{3+} (eV)	Ni^{3+} satellite	Intensity ratio (Ni^{2+}/Ni^{3+})
NiCoS-1	853.27	855.47	859.9	1.56
NiCoS-2	853.21	856.36	860.83	0.57

As per general observations, the line shapes of the Co 2p and Ni 2p core levels, as well as the presence of both divalent and trivalent oxidation states, are consistent with previous literature reports on $NiCo_2S_4$ [18, 45]. Ni-Co-S has the tendency to exist in two mineralogical forms *i.e.* $NiCo_2S_4$ or $CoNi_2S_4$. In $NiCo_2S_4$, Ni is in the +2 oxidation state, whereas Co is in the +3 oxidation state. However, a small amount of Ni can convert to +3 oxidation state and Co can occupy the site with +2 oxidation state. The ratio can be increased if, comparatively, one of the elements is in slight excess, and can occupy the position of the deficient element as well to stabilize the spinel framework. The XPS results from the S 2p core level are reported in Figure 5.4 b. The line shape is consistent with previous reports on these systems.[44, 45] Since the spin-orbit splitting between the $2p_{3/2}$ and the $2p_{1/2}$ peaks in sulfur is only 1.18 eV (*i.e.* of the same order of magnitude as the experimental resolution for these measurements), it is good practice to report the $2p_{3/2}$ and the $2p_{1/2}$ peaks as separate peaks in the figure. This is to aid in visualization of the fits to the spectra. The main spin-orbit doublet at lower binding energy is attributed to S in the 2- oxidation state. This is typically of sulfur ions bonded to metallic ions in ternary metal sulfides [46]. The S 2p doublets whose $2p_{3/2}$ peaks are observed at 164 eV and 169 eV are attributed to surface sulfur with high oxide state, such as sulfites and sulfates, respectively. The binding energies of the $2p_{3/2}$ core level for these three doublets are reported in Table 5.3.

Table 5.3: Binding energies of the S $2p_{3/2}$ peak for the S^{2-} oxidation state, as well as the sulfur ion in sulfites and sulfates absorbates.

Sample	BE S^{2-} (eV)	BE S in sulfites (eV)	BE S in sulfates (eV)
NiCoS-1	161.74	164.22	168.63
NiCoS-2	161.62	164.06	169.05

5.3.4. Electrocatalytic energy generation for the ternary samples (NiCoS-1 and NiCoS-2)

The OER performance of the **NiCoS-1** and **NiCoS-2** was first investigated. Figure 5.5 a shows the LSV polarization curves for NixCo3-xS4 samples in 1M KOH. It can be observed that the **NiCoS-2** exhibited the lower overpotential of 327 mV to generate a current density of 10 mA/cm^2, while NiCoS-1 needs overpotential of 348 mV at 10 mA/cm^2. The OER kinetics of the electrocatalysts were further analyzed using Tafel plots. As seen in Figure 5.5 b, the Tafel slope for the **NiCoS-1** and **NiCoS-2** was calculated to be 90 and 89 mV/dec, respectively. The lower Tafel slope for **NiCoS-2** indicated faster OER catalytic kinetics than **NiCoS-1**. The lower overpotential and faster kinetics suggest that **NiCoS-2** has a better electrocatalytic performance compared to **NiCoS-1**. One of the reasons for this could be the nickel-rich parameter of the sample synthesized at 250 °C. The **NiCoS-2** sample showed high activity, possibly due to high concentration of Ni^{+3} and presence of mixed valence states which can be explained by a self-doping phenomenon of the material [47]. The increase in Ni^{+3} species may result in n-type doping as it provides extra electrons, whereas Co^{+2} may lead to p-type doping by providing extra holes. Hence, a higher Ni^{+3} concentration will result in enhanced electrical conductivity for electrons, therefore, leads to better electrochemical/electrocatalytic performances [48].

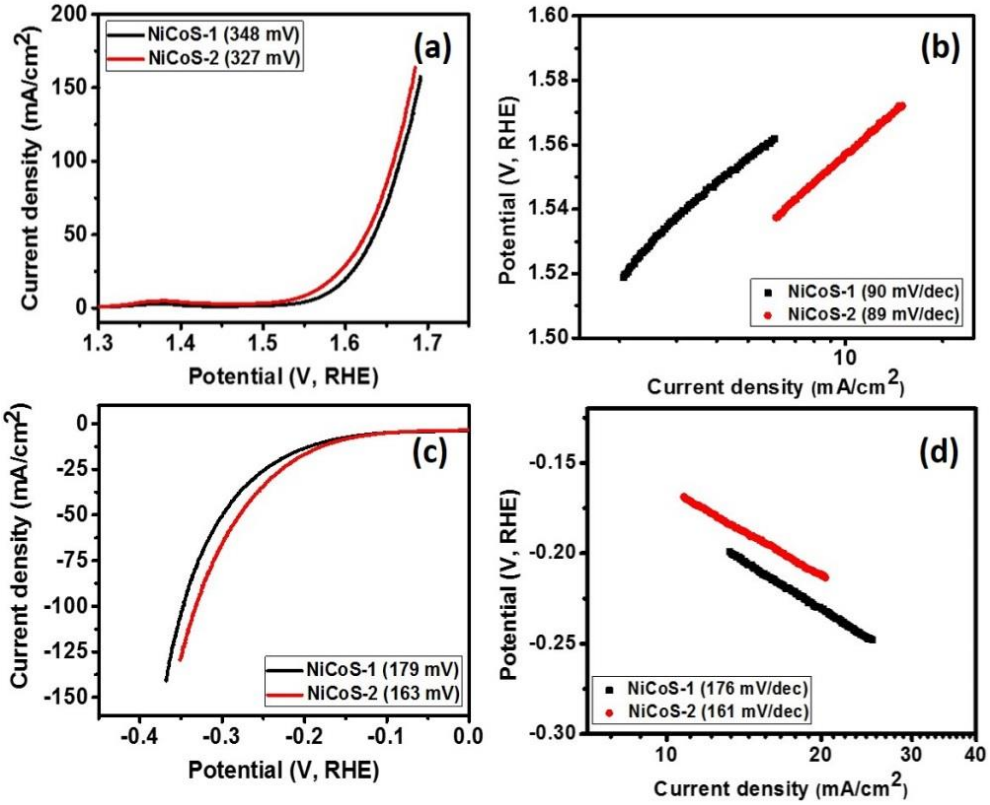

Figure 5.5: (a) Polarization curves and (b) Tafel slopes for $Ni_xCo_{3-x}S_4$ samples in OER range and (c) Polarization curves and (b) Tafel slopes for $Ni_xCo_{3-x}S_4$ samples in HER range.

Furthermore, the high degree of crystallinity in **NiCoS-2** compared to **NiCoS-1**, is linked to the enhanced electrocatalytic performance [49]. From the overall observation, both **NiCoS-1** and **NiCoS-2** have improved performances than other $NiCo_2S_4$ reported in literature. Liu *et al.*[50] have synthesized $NiCo_2S_4$ nanowire arrays through sulfidization of the $NiCo_2S_4$ precursor, which was uniformly grown on the carbon cloth using a hydrothermal reaction. The synthesized $NiCo_2S_4$ electrocatalyst required an overpotential of 340 mV to generate a current density of 100 mA/cm^2 with a Tafel slope of 89 mV/dec. $NiCo_2S_4$ with porous nanosheets array topology on carbon cloth was prepared by Zhu *et al.* [51] through two-step hydrothermal process. It showed a Tafel slope of 91 mV/dec. Table 5.4 shows the comparison with other recently reported OER catalyst using non-precious metals in the alkaline medium.

Table 5.4: Comparison of OER performance of some recently reported electrocatalysts.

Catalyst	Overpotential (mV) at 10 mA/cm^2	Tafel Slope (mV/decade)	Reference
$NiCo_2O_4$/CC	~380	90	[2]
$NiCo_2S_4$/CC	~275	89	[2]
$NiCo_2O_4$ NS/CC	320	95	[3]
$NiCo_2S_4$ NS/CC	240	91	[3]
$NiCo_2O_4$	565	292	[4]
$NiCo_2O_4$ Nanosponge	362	64	[5]
NiCo LDH NP	430	62	[6]
NiCo LDH NS	367	40	[6]
Co_3O_4	410	110	[7]
Co_3O_4/$NiCo_2O_4$	340	88	[7]
Ni_3S_2	340	150	[8]
$Co_{0.5}Fe_{0.5}S$@N-MC	410	159	[9]
Zn-Co-S NS	390	136	[10]
Zn-Co-S NP	330	97	[10]
Co_9S_8/Graphene	441	94	[11]
N-Co_9S_8/Graphene	409	83	[11]
$NiCo_2S_4$-1	**348**	**90**	**This work**
$NiCo_2S_4$-2	**327**	**89**	**This work**

Note: References to tables 4 and 5 are attached as appendix 5.1 at the end of this chapter.

The HER activity of the $Ni_xCo_{3-x}S_4$ samples was also studied, the polarization curves for $Ni_xCo_{3-x}S_4$ samples in HER region is given in Figure 5.5 c. As seen in Figure 5.5 c, **NiCoS-2** required an overpotential 163 mV, while **NiCoS-1** required an overpotential of 179 mV to achieve a current density of 10 mA/cm^2. The polarization

curves for **NiCoS-2** showed significant improvement in the HER performance compared to **NiCoS-1**. It can be observed from Figure 5.5 d, the Tafel slopes for **NiCoS-1** and **NiCoS-2** were calculated to be 176 and 161 mV/dec, respectively. The lower Tafel slope for **NiCoS-2** showed faster HER kinetics for electrocatalysts, which confirmed the better HER performance. Sivanantham *et al*.[52] have used a two-step hydrothermal method to complete the in-situ growth of hierarchical $NiCo_2S_4$ nanowire arrays on a nickel foam substrate, which needed an overpotential of 210 mV to deliver a hydrogen production current density of 10 mA/cm^2. The $NiCo_2S_4$ electrocatalyst prepared by Liu *et al*.[50] required an overpotential of 305 mV to generate a current density of 10 mA/cm^2 with a Tafel slope of 141 mV/dec. The $NiCo_2S_4$ with porous nanosheets array topology showed an overpotential of 181 mV to reach 10 mA/cm^2 [51]. The other recently reported HER catalytic properties using Ni, Co, and other non-precious metals in the alkaline medium are given in Table 5.5.

To further understand the reason for improved electrocatalytic properties of **NiCoS-2** sample, the electrochemical active surface area of **NiCoS-1** and **NiCoS-2** was determined using cyclic voltammograms in the non-faradic region. All the CV measurements were performed in a potential range of 0.87-0.92 V (vs. RHE), where no faradic reactions were observed. The CV curves were recorded for **NiCoS-1** and **NiCoS-2** at various scan rates to determine the electrochemical double layer capacitance (C_{dl}), which is directly proportional to the electrochemical active surface area of the sample. C_{dl} was calculated by plotting half of the difference in positive and negative current densities at 0.895 V (vs. RHE) versus the scan rates (Figure 5.6 a). The C_{dl} value of the **NiCoS-1** and **NiCoS-2** was calculated to be 2.27 and 7.48 mC/cm^2, respectively. The effective electrochemical surface area of the **NiCoS-2** is more than three times higher than that of the **NiCoS-1**. The highest active electrochemical surface area provides **NiCoS-2** the better OER and HER activity than **NiCoS-1** [53].

Table 5.5: Comparison of HER performance of some recently reported electrocatalysts in alkaline medium.

Catalyst	Overpotential (mV) at 10 mA/cm^2	Tafel Slope (mV/decade)	Reference
$NiCo_2O_4$/CC	~350	207	[2]
$NiCo_2S_4$/CC	~180	141	[2]
$NiCo_2O_4$ NS/CC	320	141	[3]
$NiCo_2S_4$ NS/CC	181	130	[3]
$NiCo_2O_4$/NF	310	92	[12]
Ni_3S_2	310	96	[12]
$NiCo_2S_4$	240	81.3	[12]
$NiCo_2S_4$ NW/NF	210	59	[12]
NiS	474	124	[13]
NiS_2	454	128	[13]
Ni_3S_2	335	97	[13]
Ni_2P Nanoparticles	225	100	[14]
$Ni_{0.9}Fe_{0.1}$/NC	231	111	[15]
EG/NiFe-LDH	~380	125	[16]
EG/$Co_{0.85}$Se/NiFe-LDH	260	160	[16]
Zn-Co-S Nanosheets	415	139	[10]
Zn-Co-S Nanoplates	304	131	[10]
CoOx@CN	235	115	[17]
Cobalt-Cobalt Oxide/N-Doped Carbon Hybrids	232	115	[17]
CoP NWs	209	129	[18]
CoP/CC	209	129	[18]
$NiCo_2S_4$-1	**179**	**166**	**This work**
$NiCo_2S_4$-2	**163**	**161**	**This work**

Note: References to tables 4 and 5 are attached as appendix 5.1 at the end of this chapter.

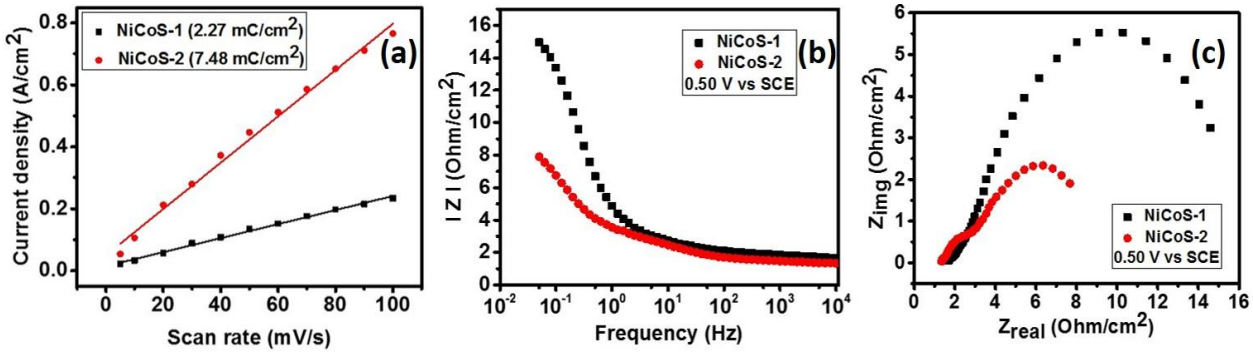

Figure 5.6: (a) Current density vs scan rate plots for $Ni_xCo_{3-x}S_4$ samples, (b) IZI vs frequency plots and (c) Z_{real} vs Z_{img} plots for $NiCo_2S_4$ samples at 0.5 V (vs. SCE).

The electrocatalytic properties of $Ni_xCo_{3-x}S_4$ samples were further analyzed using electrochemical impedance spectroscopy tests. From Figure 5.6 b, which is the plots of total impedance IZI versus frequency, it is observed that **NiCoS-2** has the lower total impedance, having only about half of the impedance of **NiCoS-1**. Moreover, **NiCoS-2** has smaller semicircle in the Nyquist plots (Figure 5.6 c). The smaller radius of the semicircle at low-frequency region suggests a lower charge transfer resistance and a faster electron transfer during electrochemical reactions. Therefore, the results of EIS tests show that the **NiCoS-2** possesses an excellent electrocatalytic performance which is consistent with the excellent OER and HER performance.

The total impedance IZI and Nyquist plots of **NiCoS-2** at various potentials are shown in Figure 5.7. It is observed that the total impedance IZI decreases with increasing potential, indicating improved electrocatalytic performance at higher potential. Similarly, the Nyquist plot starts to convert to semicircle from a straight line with the increase in the potential (Figure 5.8 b). That is because semicircle region depends on overpotential as the increase in potential provides faster reaction which leads to the reduction of semicircle's diameter.

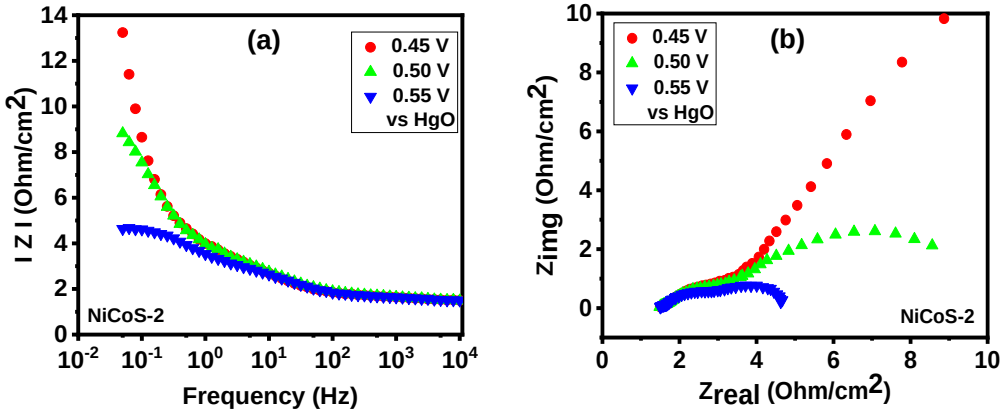

Figure 5.7: (a) IZI vs frequency plots and (b) Z_{real} vs Z_{img} plots for **NiCoS-2** sample at various overpotentials.

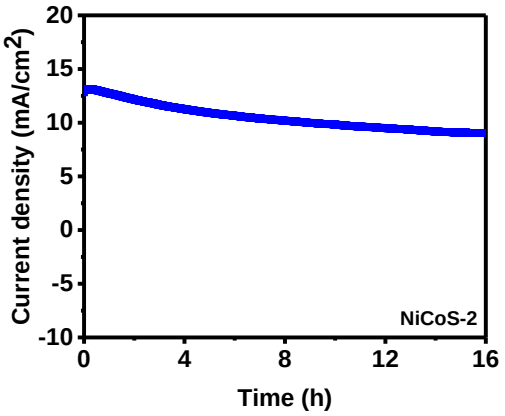

Figure 5.8: Chronoamperometry experiment for **NiCoS-2** sample.

The electrocatalytic long-term durability was measured using chronoamperometry. It was observed that the current density of NiCoS-2 was maintained almost at a constant level of 10 mA/cm^2 over the 16 h duration (Figure 5.8). The little negative effect on current density with increasing time confirms that the NiCoS-2 is very stable and could be used as a durable electrocatalyst for water splitting applications.

5.3.5. Electrochemical energy storage for the ternary samples (NiCoS-1 and NiCoS-2)

The supercapacitor performance of $Ni_xCo_{3-x}S_4$ samples was evaluated using cyclic voltammetry and galvanostatic charge-discharge (GCD) tests. Figure 5.9 a and b show the CV curves of **NiCoS-1** and **NiCoS-2** in a 3M KOH solution at various scan rates in the

voltage range of 0-0.6 V (vs. SCE). The presence of redox peaks revealed the occurrence of Faradaic redox reactions in both CV curves of $Ni_xCo_{3-x}S_4$ samples. The peak potentials for oxidation reaction and reduction reaction are about 0.45 V and 0.25 V, bilateral shifting with the increase of scan rate. In addition, the larger current density of redox peaks and area under the CV curves for **NiCoS-2** indicate the higher charge storage capacity. Moreover, from GCD curves of both $Ni_xCo_{3-x}S_4$ samples (Figure 5.9 c and d), under the same current density, **NiCoS-2** have the longer charge and discharge time compared to **NiCoS-1**, further suggesting the superior charge storage capacity. The nonlinear lines charge and discharge curves showed the pseudo-capacitance behaviour attributed to reversible redox reactions at the electrode surface.

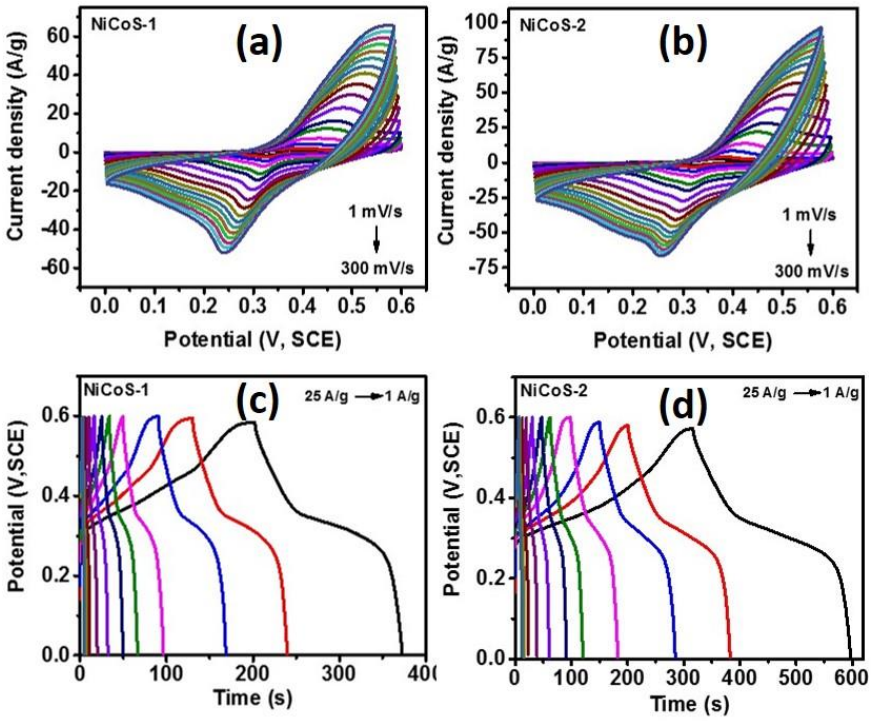

Figure 5.9: CV curves of (a) **NiCoS-1** and (b) **NiCoS-2** at various scan rates in 3M KOH electrolyte. Galvanostatic charge-discharge curves of (c) **NiCoS-1** and (d) **NiCoS-2** at various scan rates in 3M KOH electrolyte.

Specific capacitance of **NiCoS-1** and **NiCoS-2** were calculated from the CV data and GCD data and was plotted in Figure 5.10 a and b as a function of scan rates and current densities, respectively. Higher specific capacitance was observed at a lower scan rate and lower current density for both $Ni_xCo_{3-x}S_4$ samples because of lower scan rate and

lower current density provides more time for redox reactions. The maximum specific capacitance of **NiCoS-2** was 1273 F/g and 494 F/g which were calculated from the CV curve at a scan rate of 1 mV/s and GCD curve at 1 A/g, respectively. The supercapacitor performances of **NiCoS-1** and **NiCoS-2** are superior or comparable to other reported NiCo-based samples. The $NiCo_2O_4$ coral-like porous crystals synthesized using sol–gel approach by Wu *et al.*[54] have a capacitance of 217 F/g. Salunkhe *et al.*[55] prepared $NiCo_2O_4$ films on indium tin oxide substrates by a chemical bath deposition method. The $NiCo_2O_4$ films showed a highest specific capacitance of 490 F/g.

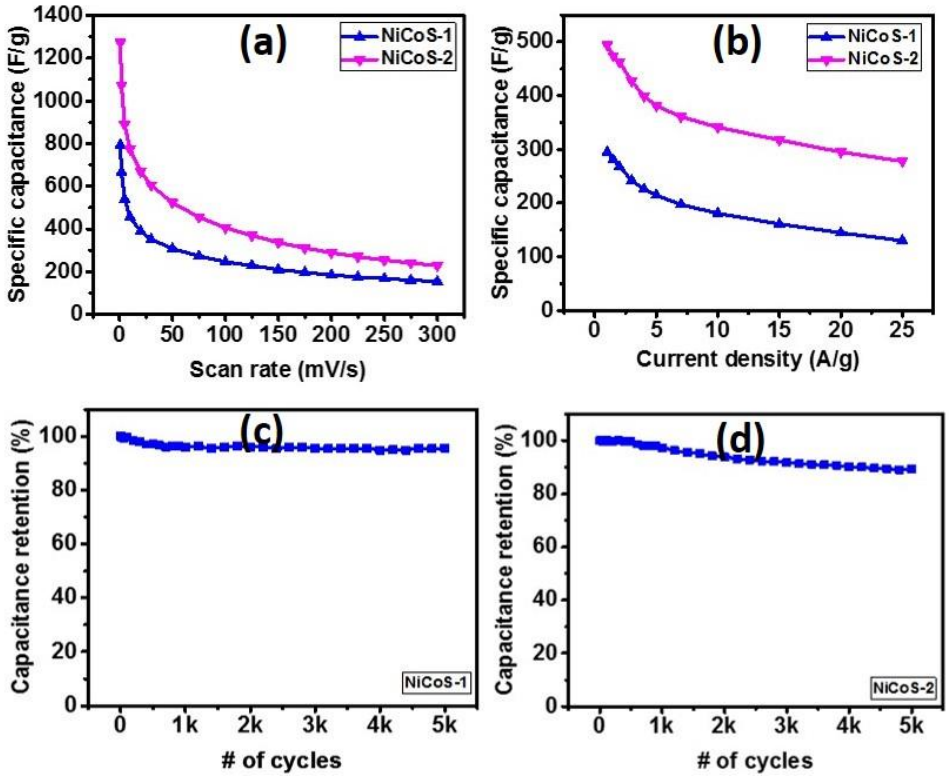

Figure 5.10: Variation of specific capacitance as a function of (a) scan rate and (b) current density for $Ni_xCo_{3-x}S_4$ samples. Cyclic stability plot for (c) **NiCoS-1** and (d) **NiCoS-2** sample using galvanostatic charge-discharge measurements.

The long-term performance of the $Ni_xCo_{3-x}S_4$ samples was studied using galvanostatic charge-discharge measurements for 5000 cycles (Figure 5.10 c-d). As seen in the capacitance versus number of cycles, both samples exhibited a very stable performance. The **NiCoS-1** and **NiCoS-2** showed capacitance retention of 95 % and 85 %

after 5000 cycles, respectively. About 60 % of capacitance was maintained after 1000 cycles for the ultrathin porous hierarchically textured $NiCo_2O_4$–graphene oxide nanosheets [9]. The capacitance of caterpillar-like $NiCo_2S_4$ nanocrystal arrays on nickel foam prepared by Chen *et al.* [56] kept 83% after 3000 cycles.

To further evaluate the performance of **NiCoS-2** as energy storage material and the effect of temperature on the electrochemical properties, a symmetrical supercapacitor device was fabricated and tested in 3M KOH using CV, GCD, and EIS. Figure 5.11 a shows the CV curves of the device at various scan rates. The potential window was as large as 1 V. From the CV curves of the device at various temperatures (Figure 5.11 b), the area under the CV curves was observed to increase with increasing temperature, showing improvement in storage capacity of the device. Similar behaviour was observed in the GCD curves at different temperatures (Figure 5.11 c). Charge and discharge time increased with temperature confirming the improvement in charge storage capacity. As seen in Figure 5.11 d, there was a 180% increase in specific capacitance when the temperature was raised from 10 to 60 °C.

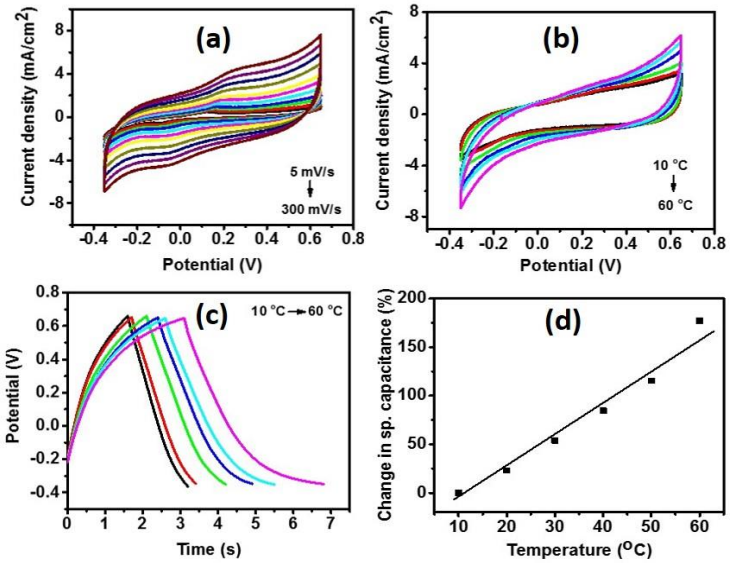

Figure 5.11: CV curves (a) at various scan rates and (b) at various temperatures, (c) Charge-discharge curves at various temperature and (b) change in specific capacitance as a function of temperature for the supercapacitor device fabricated using **NiCoS-2** electrodes.

The total impedance IZI with different frequency and Nyquist plots at various temperatures are given in Figure 5.12 a and b. As seen, total impedance IZI, Z_{real} and Z_{imag} decreases with increasing temperature, which could be due to increased mobility of the ions in the electrolyte [47]. Similar phenomena were observed in other reports [57]. A 150% improvement in the specific capacitance of the device using flower-structure $NiCo_2O_4$ by increasing temperature from 10 to 60 °C [8].

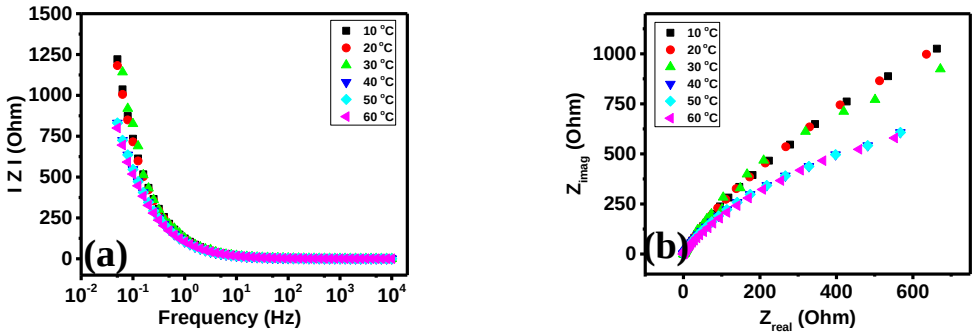

Figure 5.12: Variation of (a) I Z I vs frequency and (b) Z_{real} and Z_{imag} at various temperatures for the supercapacitor device fabricated using **NiCoS-2** electrodes.

5.4. Conclusion

In summary, Co or Ni-rich $Ni_xCo_{3-x}S_4$ nanosheets were synthesized from the corresponding metal complexes of ethyl piperazino-dithiocarbamate, which were used as molecular precursors. The nanosheets were used for oxygen evolution reaction and a lower Tafel slope (89 mV/dec) was observed for Ni-rich nanosheets which indicates better OER performance, as compared to Co-rich nanosheets (90 mV/dec). Similarly, the Tafel slope for Co-rich and Ni-rich were calculated to be 176 and 161 mV/dec respectively, which shows the superior HER performance of Ni-rich nanosheets. The efficiency of $Ni_xCo_{3-x}S_4$ nanosheets was also investigated for supercapacitance performance. The GCD curves indicate superior charge storage performance of Ni-rich nanosheets and a maximum specific capacitance of 1273 F/g and 494 F/g were observed from the CV curve at a scan rate of 1 mV s^{-1} and GCD curve at 1 A/g. Both samples exhibited a very stable long-term performance and Co-rich versus Ni-rich samples showed capacitance retention of 95% and 85% after 5000 cycles, respectively. Overall, the Ni-rich $Ni_xCo_{3-x}S_4$ sample indicates superior energy generating and storage efficiency.

The study indicates the significance of the metallic stoichiometric variation on properties of thiospinel materials, and a way to tune the efficiency of the ternary materials by the slight modification of metallic composition.

5.5 References

[1] H. Zhang, X. Yu, D. Guo, B. Qu, M. Zhang, Q. Li and T. Wang, *ACS Appl. Mater. Interfaces*, 2013, **5**, 7335-7340.

[2] H. Wan, X. Ji, J. Jiang, J. Yu, L. Miao, L. Zhang, S. Bie, H. Chen and Y. Ruan, *J. Power Sources*, 2013, **243**, 396-402.

[3] L. Hao, X. Li and L. Zhi, *Adv. Mater.*, 2013, **25**, 3899-3904.

[4] Y. Zhang, L. Li, H. Su, W. Huang and X. Dong, *J. Mater. Chem. A*, 2015, **3**, 43-59.

[5] Q. Wu, Y. Xu, Z. Yao, A. Liu and G. Shi, *ACS Nano*, 2010, **4**, 1963-1970.

[6] C.-C. Hu and W.-C. Chen, *Electrochim. Acta*, 2004, **49**, 3469-3477.

[7] Y. Zhu, X. Ji, Z. Wu, W. Song, H. Hou, Z. Wu, X. He, Q. Chen and C. E. Banks, *J. Power Sources*, 2014, **267**, 888-900.

[8] R. K. Gupta, J. Candler, S. Palchoudhury, K. Ramasamy and B. K. Gupta, *Sci. Rep.*, 2015, **5**, 15265.

[9] E. Mitchell, A. Jimenez, R. K. Gupta, B. K. Gupta, K. Ramasamy, M. Shahabuddin and S. R. Mishra, *New J. Chem.*, 2015, **39**, 2181-2187.

[10] Y. Zhu, Z. Wu, M. Jing, W. Song, H. Hou, X. Yang, Q. Chen and X. Ji, *Electrochim. Acta*, 2014, **149**, 144-151.

[11] L. Niu, Y. Wang, F. Ruan, C. Shen, S. Shan, M. Xu, Z. Sun, C. Li, X. Liu and Y. Gong, *J. Mater. Chem. A*, 2016, **4**, 5669-5677.

[12] Z. Yang, X. Zhu, K. Wang, G. Ma, H. Cheng and F. Xu, *Appl. Surf. Sci.*, 2015, **347**, 690-695.

[13] C. Biagioni and M. Pasero, *Am. Mineral.*, 2014, **99**, 1254-1264.

[14] M. R. Gao, J. Jiang and S. H. Yu, *Small*, 2012, **8**, 13-27.

[15] C. Xia, P. Li, A. N. Gandi, U. Schwingenschlögl and H. N. Alshareef, *Chem. Mater.*, 2015, **27**, 6482-6485.

[16] S. Y. Khoo, J. Miao, H. B. Yang, Z. He, K. C. Leong, B. Liu and T. T. Y. Tan, *Adv. Mater. Interfaces*, 2015, **2**.

[17] J. Liu, J. Wang, B. Zhang, Y. Ruan, L. Lv, X. Ji, K. Xu, L. Miao and J. Jiang, *ACS Appl. Mater. Interfaces*, 2017, **9**, 15364-15372.

[18] J. Xiao, L. Wan, S. Yang, F. Xiao and S. Wang, *Nano Lett.*, 2014, **14**, 831-838.

[19] C. Xia and H. N. Alshareef, *Chem. Mater.*, 2015, **27**, 4661-4668.

[20] F. Lu, M. Zhou, W. Li, Q. Weng, C. Li, Y. Xue, X. Jiang, X. Zeng, Y. Bando and D. Golberg, *Nano Energy*, 2016, **26**, 313-323.

[21] D.-Y. Kim, G. Ghodake, N. Maile, A. Kadam, D. S. Lee, V. Fulari and S. Shinde, *Sci. Rep.*, 2017, **7**, 9764.

[22] Y. M. Chen, Z. Li and X. W. D. Lou, *Angew. Chem.*, 2015, **127**, 10667-10670.

[23] L. Shen, L. Yu, H. B. Wu, X.-Y. Yu, X. Zhang and X. W. D. Lou, *Nat. Commun.*, 2015, **6**, 6694.

[24] B. Y. Guan, L. Yu, X. Wang, S. Song and X. W. D. Lou, *Adv. Mater.*, 2017, **29**.

[25] S. Peng, L. Li, C. Li, H. Tan, R. Cai, H. Yu, S. Mhaisalkar, M. Srinivasan, S. Ramakrishna and Q. Yan, *Chem. Commun.*, 2013, **49**, 10178-10180.

[26] P. Rudolph, *Cryst. Res. Technol.*, 2003, **38**, 542-554.

[27] B. Chen, H. Zhong, W. Zhang, Z. a. Tan, Y. Li, C. Yu, T. Zhai, Y. Bando, S. Yang and B. Zou, *Adv. Funct. Mater.*, 2012, **22**, 2081-2088.

[28] F. Viñes, G. Konstantatos and F. Illas, *Phys. Chem. Chem. Phys.*, 2017, **19**, 27940-27944.

[29] L. D. Nyamen, V. R. Pullabhotla, A. A. Nejo, P. T. Ndifon, J. H. Warner and N. Revaprasadu, *Dalton Trans.*, 2012, **41**, 8297-8302.

[30] N. Moloto, N. Revaprasadu, M. Moloto, P. O'Brien and M. Helliwell, *Polyhedron*, 2007, **26**, 3947-3955.

[31] P. S. Nair, T. Radhakrishnan, N. Revaprasadu, G. Kolawole and P. O'Brien, *J. Mater. Chem.*, 2004, **14**, 581-584.

[32] M. D. Khan, J. Akhtar, M. A. Malik and N. Revaprasadu, *ChemistrySelect*, 2016, **1**, 5982-5989.

[33] M. D. Khan, M. Akhtar, M. A. Malik, N. Revaprasadu and P. O'Brien, *ChemistrySelect*, 2018, **3**, 2943-2950.

[34] M. Khan, M. Malik, J. Akhtar, S. Mlowe and N. Revaprasadu, *Thin Solid Films*, 2017, **638**, 338-344.

[35] A. A. Memon, M. Dilshad, N. Revaprasadu, M. A. MALIK, J. Raftery and J. Akhtar, *Turk. J. Chem.*, 2015, **39**, 169-178.

[36] S. Mlowe, D. J. Lewis, M. A. Malik, J. Raftery, E. B. Mubofu, P. O'Brien and N. Revaprasadu, *New J. Chem.*, 2014, **38**, 6073-6080.

[37] M. D. Khan, M. Aamir, M. Sohail, M. Sher, J. Akhtar, M. A. Malik and N. Revaprasadu, *Sol. Energy*, 2018, **169**, 526-534.

[38] M. D. Khan, M. Aamir, M. Sohail, M. Sher, N. Baig, J. Akhtar, M. A. Malik and N. Revaprasadu, *Dalton Trans.*, 2018, **47**, 5465-5473.

[39] N. Revaprasadu, S. Mlowe and M. P. Akerman, *New J. Chem.*, 2018.

[40] D. P. Dutta, G. Sharma and I. Gopalakrishnan, *Mater. Lett.*, 2008, **62**, 1275-1278.

[41] N. Mntungwa, M. Khan, S. Mlowe and N. Revaprasadu, *Mater. Lett.*, 2015, **145**, 239-242.

[42] M. D. Khan, J. Akhtar, M. A. Malik, M. Akhtar and N. Revaprasadu, *New J. Chem.*, 2015, **39**, 9569-9574.

[43] M. Prabu, K. Ketpang and S. Shanmugam, *Nanoscale*, 2014, **6**, 3173-3181.

[44] W. Du, Z. Wang, Z. Zhu, S. Hu, X. Zhu, Y. Shi, H. Pang and X. Qian, *J. Mater. Chem. A*, 2014, **2**, 9613-9619.

[45] N. Kurra, C. Xia, M. N. Hedhili and H. N. Alshareef, *Chem. Commun.*, 2015, **51**, 10494-10497.

[46] Y. Ohno, *Phys. Rev. B*, 1991, **44**, 1281.

[47] X. Li, Q. Li, Y. Wu, M. Rui and H. Zeng, *ACS Appl. Mater. Interfaces*, 2015, **7**, 19316-19323.

[48] X. Wang, C. Yan, A. Sumboja, J. Yan and P. S. Lee, *Adv. Energy Mater.*, 2014, **4**.

[49] S. A. Pervez, D. Kim, U. Farooq, A. Yaqub, J.-H. Choi, Y.-J. Lee and C.-H. Doh, *ACS Appl. Mater. Interfaces*, 2014, **6**, 11219-11224.

[50] D. Liu, Q. Lu, Y. Luo, X. Sun and A. M. Asiri, *Nanoscale*, 2015, **7**, 15122-15126.

[51] W. Zhu, M. Ren, N. Hu, W. Zhang, Z. Luo, R. Wang, J. Wang, L. Huang, Y. Suo and J. Wang, *ACS Sustain. Chem. Eng.*, 2018.

[52] A. Sivanantham, P. Ganesan and S. Shanmugam, *Adv. Funct. Mater.*, 2016, **26**, 4661-4672.

[53] C. Ranaweera, C. Zhang, S. Bhoyate, P. Kahol, M. Ghimire, S. Mishra, F. Perez, B. K. Gupta and R. K. Gupta, *Mater. Chem. Frontiers*, 2017, **1**, 1580-1584.

[54] Y. Q. Wu, X. Y. Chen, P. T. Ji and Q. Q. Zhou, *Electrochim. Acta*, 2011, **56**, 7517-7522.

[55] R. R. Salunkhe, K. Jang, H. Yu, S. Yu, T. Ganesh, S.-H. Han and H. Ahn, *J. Alloys Compd.*, 2011, **509**, 6677-6682.

[56] X. Chen, D. Chen, X. Guo, R. Wang and H. Zhang, *ACS Appl. Mater. Interfaces*, 2017, **9**, 18774-18781.

[57] S. Bhoyate, C. K. Ranaweera, C. Zhang, T. Morey, M. Hyatt, P. K. Kahol, M. Ghimire, S. R. Mishra and R. K. Gupta, *Global Challenges*, 2017, **1**.

Appendix 5.1

References

[1] D. Liu, Q. Lu, Y. Luo, X. Sun and A. M. Asiri, *Nanoscale*, 2015, **7**, 15122–15126.

[2] W. Zhu, M. Ren, N. Hu, W. Zhang, Z. Luo, R. Wang, J. Wang, L. Huang, Y. Suo and J. Wang, *ACS Sustain. Chem. Eng.*, 2018, acssuschemeng.7b04663.

[3] H. Shi and G. Zhao, *J. Phys. Chem. C*, 2014, **118**, 25939–25946.

[4] C. Zhu, D. Wen, S. Leubner, M. Oschatz, W. Liu, M. Holzschuh, F. Simon, S. Kaskel and A. Eychmüller, *Chem. Commun.*, 2015, **51**, 7851–7854.

[5] H. Liang, F. Meng, M. Cabán-Acevedo, L. Li, A. Forticaux, L. Xiu, Z. Wang and S. Jin, *Nano Lett.*, 2015, **15**, 1421–1427.

[6] H. Hu, B. Guan, B. Xia and X. W. Lou, *J. Am. Chem. Soc.*, 2015, **137**, 5590–5595.

[7] T. Zhu, L. Zhu, J. Wang and G. W. Ho, *J. Mater. Chem. A*, 2016, **4**, 13916–13922.

[8] M. Shen, C. Ruan, Y. Chen, C. Jiang, K. Ai and L. Lu, *ACS Appl. Mater. Interfaces*, 2015, **7**, 1207–1218.

[9] X. Wu, X. Han, X. Ma, W. Zhang, Y. Deng, C. Zhong and W. Hu, *ACS Appl. Mater. Interfaces*, 2017, **9**, 12574–12583.

[10] S. Dou, L. Tao, J. Huo, S. Wang and L. Dai, *Energy Environ. Sci.*, 2016, **9**, 1320–1326.

[11] A. Sivanantham, P. Ganesan and S. Shanmugam, *Adv. Funct. Mater.*, 2016, **26**, 4661–4672.

[12] N. Jiang, Q. Tang, M. Sheng, B. You, D. Jiang and Y. Sun, *Catal. Sci. Technol.*, 2016, **6**, 1077–1084.

[13] L. Feng, H. Vrubel, M. Bensimon and X. Hu, *Phys. Chem. Chem. Phys.*, 2014, **16**, 5917.

[14] X. Zhang, H. Xu, X. Li, Y. Li, T. Yang and Y. Liang, *ACS Catal.*, 2016, **6**, 580–588.

[15] Y. Hou, M. R. Lohe, J. Zhang, S. Liu, X. Zhuang and X. Feng, *Energy Environ. Sci.*, 2016, **9**, 478–483.

[16] H. Jin, J. Wang, D. Su, Z. Wei, Z. Pang and Y. Wang, *J. Am. Chem. Soc.*, 2015, **137**, 2688–2694.

[17] J. Tian, Q. Liu, A. M. Asiri and X. Sun, *J. Am. Chem. Soc.*, 2014, **136**, 7587–7590.

CHAPTER 6

SUMMARY OF WORK AND FUTURE OUTLOOK

6.1. Summary and Conclusion

The work aimed at proposing the use of Co and Ni heterocyclic dithiocarbamate complexes as single source molecular precursors (SSP) towards the fabrication of corresponding metal sulfide nanoparticles and thin films. The nanoparticles were fabricated in both binary and ternary form. Prior to the fabrication processes, it was of crucial importance to ascertain the chemical composition and purity of the complexes, as per requirements for SSP. Thus, the complexes were fully characterised by FTIR spectroscopy and elemental analysis; nuclear magnetic resonance spectroscopy measurements could not be applied to all due to the metallic nature of the Ni and Co metal centres which renders the technique unsuitable. Regardless of this, the most reliable analytical tool, single crystal X-ray crystallography, was used to elucidate the structures of the complexes.

The synthesis of Ni_xS_y nanoparticles focused on establishing reaction parameters to afford phase-pure material, by using the hot injection method. Rare phase-pure Ni_3S_4 and Ni_3S_2 nanoparticles could be obtained by varying the chain length of the amine capping agents (dodecylamine, hexadecylamine and oleylamine). The nature of the *bis*(piperidinylldithiocarbamato)nickel(II) (**1**), *bis*(tetrahydroquinolinyldithiocarbamato)nickel(II) (**2**) and *bis*(*N'*-ethyl-*N*-piperazinyldithiocarbamato)nickel(II) (**3**) complexes also played a role in controlling the phase of the nanoparticles. The magnetism of the nanoparticles was investigated and it was found that Ni_3S_4 showed ferromagnetic behaviour while Ni_3S_2 showed paramagnetic behaviour. The same complexes (**1**)-(**3**) were used to deposit Ni_xS_y thin films by the aerosol assisted chemical vapour deposition method. The films were matched to NiS phase. Interestingly, the nature of the complexes and deposition temperatures were found to have morphology control, from long rods to irregular plate-like morphology. Furthermore, the UV-Vis absorption measurements indicated quantum confinement effects, due to blue-shifted optical energy band gap between 3.1 eV and 4.2 eV.

Co_xS_y nanoparticles were synthesized from *tris*(morpholinodithiocarbamato)cobalt(III) complex (**4**), via an oleylamine-mediated hot injection method. The nanoparticles prepared were tested for both energy generation and storage; they demonstrated good electrochemical and electrocatalytic performances. The as prepared nanoparticles have been evaluated for energy

generation and energy storage studies. **CoS-2** sample (260 °C) displayed better electrochemical and electrocatalytic performances than **CoS-1** (230 °C), whereby **CoS-2** had a lower overpotential (276 mV) to generate a current density of 10 mA/cm^2 than **CoS-1** (307 mV), indicative of the superiority of **CoS-2** in terms of electrocatalytic performance. The maximum specific capacitance for **CoS-2** sample is 440 F g^{-1} and 1059 F g^{-1} which were calculated from the GCD curve and CV curve of **CoS-2** at a current density of 1 A g^{-1} and a scan rate of 1 mV s^{-1}, respectively.

Co and Ni-rich $Ni_xCo_{3-x}S_4$ nanosheets were synthesized from the solvent thermolysis of equimolar *bis*(*N'*-ethyl-*N*-piperazinyldithiocarbamato)nickel(II) (**3**) and *tris*(*N'*-ethyl-*N*-piperazinyldithiocarbamato)cobalt(III) (**5**) complexes. The reaction utilized oleylamine as a coordinating solvent. The nanosheets were then evaluated as active materials in the O_2 evolution reaction (OER) and hydrogen evolution reaction (HER). The Ni-rich nanosheets indicated a relatively higher OER and HER compared to the Co-rich counterparts, attributed to the differences observed in their Tafel slope values. Furthermore, the capacitance studies indicate Ni-rich nanosheets exhibiting relatively higher supercapacitance performance. Both Ni and Co-rich nanosheets showed capacitance of above 85 % after 5000 cycles. The study observed that the Ni-rich nanosheets showed superiority in energy generating and storage efficiency.

The overall work demonstrated the necessity of tweaking reaction parameters to tailor the properties of the nanoparticles and thin towards various applications. The nature of the complex determines the decomposition pathway or mechanism, when coupled with other factors such as reaction temperature and nature of the coordinating solvent (capping agent). The resulting nanoparticles show interesting performances in various suitable applications.

6.2. Future Work

The future outlook identifies the opportunity to measure the electrochemical and electrocatalytic behaviour of phase pure Ni_3S_2 and NiS and compare with the already published works of the Ni-Co-S ternary system. It is important also to use greener capping agent as another means of tuning the morphology of both binary Ni-S and Co-S and assess their magnetic, electrochemical and electrocatalitic performance. Lastly, it is scientifically feasible to apply the

ternary material in light emitting diodes (LED) and thus assess their durability and stability in this regard.

Appendices: List of selected publications, conferences and ligands/complexes used in this study

List of Publications

(1) Gervas, C.; Mubofu, E. B.; Mdoe, J. E. G.; Revaprasadu, N. Functionalized Mesoporous Organo-Silica Nanosorbents for Removal of Chromium (III) Ions from Tanneries Wastewater. *J. Porous Mater.* **2016**, *23* (1), 83.

(2) Gervas, C.; Mlowe, S.; Revaprasadu, N. Synthesis of PbTe and PbSe Nanoparticles under the Influence of Hydrochloric Acid and Carbon Dioxide. *Mater. Sci. Semicond. Process.* **2016**, *56*.

(3) Masikane, S. C.; Mlowe, S.; Gervas, C.; Revaprasadu, N.; Pawar, A. S.; Garje, S. S. Lead(II) Halide Cinnamaldehyde Thiosemicarbazone Complexes as Single Source Precursors for Oleylamine-Capped Lead Sulfide Nanoparticles. *J. Mater. Sci. Mater. Electron.* **2017**.

(4) Gervas, C.; Mlowe, S.; Akerman, M. P.; Ezekiel, I.; Moyo, T.; Revaprasadu, N. Synthesis of Rare Pure Phase Ni3S4 and Ni3S2 Nanoparticles in Different Primary Amine Coordinating Solvents. *Polyhedron* **2017**, *122*, 16.

(5) Gervas, C.; Mlowe, S.; Akerman, M. P. and N. R. Phase Pure Ni3S2 and NiS from Bis(N'-Ethyl-N-Piperazinylcarbodithioato-S,S')-Nickel(II) via Solvent Thermolysis and Aerosol Assisted Chemical Vapour Deposition. *New J. Chem.* **2018**.

(6) Gervas, C.; Khan, M. D.; Zhang, C.; Zhao, C.; Gupta, R. K.; Carleschi, E.; Doyle, B. P.; Revaprasadu, N. Effect of Cationic Disorder on the Energy Generation and Energy Storage Applications of $Ni_x Co_{3-x} S_4$ Thiospinel. *RSC Adv.* **2018**, *8* (42), 24049.

(7) Charles Gervas, Malik Dilshad Khan, Sixberth Mlowe, Chunyang Zhang,[b] Chen Zhao,[b] Ram K. Gupta, Matthew P. Akerman, and Neerish Revaprasadu[i]. Facile synthesis of bifunctional Co_xS_y nanoplates for efficient H_2/O_2 evolution and supercapacitance. *Submitted for peer-review*.

Conferences

1. **Poster Presentation** at: Annual Conference for Tanzania Chemical Society Internatinal Chemistry Conference 5th – 7th OCTOBER, 2011, Girraffe Ocean View Hotel in Dar es Salaam – presentation on the topic of ***'Preparation of Sunflower Oil – Templated Organo-Silica Composites for Removal of Chromium (III) Ions from Tanneries Wastewater'***

2. **Poster Presentation** at: 7th International Symposium on Macro- and Supramolecular Architectures and Materials (MAM-14)- 23–27 November 2014 Mintek Johannesburg, South Africa – Presented on: ***Synthesis of PbTe and PbSe Nanoparticles under the Influence of Hydrochloric Acid and Carbon Dioxide***

3. **Oral Presentaion** at: University of Mumbai India (30th November, 2015- 4th December 2015) - International Conference: Presented on ***'Preparation of Sunflower Oil – Templated Organo-Silica Composites for Removal of Chromium(III) Ions from Tanneries Wastewater'***

4. **Delegate at**: **MSSA Conference 2016:** The Boardwalk Convention Centre, Port Elizabeth. (05 Dec 2016 to 09 Dec 2016)

5. **Flash Talk at:** SACI Inorganic 2017 at Arabella Hotel and Spa Hermanus, Western Cape 25-29 June 2017. Presented on: ***'Preparation of heterocyclic dithiocarbamante nickel complexes as single source precursors for various pure phases of nickle sulfide nanopaticles and thin films'.***

6. **Poster Presentation** at: South African Nanotechnology Initiative (SANI) at Salt Rock Hotel (22nd – 25th April, 2018), Durban SA- Presented on *'**Phase pure Ni_3S_2 and NiS from bis(N'-ethyl-N-piperazinylcarbodithioato-S,S')-nickel(II) via solvent thermolysis and aerosol assisted chemical vapour deposition'.***